3-D Characterization of the Structure of Paper and Paperboard and Their Application to Optimize Drying and Water Removal Processes and End-Use Applications
(DOE Project DE-FC07-00ID13873)

Shri Ramaswamy
University of Minnesota

B.V. Ramarao
State University of New York

A Final Report to the U.S. Department of Energy
August 29, 2004

Table of Contents

Final Project Report

3-D Characterization of the Structure of Paper and Paperboard and Their Application to Optimize Drying and Water Removal Processes and End-Use Applications

Covering Period: January 1, 2000 to December 31, 2003

Date of Report: August 29, 2004

Recipient: University of Minnesota (UMN)

Award Number: DE-FC07-00ID13873

Subcontractors: State University of New York

Other Partners: (Hercules Inc., Wilmington, DE, in-kind support)

Contact: Shri Ramaswamy (PI), ph: 612 624 8797, e-mail: shri@umn.edu; Dr. B.V. Ramarao (co-PI), ph: 315 470 6524, e-mail: bvramara@syr.edu

Project Objective: Develop an accurate, direct, non-invasive method to visualize the complex pore structure of paper and board. Characterize the three dimensional bulk structure of paper and paper board using sophisticated image analysis techniques. Develop relationships between pore structure characteristics and transport properties namely, water vapor diffusivity and liquid permeability.

ABSTRACT

The three dimensional structure of paper materials plays a critical role in the paper manufacturing process especially via its impact on the transport properties for fluids. Dewatering of the wet web, pressing and drying will benefit from knowledge of the relationships between the web structure and its transport coefficients. Among transport, moisture diffusion in paper is central to the understanding and optimal design of paper products for their performance in different environmental conditions. Our recent research of moisture sorption in paper has indicated that diffusion of water vapor through the pore space is an important mechanism for transport [Ramaswamy, 2001, Huang, 2002]. The effect of the three dimensional structure of the paper sheet on the diffusion of moisture is significant.

The structure of the pore space within a paper sheet is imaged in serial sections using x-ray micro computed tomography. The three dimensional structure is reconstructed from these sections using digital image processing techniques. The structure is then analyzed by measuring traditional descriptors for the pore space such as specific surface area and porosity. In addition, morphometric and quantitative stereological techniques are used to characterize the structure. Techniques of mathematical morphology [Serra, 1986] used include erosion, dilation, closing, opening and binarization with subsequent skeletonization.

A sequence of microtomographs was imaged at approximately 2 μm intervals and the three-dimensional pore-fiber structure was reconstructed. The pore size distributions for both in-plane as well as transverse pores were measured. Significant differences in the in-plane (XY) and the transverse directions in pore characteristics are found and may help partly explain the different liquid and vapor transport properties in the in-plane and transverse directions. The results from the mathematical morphological study show that the pore space and the fiber space are bicontinuous. Some network measures of both these spaces are the network nodal density and bond co-ordination number distribution, both of which are determined. Significant transport properties for the pore space include the saturated water permeability and water vapor diffusivity. Due to the anisotropic nature of the structure, these are three-dimensional tensors in general.

Results with varying sheet structures compare favorably with conventional mercury intrusion porosimetry data. X-ray microtomography combined with digital image analysis has also been shown to be capable of independently evaluating the in plane and transverse pore structure characteristics of paper and paperboard. Interestingly, the transverse pore structure appears to be more open with larger pore size distribution compared to the in plane pore structure. This may help explain the differences in liquid and vapor transport through the in plane and transverse structures during the paper manufacturing process and during end-use application.

Comparison of Z-directional structural details of hand sheet and commercially made fine paper samples show a distinct difference in pore size distribution both in the in-plane and transverse direction. Commercial sheets show significant variation through the thickness direction potentially owing to the non-uniformity during formation. Method presented here may provide a useful tool to the papermaker to truly engineer the structure of paper and board tailored to specific end-use applications.

Surface structure characteristics of porous materials such as paper and board play an important role in surface related applications, i.e. writing, printing, coating etc. The difference in surface structure between the top and bottom sides of the porous material, i.e. "two-sidedness" due to processing and raw material characteristics may lead to differences in end-use performance. Image analysis methods to characterize the surface structure of porous materials using X-ray micro computed tomography were also developed. This complements our earlier method to analyze the bulk structure and Z-D structure of porous materials. The measurements of surface structure characteristics include thickness distribution, surface volume distribution, contact fraction distribution and surface pit distribution. Method developed here even though shown for low resolution X-ray tomography images are equally applicable for high resolution (~1 micron) images. As one would expect, the surface structure characteristics will be critically dependent on the quality and resolution of the images. This presents a useful tool to characterize and engineer the surface structure of porous materials such as paper and board tailored to specific end-use applications. This will also help troubleshoot problems related to manufacturing and end-use applications.

This study attempted to identify the optimal resolution through a comparison between 3D images obtained by monochromatic synchrotron radiation *X-mCT* in phase contrast mode (resolution ≈ 1 μm) and polychromatic radiation *X-mCT* in absorption mode (res. ≈ 5 μm).

It was found that both resolutions have the ability to show the expected trends when comparing different paper samples. The low resolution technique shows fewer details resulting in lower specific surface area, larger pore channels, characterized as hydraulic radii, and lower tortuosities, where differences between samples and principal directions are more difficult to detect. The low resolution images are also noisier. The disadvantages of the high resolution images are high cost and limited availability of hard x-ray beam time as well as the small size of the sample volumes imaged. The results show that the low resolution images can be used for comparative studies, whereas the high resolution images may be better suited for fundamental research on the paper structure and its influence on paper properties, as one gets more accurate physical measurements.

In addition, pore space diffusion model has been developed to simulate simultaneous diffusion in heterogeneous porous materials such as paper containing cellulose fibers and void spaces. Stochastic dynamic approach along with random walk simulation has been implemented to model simultaneous diffusion in 3D matrix of cellulose fibers and pores. This model is suitable for simulating simultaneous diffusion in porous materials under variety of conditions including low relative humidity conditions where diffusion occurs predominantly through one medium i.e. pore space and high humidity conditions where both mediums (i.e. fiber and pore spaces) are highly conductive. Both pore as well as effective diffusivity values for paper samples of varying structure were compared with the experimental values and are in fair agreement especially through the thickness direction of samples. In addition to this, intrinsic fiber phase diffusivity has been estimated for the first time using a combination of simulation and experimental data.

INTRODUCTION AND BACKGROUND

The structure of the inter-fiber voids in paper governs some of its important transport properties. Among the most significant is the conductivity to moisture in both the saturated and unsaturated states. Moisture conduction in free liquid, bound water and vapor forms is central to many processing operations such as the drainage of the wet-web, its subsequent dewatering under vacuum and pressure and finally its drying behavior. Furthermore, conductivity of the paper to moisture at low moisture contents is important in controlling the physical properties such as its elastic moduli [Wang, 1991, Habeger 1999,]. Thus, the relationship between the structure of the paper from the void space and fiber aspects is of significant interest.

X-ray microtomography is a relatively new technique used in the three-dimensional imaging of materials. This method consists of obtaining large set of images while passing radiation through the sample at different angles. The projected images can be combined to reconstruct an approximation of geometry of the interior structure. Traditional x-ray imaging in medical applications uses absorptive contrast between high density bone materials and low density tissue. In the case of paper and board, cellulose and the surrounding medium have approximately equal absorptivities and hence the contrast is minimal. In such structures, “phase contrast imaging” based on relative difference in refractive index between cellulose fibers and surrounding medium is used. Samuelsen et.al. [1999, 2001] , Guruyev et.al. [2001] and Goel et al. [2001] have shown the use of “phase contrast imaging” in paper.

METHODS

In order to study the relationship between pore structure and transport properties, hand sheets of varying structure were prepared by subjecting bleached soft wood kraft fibers to varying degrees of refining. The level of mechanical pressing and other sheet forming variables were held constant. The change in apparent density values for the samples did indicate potential change in internal structure. Shown below are example microtomographs of specimens of paper sheets refined to different degrees of freeness in the laboratory.

The X-ray images were then binarized to distinguish fiber and voids using a *dynamic thresholding method* [Chow, 1972, Goel, 2000]. This method is based on the fact that the threshold value of a pixel depends on the intensities of the neighboring pixels. Each image was divided into number of overlapping windows of 128×128 pixels. Threshold values for the pixels at the center of each window were calculated using the *minimum error thresholding method* [Kittler, 1986, Goel, 2000]. This method tries to minimize the probability of misclassifying a pixel. Based on the pixel values, an intensity histogram was computed over each window. Histograms obtained using these methods were bi-modal with one distribution corresponding to voids and other to fibers. A sample histogram is shown in Figure 3. Threshold values were then calculated for pixels at the center of each window using an iterative procedure. After the threshold values for the pixels at the center of each window were calculated, thresholds for the remaining pixels were calculated using bilinear interpolation. Finally, the original intensity value g(m,n) was compared with the threshold value T(m,n) for each pixel, where (m,n) are the pixel coordinates. If g(m,n) > T(m,n) a value of 1 was assigned to the pixel, otherwise, the pixel intensity was set to 0.

Figure 1. X-ray microtomograph images of paper sheet specimens in the XY plane at 6 different refining levels (670, 570, 460, 330, 280, 220 CSF). Binary images corresponding to each image are shown in the right column.

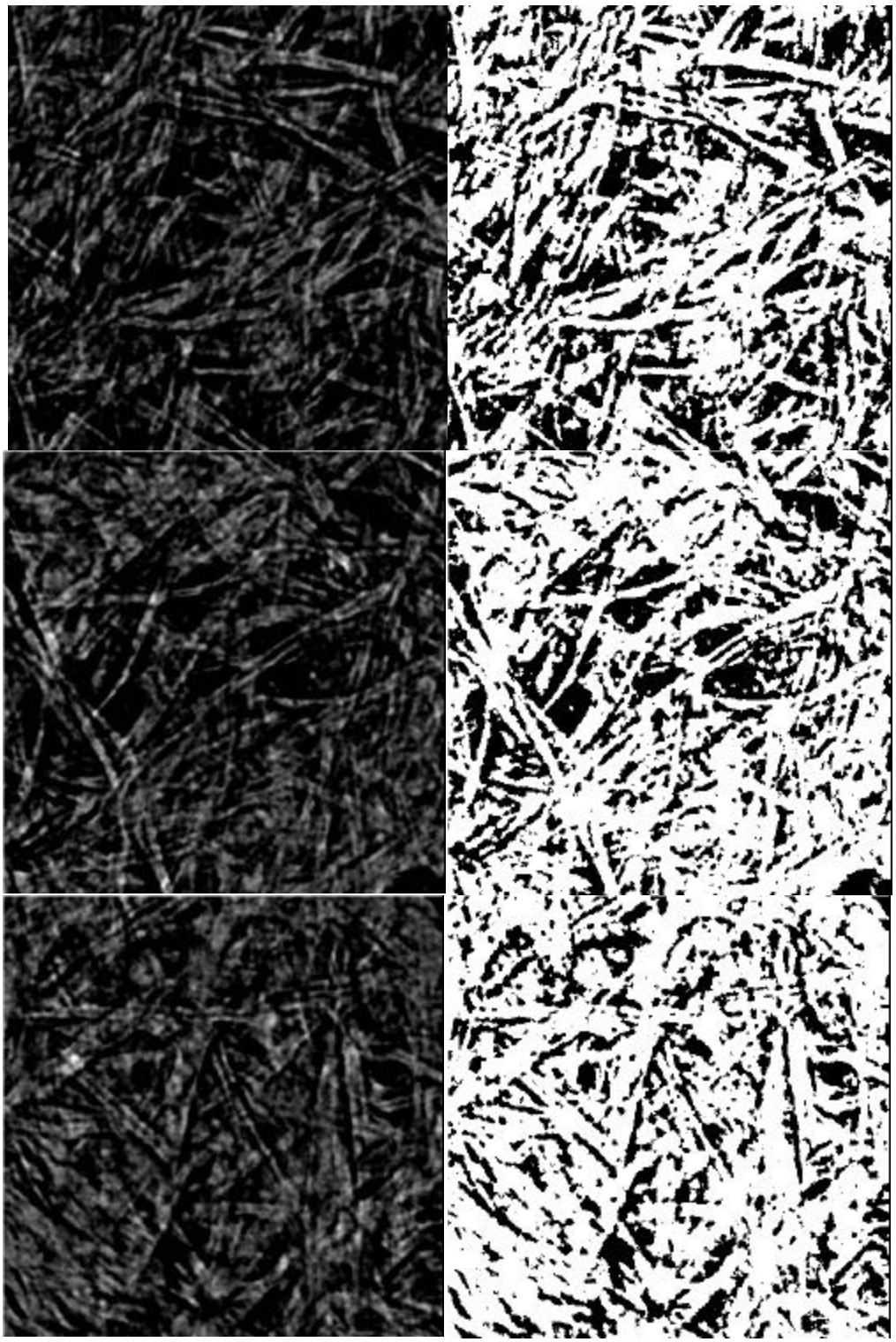

330

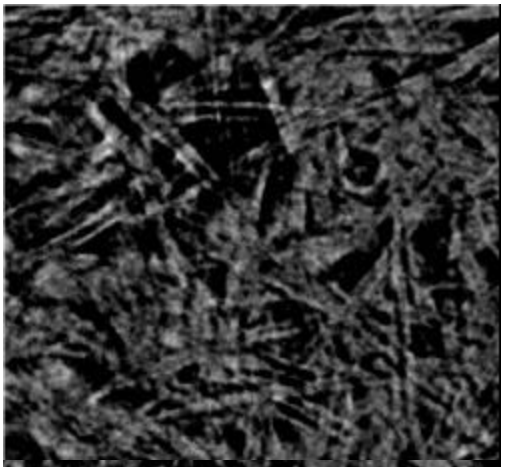

280

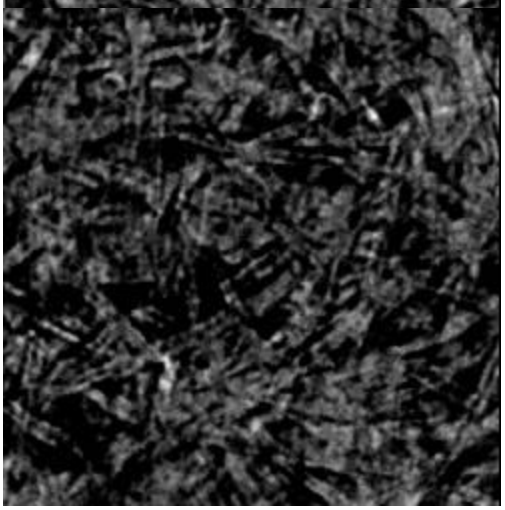

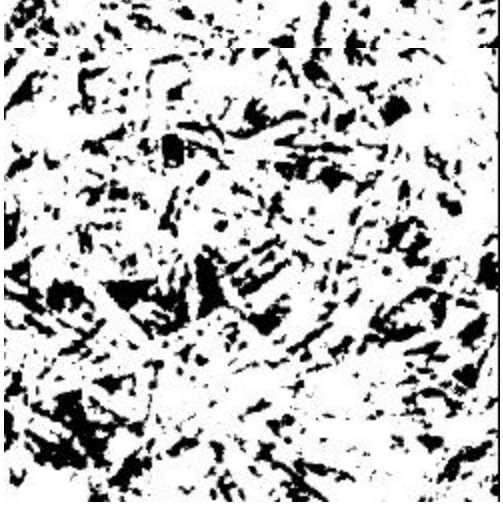

220

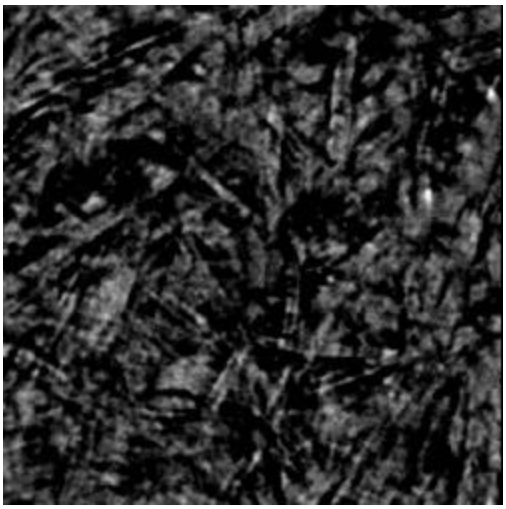

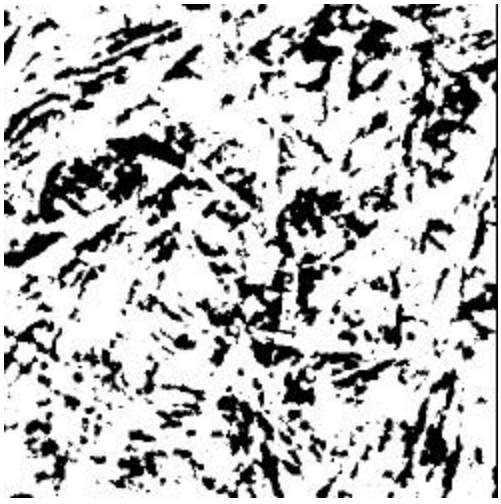

Figure 2. Binarized version of the microtomograph sections in the (a) X-Y, (460x460 pixels) (b) Y-Z (120x460 pixels) and (c) X-Z (460x120 pixels) planes.

a

b

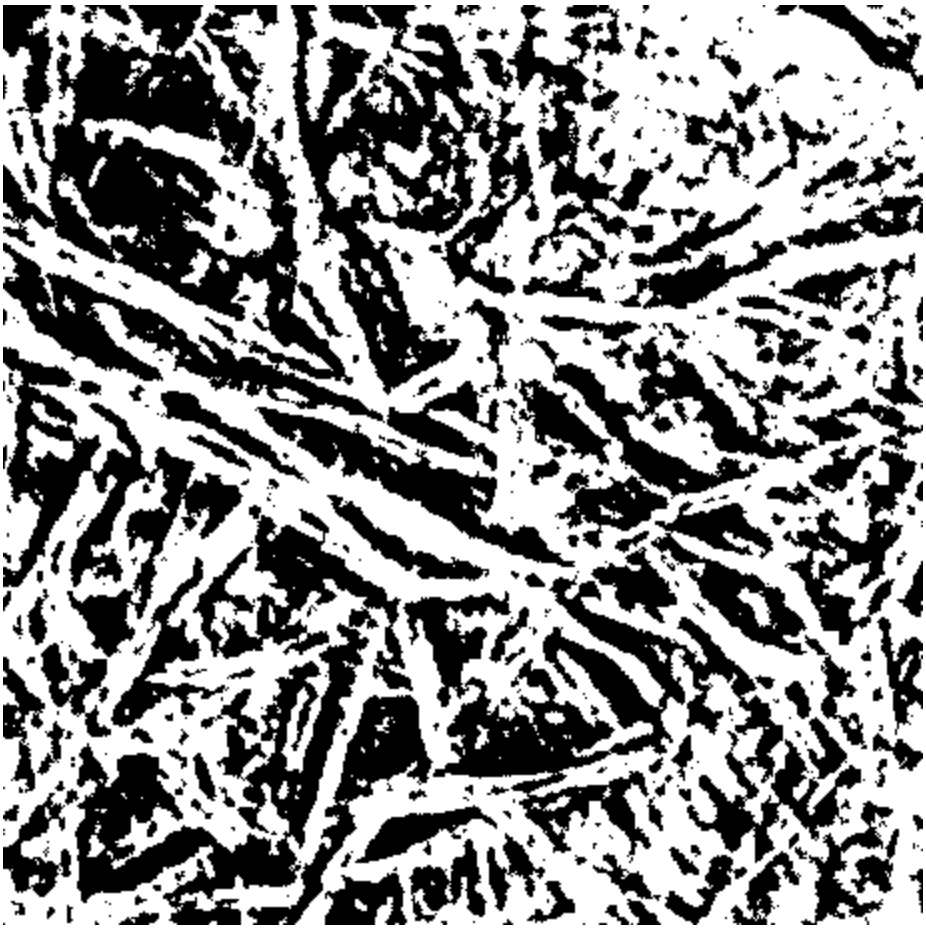

c

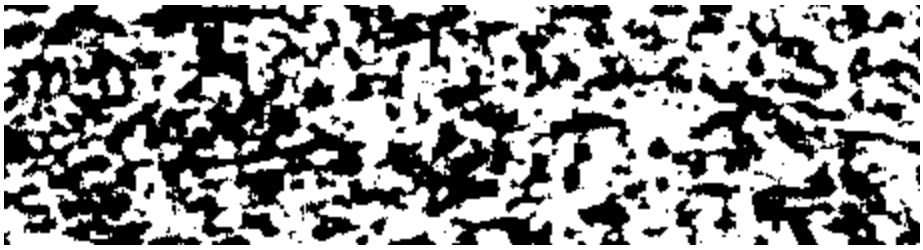

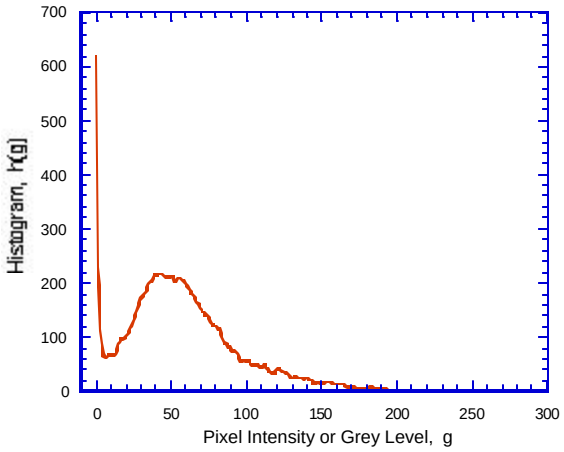

Figure 3. Sample histogram for one of the windows

RESULTS AND DISCUSSION

Having identified the fiber (white, pixel intensity 1) and void (black, pixel intensity 0), the traditional pore structure descriptors such as porosity and specific surface area are calculated as follows. The porosity (ε) of the total sample is calculated by taking the ratio of the total void pixels and the total sample pixels. The three dimensional void structure was reconstructed from a sequence of closely spaced images (2 µm apart) between the serial sections. This gave the void surface in the third dimension. A pixel when projected into the third dimension forms a voxel. Each of the fiber voxels was then compared with all of its adjacent neighbors to identify the fiber-void interfacial area. The specific surface area is then calculated as,

$$S_w = \frac{S_t}{(1-e)r_f}$$

Eq. 1

The specific surface area is given in m^2/g , the total interfacial area from the voxels is S_t, m^2, the fiber density is denoted by ρ_f (g/m^3). The porosity and specific surface area calculated from micro X-ray tomography and image analysis for samples of varying structure is shown in Figure 4. As one would expect, the porosity of the samples decrease with increasing refining or decreasing freeness values. It is interesting to note, however, that the major decrease in porosity is from larger pores (pores greater than 4.0 microns in diameter), as shown by mercury intrusion porosimetry data on these samples (Figure 5). The specific interface area was also found to decrease with freeness. At first this appears contradictory. Normally one would expect the specific surface area to increase with

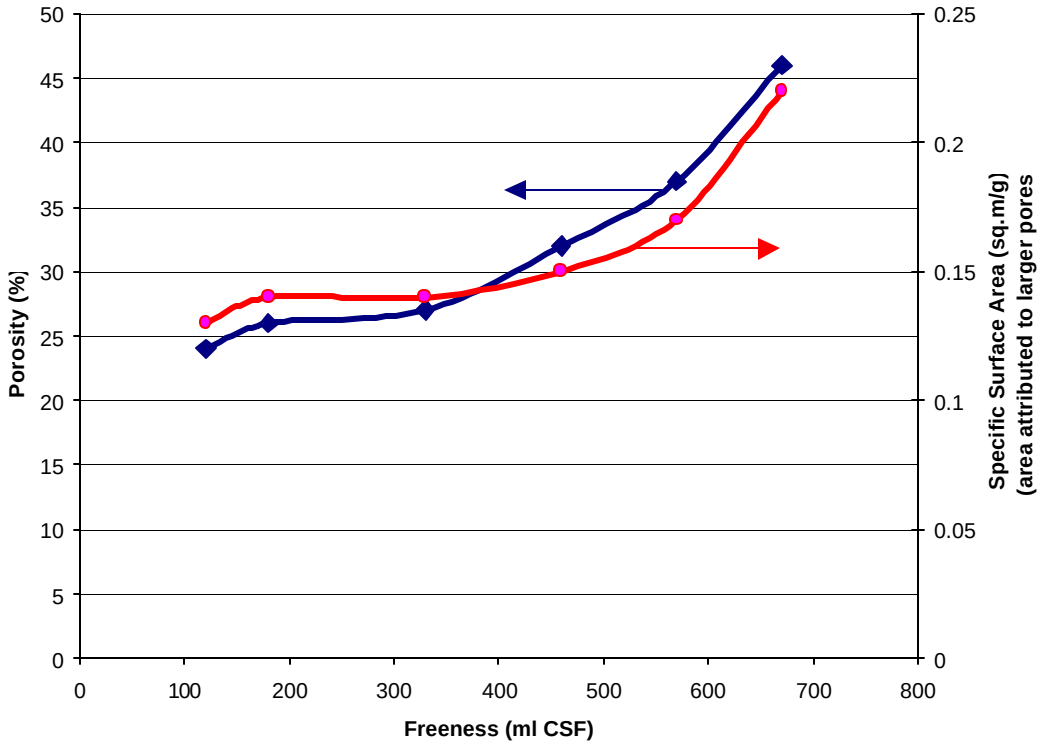

Figure 4 Porosity and specific surface area from X-ray tomography and image analysis for samples of varying structure

refining. This was indeed the case when one looks at the total specific surface area as measured by the traditional mercury intrusion technique. However, the specific surface area of pores greater than 1.0 micron in diameter was found to decrease with refining, a trend similar to that observed with image analysis (Figure 6). Detailed analysis of the mercury intrusion porosimetry data shows that while the major decrease in pore volume comes from larger pores (pore diameter > 4.0 microns), the increase in surface area with refining is primarily from much smaller pores (pore diameter less than 0.1 microns). This explains why the image analysis data show a decrease in porosity as well as a

decrease in surface area with refining. Porosity and specific surface area distributions as a function of pore diameter as obtained by mercury intrusion porosimetry for the unrefined and highly refined samples are shown in Figures 7 and 8 [Goel, 2003].

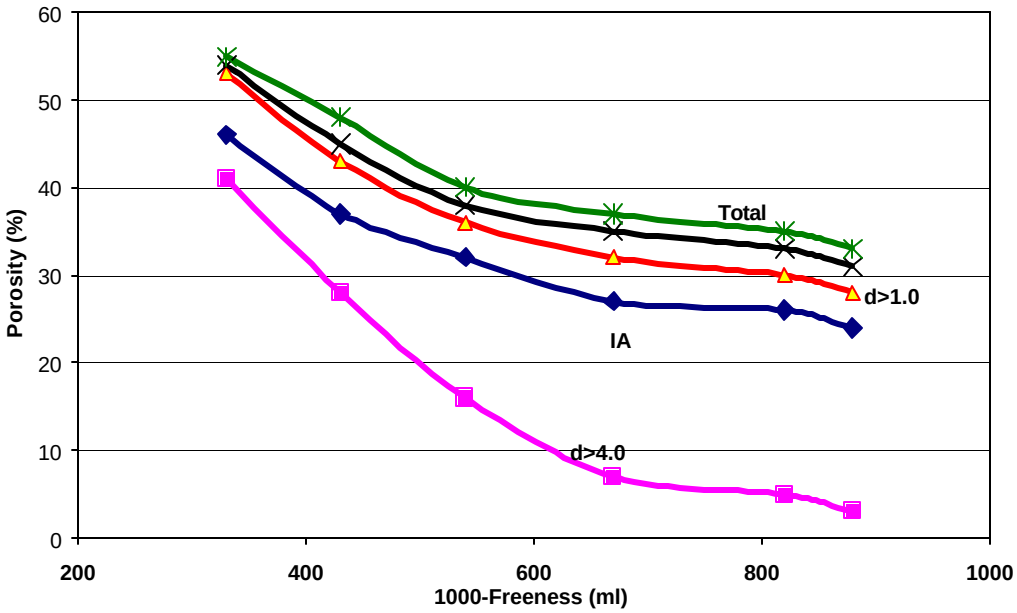

Figure 5. Porosity comparison between Image Analysis and Mercury Intrusion Porosimetry (MIP) for samples of varying structure

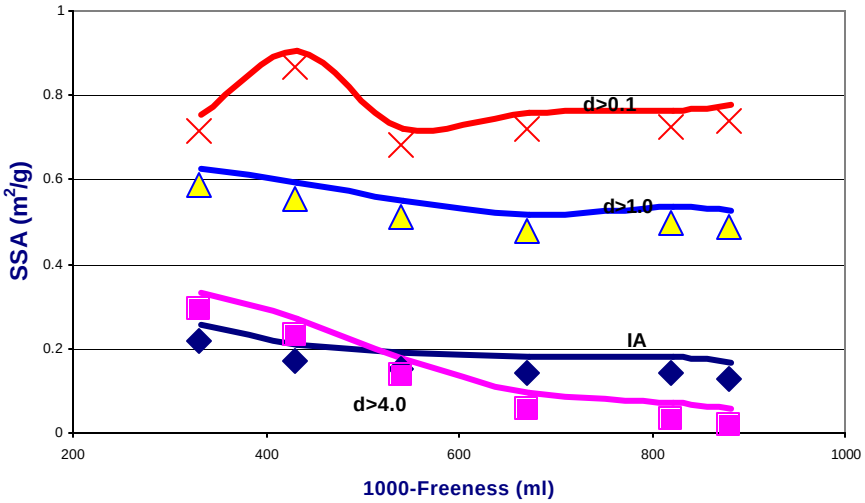

Figure 6. Specific surface area comparison between Image Analysis and Mercury Intrusion Porosimetry (MIP) for samples of varying structure

In addition to porosity and specific surface area, another traditional descriptor used in porous media is the distribution of pore size. Techniques such as mercury intrusion porosimetry generally give the volume distribution corresponding to the entire sample (Figure 7 and Figure 8). Using X-ray and image analysis, it is possible to evaluate the pore size distribution in the three independent directions. Such pore size distribution will be more meaningful in analyzing fluid flow predominantly in one direction, i.e. in-plane flow, transverse flow. In order to conduct such analysis, we define pore hydraulic radius ($R_{p,h}$, m) as follows:

$$R_{p,h} = \frac{A_p}{W_p}$$

Eq. 2

where A_p is the cross sectional area of a pore (m^2) and W_p is its perimeter (m). Since the pores can be identified from contiguous white or black regions in a binarized image, the pore size distribution can be estimated easily. Having identified the pores and their areas in each plane through the entire thickness, the perimeter of each pore is then calculated by identifying the set of pixels that belong to the pore and that have at least one neighbor that interfaces with a fiber pixel.

The volume of each pore identified in any given plane is calculated by multiplying the area of that pore by the constant slice thickness. By stacking up the volume occupied by pores of a given hydraulic radius for all slices through the thickness in any given plane, the overall pore size distribution in any plane for a sample can be obtained. It is assumed that the total pore volume (or porosity) in any given sample is the same irrespective of the XY, YZ, or XZ plane of view. Figures 9 and 10 show the pore size distribution obtained by image analysis in the XY, YZ and XZ views for two different structures. For comparison the overall pore size distribution obtained by traditional mercury intrusion porosimetry is also shown in the same figure. Here, normalized pore volumes obtained by dividing the pore volume corresponding to a specific pore size by the total pore volume is represented on the y-axis. It is interesting to note that for any given structure, the pore size distribution in the XY (or transverse) view is broader than the YZ or XZ views (in-plane views). The average pore size in the XY view is also larger than the other two directions. This indicates that potentially the fluid flowing in the transverse direction encounters a much more open pore structure

with larger pore sizes compared to the in-plane direction. This may help partly explain the differences observed in in-plane vs transverse permeability experiments.

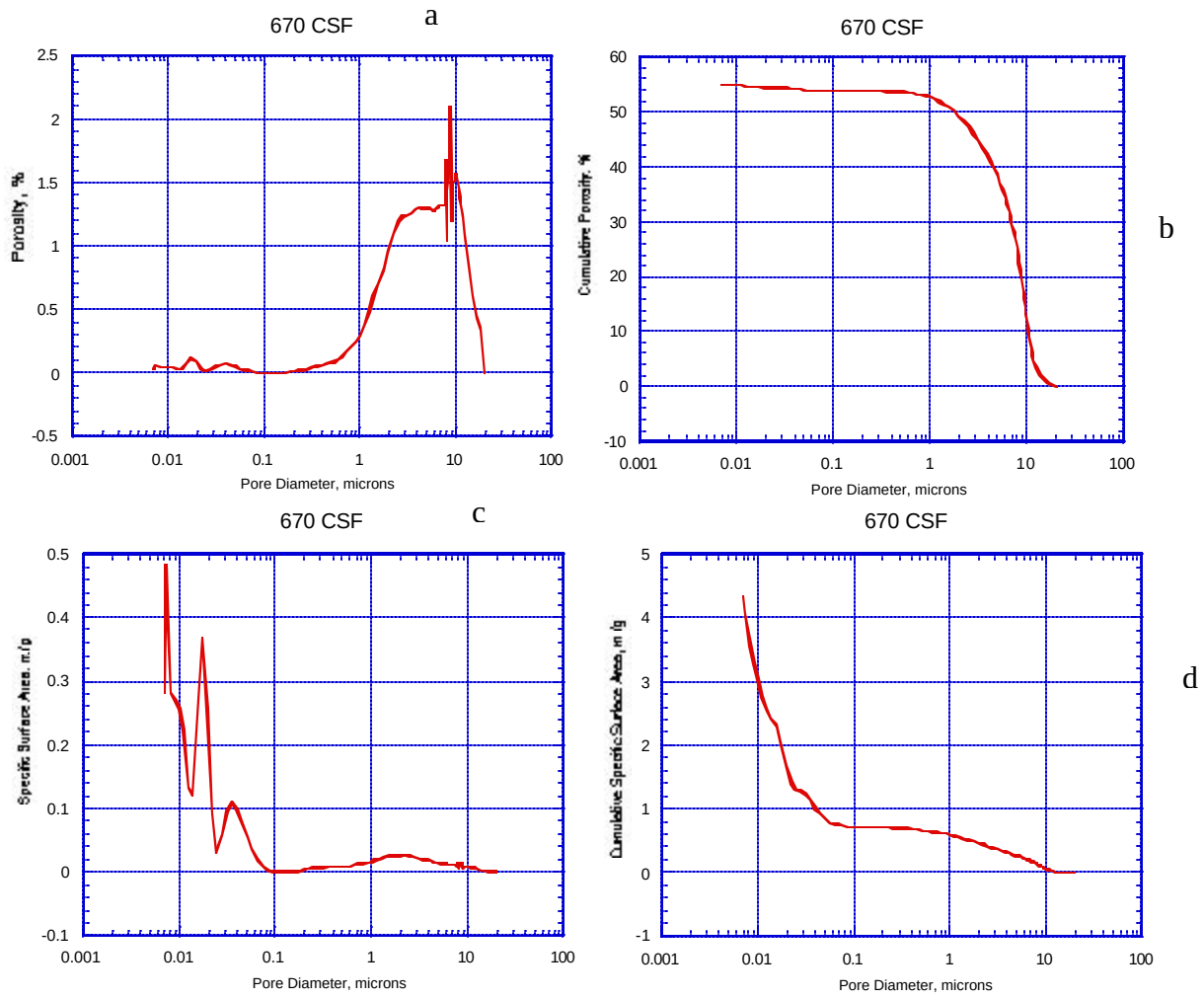

Figure 7 Porosity (a), Cumulative Porosity (b), Specific Surface Area (c), and Cumulative Specific Surface Area (d) distributions by Mercury Intrusion Porosimetry for 670 CSF sample.

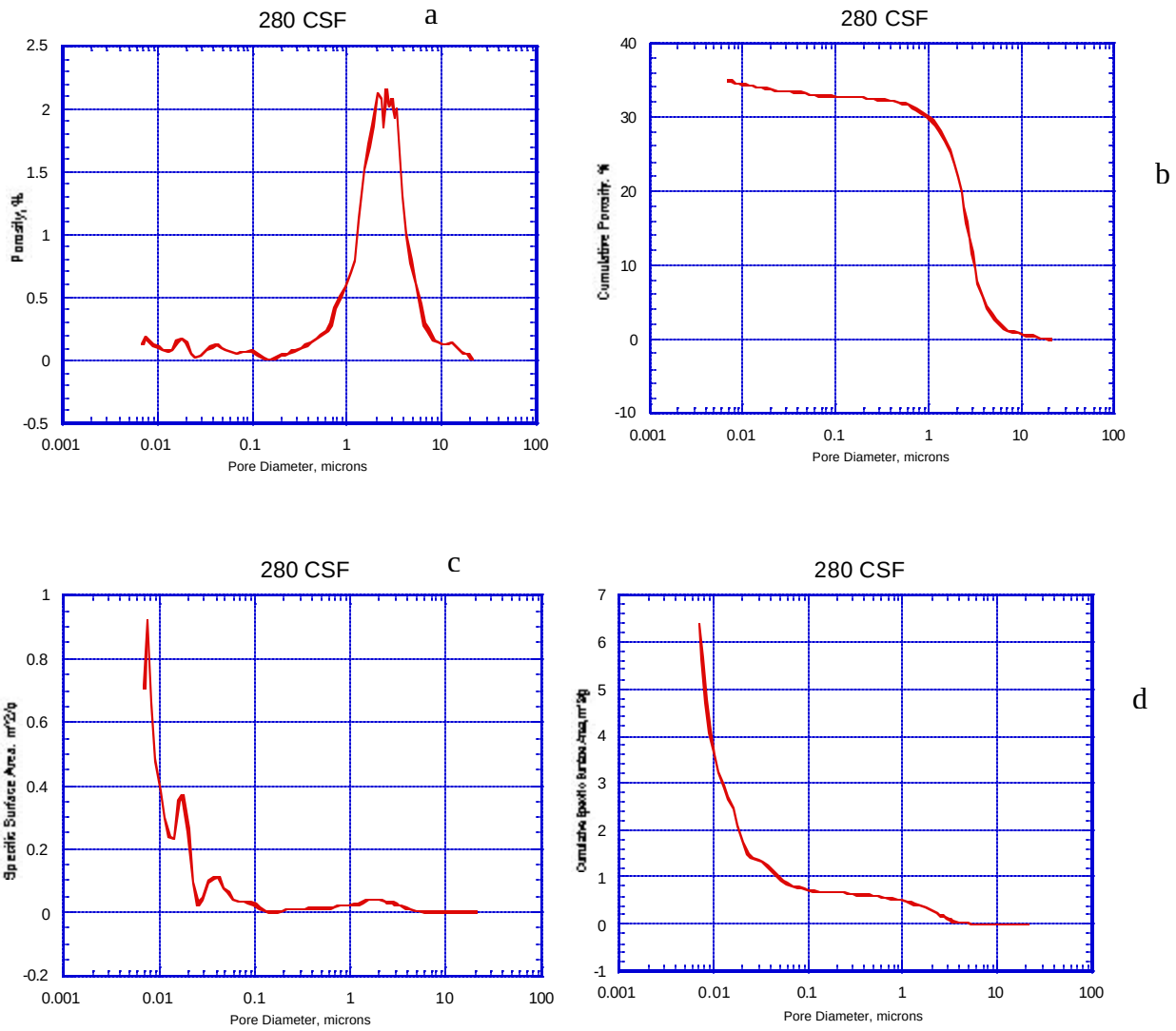

Figure 8 Porosity (a), Cumulative Porosity (b), Specific Surface Area (c), and Cumulative Specific Surface Area (d) distributions by Mercury Intrusion Porosimetry for 280 CSF sample.

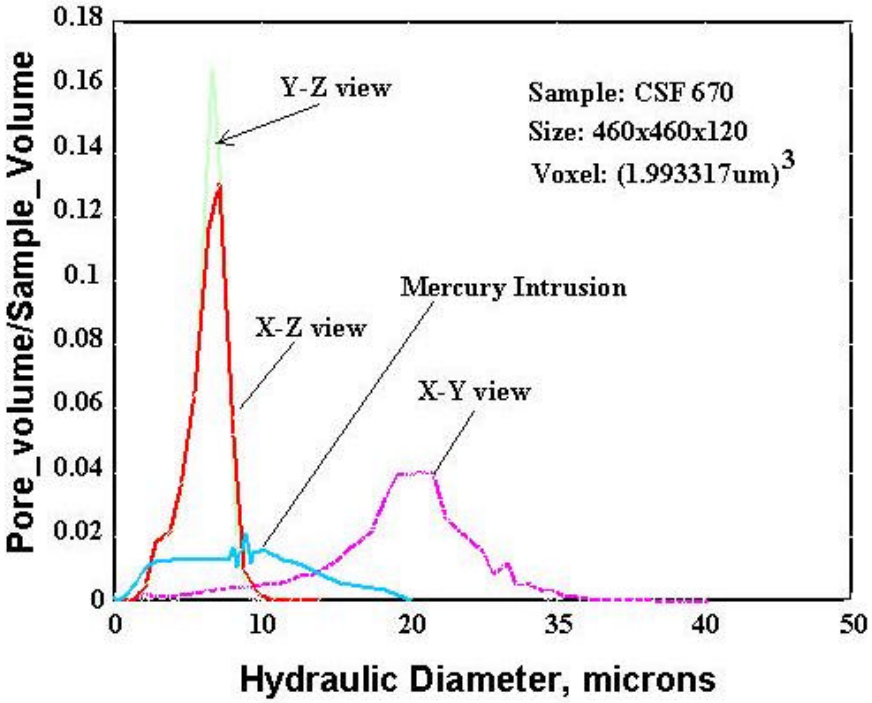

Figure 9. Comparison of pore size distribution in the XY, YZ and XZ planes by image analysis and the mercury intrusion porosimtery for unrefined pulp (670 CSF).

As we go from an unrefined to highly refined sample (Figure (9) vs Figure (10)), the overall pore volume has decreased, as indicated earlier by the porosity values. Also, the pore size distribution shifts towards smaller pore size. But, the distinct difference between in-plane and transverse views is still very much present. The pore size distribution by mercury intrusion, on the other hand, cannot distinguish between the in-plane and transverse views. The mercury intrusion data indicate the narrowing of the pore size distribution with refining, shifting towards the smaller pore size. The pore size distribution by mercury intrusion is more close to the XY view than the other two views. One difference between the X-ray, image analysis and the mercury intrusion technique is that due to the lower resolution of the X-ray technique (~3-4 microns), we are unable to visualize the very small pores in the original image. As a result, the pore volume distribution obtained by mercury intrusion at the small pore size ranges are higher than that obtained by X-ray and image analysis. It is possible that with a higher resolution technique (~1 micron), such as the one used by Samuelsen et.al. [Samuelsen, 1999,Samuelsen, 2001] and Guruyev et.al [Guruyev, 2001] more accurate distributions at the lower pore sizes can be obtained.

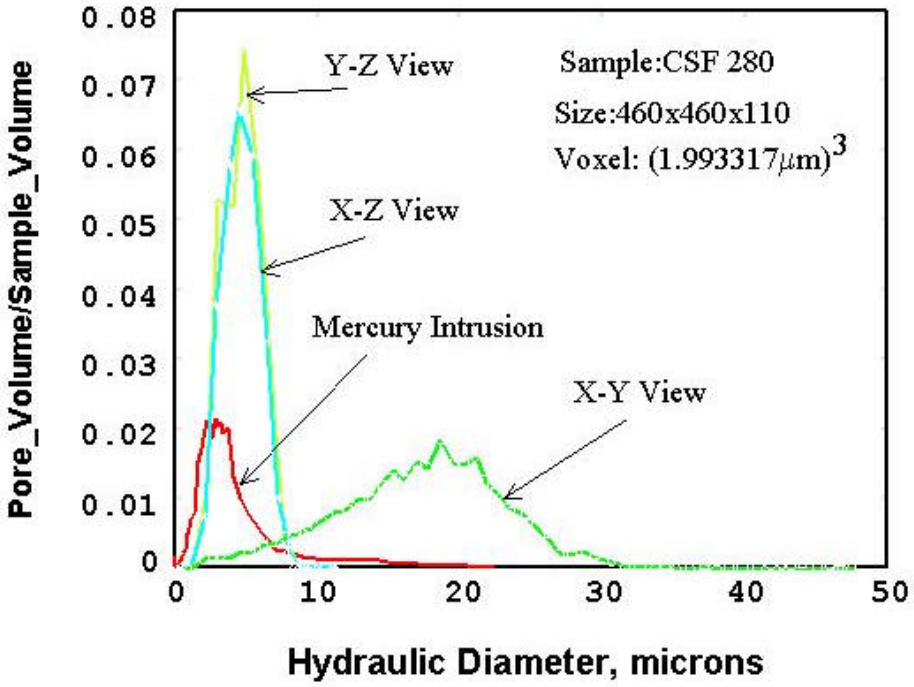

Figure 10. Comparison of pore size distribution in the XY, YZ and XZ planes by image analysis and the mercury intrusion porosimetry for highly refined pulp (280 CSF).

Tortuosity

In addition to classical structure parameters such as porosity, fiber-void interfacial area (surface area) and pore size distribution, one of the other structure descriptor is tortuosity. Tortuosity is defined as the ratio of the actual length of the capillary to the straight line (or the shortest length) length of the capillary. In porous materials such as paper and paperboard, the inter-fiber capillaries can be expected to be highly tortuous. Measurements of tortuosity on a small local scale i.e. between adjacent slices in x-ray images is not very meaningful as the pores are indeed straight on such smaller scale. Then we developed an algorithm to characterize tortuosity for the bulk sample. This algorithm is based on letting tracers (particles) pass through the pores in an actual image of the sample. Starting off on one face of the sample image, the tracers are allowed to traverse through the structure predominantly in a prior decided direction, i.e. in-plane and transverse directions. For example, if the tracer is at some intermediate point in the structure the next step it will take will be in the predominant direction, if that is possible, i.e. if the next voxel in the predominant direction is a pore voxel. If it is not a pore voxel, then a side step will be taken. If none of the other directions are

possible, other than the direction that was taken to come into the current pore, then this will be considered a dead pore and the tracer traverse will be stopped and new tracer is begun from the original face of the image. Since the predominant direction can either be in-plane or transverse, it is possible to obtain independent measurements of in-plane and transverse tortuosity.

Figure 11 and Figure 12 show the trajectory followed by sample tracers as they move through the pore structure in the in-plane and transverse directions. It is interesting to note that in some locations the tracer makes a zigzag pattern while trying to find a way out in the predominant direction. Obviously, due to the complex nature of the 3D pore structure of paper and paperboard, one would expect different values of tortuosity for each tracer. Indeed average values of tortuosity with 10, 100 tracers were quite different. Then continuing this exercise further we found that if the number of tracers were equal or greater than 1000, then the average values of tortuosity were approximately the same.

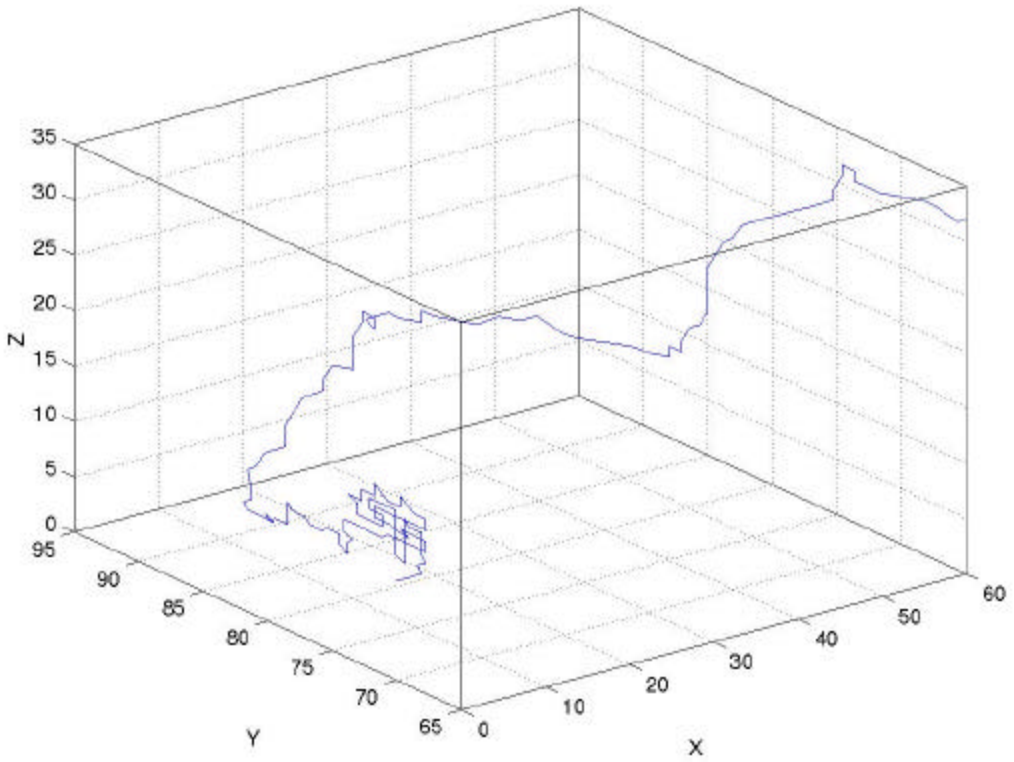

Figure 11. Trajectory followed by sample tracer through the pore structure in the in-plane direction

The average distribution of in-plane and transverse tortuosity values for 1000 tracers for slightly refined sample is shown in Figure 13. As mentioned before, the transverse tortuosity is always greater than in-plane tortuosity. Also, it is interesting to note that the transverse tortuosity has a wider distribution suggesting broader range of tortuosity values.

This exercise was then carried out for six different samples of varying refining levels and structure. The plot of transverse and in-plane tortuosity versus refining or freeness is shown in Figure 14. It is interesting that for all refining levels the transverse tortuosity is always greater than in-plane tortuosity. Also, the difference between in-plane and transverse tortuosity increases as the sheet is more refined. This along with differences in pore size distribution may help explain the observed differences in in-plane versus transverse liquid permeability and vapor diffusivity.

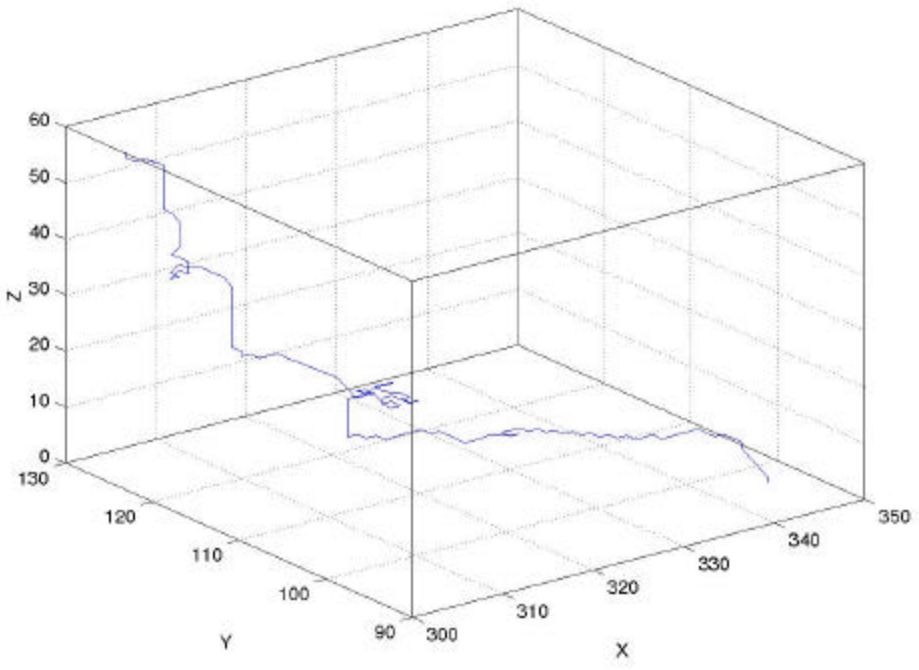

Figure 12. Trajectory followed by sample tracer through the pore structure in the transverse direction

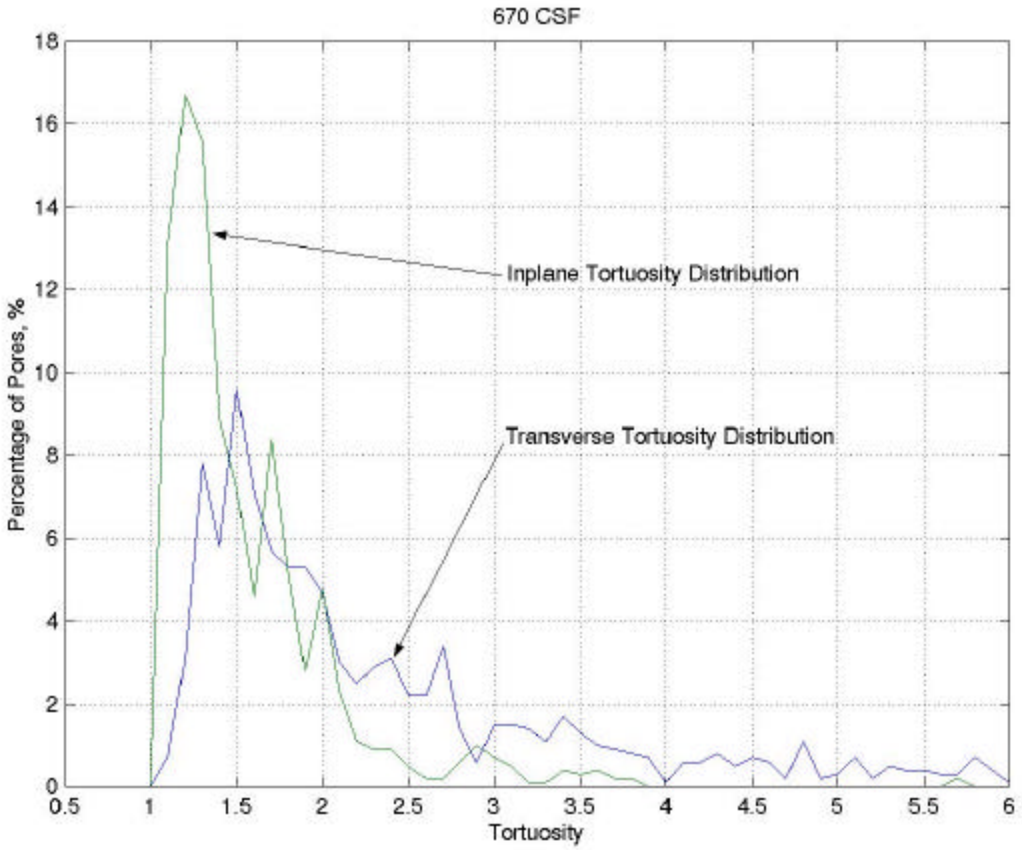

Figure 13. In-plane versus transverse tortuosity distribution for slightly refined sample (670 CSF) (average of 1000 tracers for each direction)

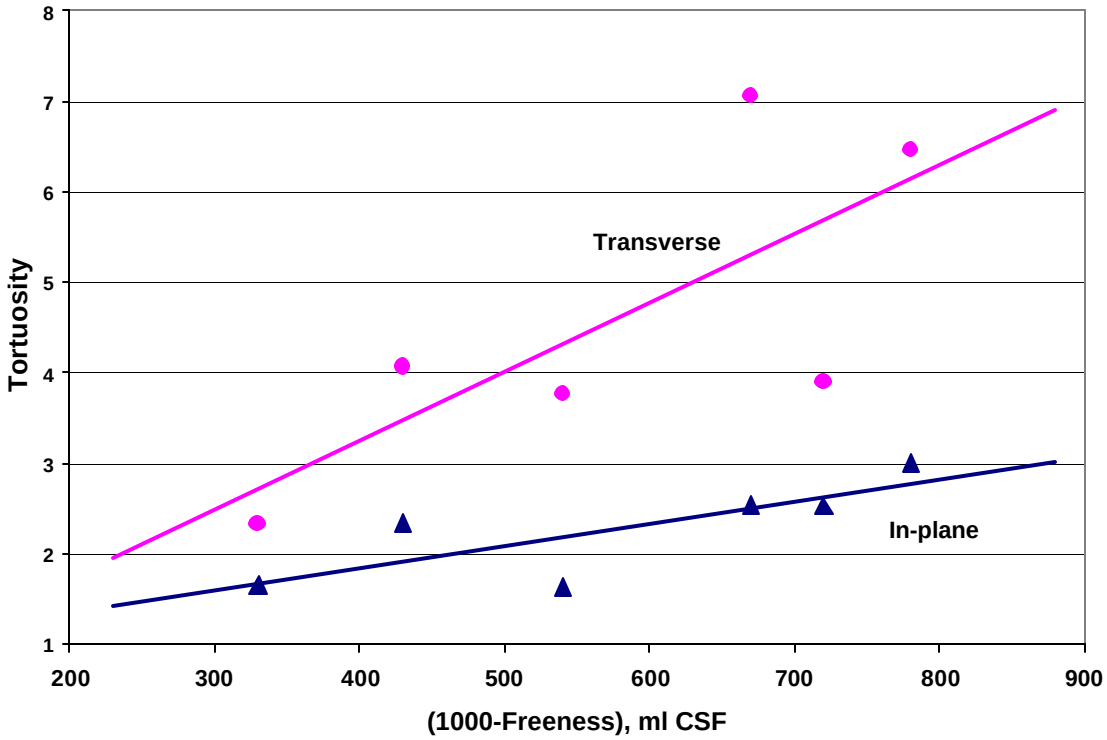

Figure 14. Effect of refining on in-plane and transverse tortuosity (average of 1000 tracers for each direction)

Pore-bond Network Representations

In addition to traditional pore structure analysis using conventional measures such as porosity, specific surface area, pore size distribution morphometric and other quantitative stereological techniques have been used to analyze the three dimensional structure. In this paper, we restrict our attention to the two-dimensional case and consider the three dimensionality in a subsequent report. First, the bi-level images obtained in each of the XY, YZ and XZ planes through the thickness of a given sample are skeletonized by sequential erosion operations without effecting pore connectivity. The skeletonization procedure can be used to minimize either the fiber or the void area to just a single line of pixels representing the original image. Skeletons of fibers and voids overlaid on the original binarized image using Matlab ™ Image Toolkit are shown in Figures 15 and 16. It is interesting to note that the skeletons, in both figures, very closely represent the original fiber and void structure. It should be pointed out that no smoothing algorithm was used in the original bi-level image. As a result, the fiber-void interface is rough with a number of small projections. The skeletons, to some extent, misrepresent some of these projections as short pathways attached to the backbone. A higher resolution X-ray imaging technique in combination with a smoothing algorithm is expected to eliminate some of the rough interfaces and the artifices on the skeleton.

The network structure represented by the skeleton can now be quantitatively described using network nodal density, co-ordination number and bond length distributions. Nodes are defined as points or pixels at which two or more bonds intersect. Skeleton branches coming off a main backbone are also defined as nodes. The node density is defined as the total number of nodes per unit area. Then the node density distribution is the distribution of these nodes in any given slice for a given plane. The co-ordination number is defined as the total number of branches or pathways that can be identified for each of the nodes. The distribution of co-ordination number follows a similar definition as the node density distribution. The bond length and its distribution is then the distribution of the actual distance between two connected nodes. Even though the definition of these pore-bond network structure parameters is simple, the actual calculation of these parameters in a complex structure for paper as shown in any of the images is truly challenging.

The skeletonized image of pores, for example, consists of a large two-dimensional matrix of zeros and ones representing each pixel, one being the skeleton and zero being the non-skeleton. The algorithm for node density and co-ordination number determination begins by looking at every pixel to see if it is part of a skeleton. If a pixel is part of the skeleton,

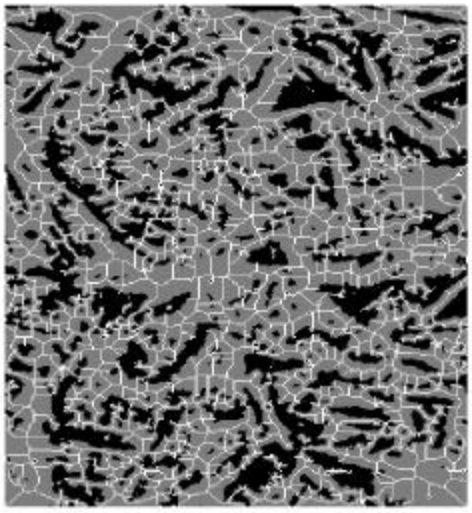

Figure 15 Skeleton of fiber over laid on binarized image

Figure 16 Skeleton of pores over laid on binarized image

i.e. it has an intensity of one, a search is done to see how many individual paths following the skeleton out to the edge of a box surrounding the original pixel can be found. If three or more of these paths are found then this pixel is considered to be a node, and the co-ordination number of the node is equal to the number of individual paths found. In order to avoid counting a node more than once and to avoid clusters of pixels surrounding a node, an artifact of the imaging and skeletonization procedure, a small number of pixels surrounding an identified node is cleared or given an intensity value of zero. A visual comparison of the nodes with the skeleton analysis indicated that this procedure worked quite well in both identifying nodes and eliminating clusters. The node density is found by searching each slice in 40 pixel by 40 pixel segments and then dividing the number of nodes found in each segment by the area of the segment.

A typical average node density distribution and co-ordination number distribution in the XY plane for a unrefined (670 CSF) and highly refined sample (220 CSF) are shown in Figures 17 thru 20 respectively. As shown in the figures, node density distribution for unrefined sample appears to be broader with a bigger range than the highly refined sample. A similar behavior was observed in the YZ and XZ planes as well. The frequency distribution of co-ordination numbers appears very similar for the both the sheets. A similar behavior, again, was observed with other planes as well.

A plot of the average node density and co-ordination number for a given plane for the entire thickness of a sample versus freeness shows an interesting behavior (c.f. Figure 21 and Figure 22). Increasing the level of refining or increasing the density of the sheet appear to decrease the average node density and average co-ordination number. This trend is very similar to what was observed with change in porosity and specific surface area with refining. One would expect with refining and

higher density sheet, there is a larger number of smaller pores, as shown by pore size distribution. If this were the case then the node density would be expected to increase with refining. On closer observation of the results and the skeletons, it appears that the greater the number of larger pores (as in unrefined sheet) with more imperfections or rough edges, the skeletonization routine converts this into an image containing long skeleton backbones with many loose branches attached to it. As a result, the node density and the co-ordination number is greater for a unrefined sheet as compared to a highly refined sheet. This again would be an artifact of the resolution of the X-ray imaging technique. As mentioned earlier, with a higher resolution X-ray technique and employing a smoothing algorithm may solve this problem.

In conclusion, in addition to the traditional methods of describing the void space in paper, the topological complexity can be reflected in morphometric measures including node density, co-ordination number and bond length distributions. The methodology presented here appears to work well even with dense, highly refined sheets. The accuracy of this method can be further improved with a higher resolution X-ray technique. Efforts are underway in obtaining high resolution images and relating pore structure descriptors to liquid and vapor transport.

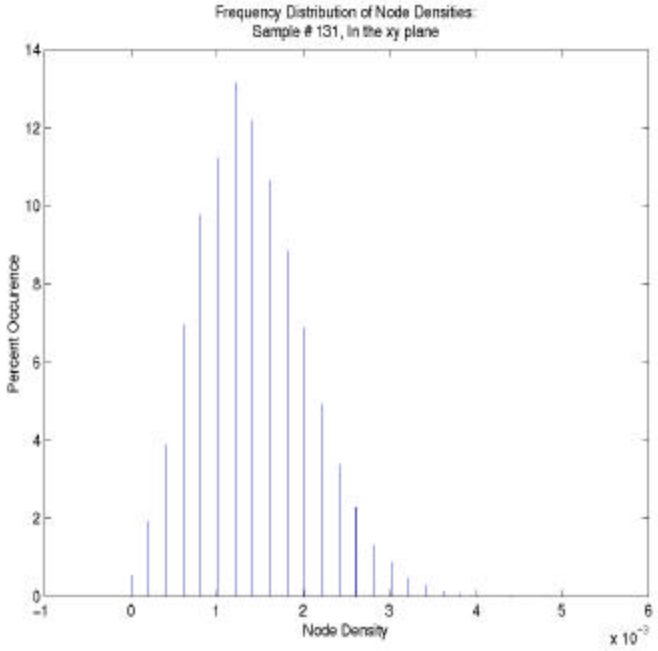

Figure 17. Average node density distribution in the XY plane for unrefined sample

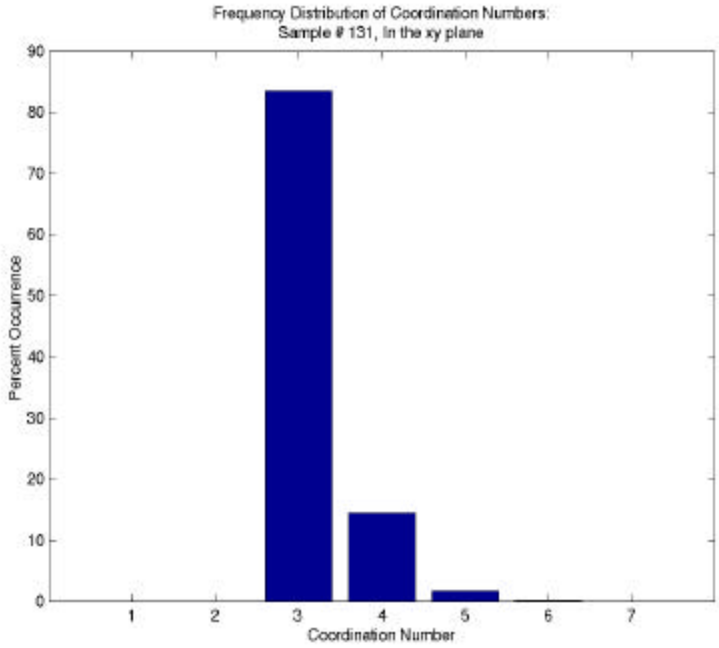

Figure 18. Average co-ordination number distribution in the XY plane for unrefined sample

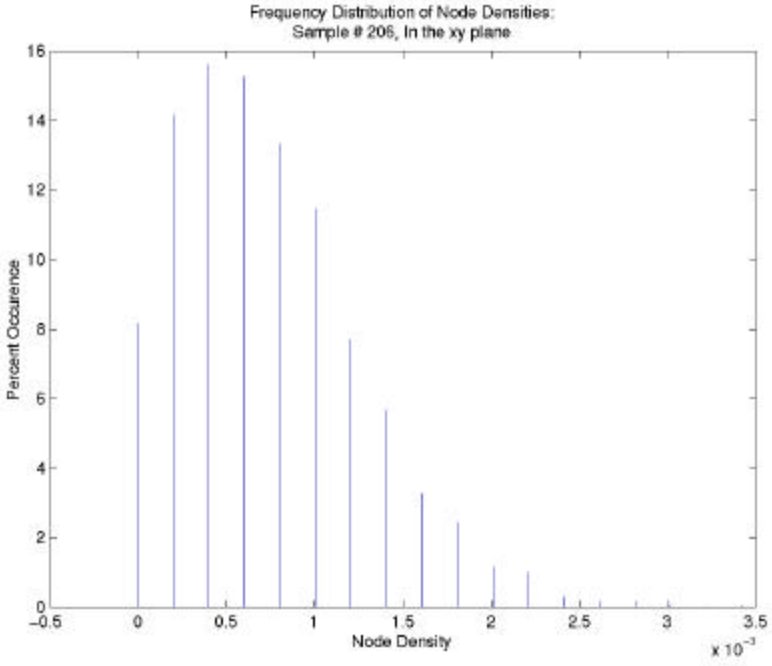

Figure 19. Average node density distribution in the XY plane for highly refined sample

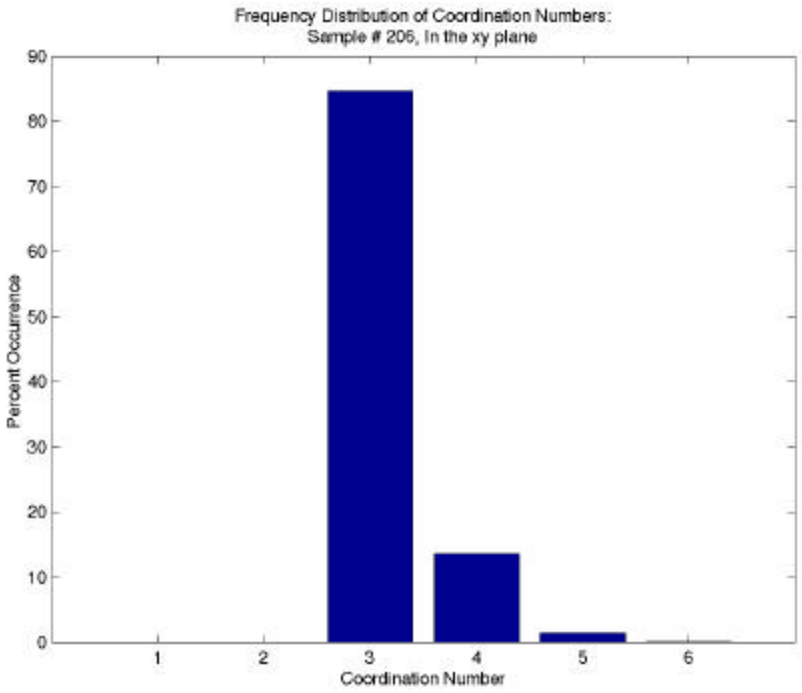

Figure 20. Average co-ordination number distribution in the XY plane for highly refined sample

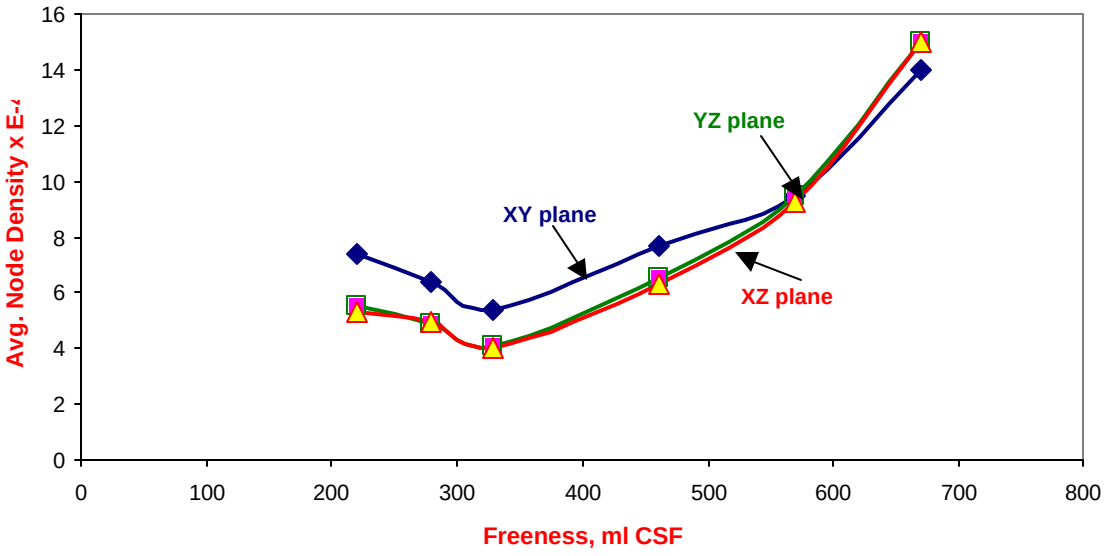

Figure 21 Effect of refining on average node density for all three planes.

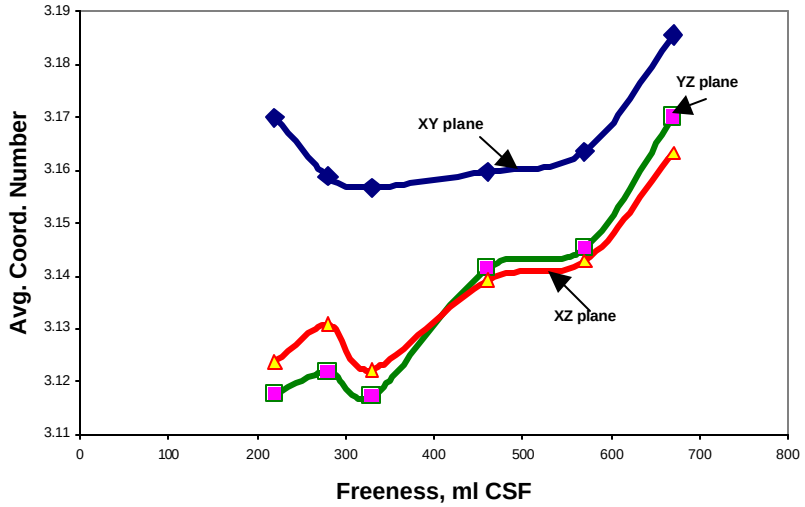

Figure 22 Effect of refining on average coordination number for all three planes.

Comparison between commercial sheets and laboratory made hand sheets - Z-D structure characterization

300 g/m^2 hand sheets of varying structures were prepared by refining bleached softwood kraft pulp to different extents (Tappi test method T-205). Commercial samples used in this work are writing and printing paper samples manufactured in North America. Sample micro-CT scanning and reconstruction was done with SkyScan-1072 system developed and manufactured by SkyScan, Belgium and distributed by Microphotonics, Allentown, PA.

Direct quantitative evidence for the z-directional structural characteristics of commercial machine made fine paper (writing and printing) and hand sheets of varying structures are reported here using X-µCT and image analysis techniques. Traditional descriptors such as porosity, fiber-void interfacial area (specific surface area), tortuosity, pore size distribution in the two orthogonal directions are reported for sections through the thickness direction.

Porosity (ratio of void volume to total volume) comparison between hand sheet (280 CSF) commercial fine papers clearly indicate that while the hand sheet is more uniform the commercial structures do indicate a substantial difference between the top, middle and bottom (Figure 23) potentially owing to the non-uniformity during formation. Each of the sections (top, middle, bottom etc.) of the commercial fine paper samples reported here are approximately 16 microns in thickness while the hand sheet sections are 32 microns (due to the higher basis weight of hand sheets). The Z-directional fiber-void interfacial area distribution shows a similar comparison between the hand sheet and commercial sheets (Figure 24).

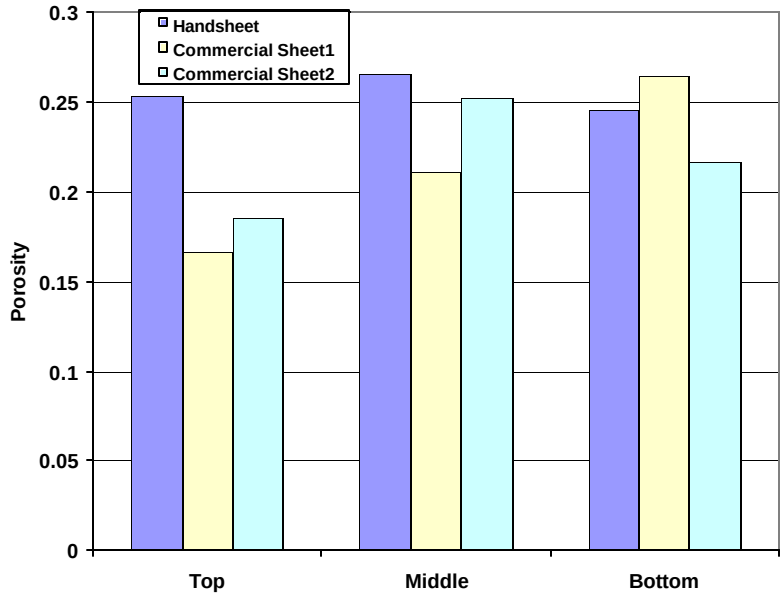

Figure 23. Z-D porosity distribution for hand sheet and commercial sheets

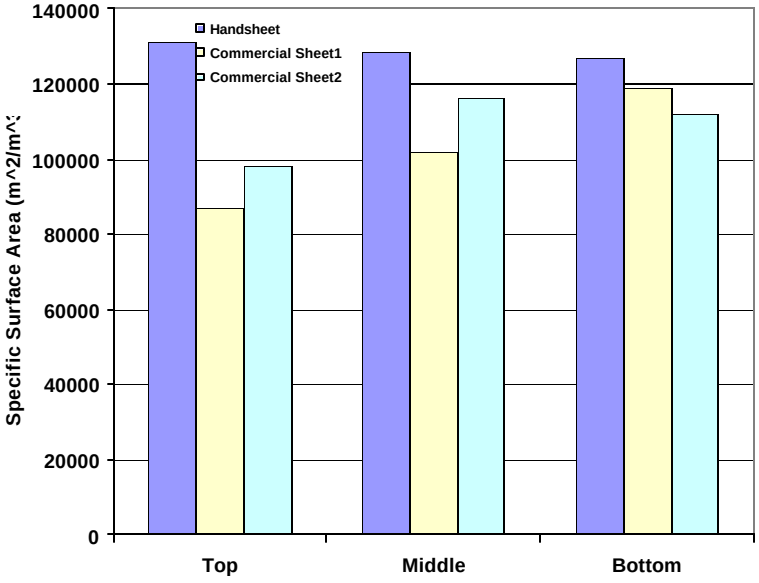

Figure 24. Z-D specific surface area distribution for hand sheet and commercial sheets

Interestingly commercial machine made papers show distinct differences in the structural characteristics through the thickness direction depending on the quality of the sample, while hand sheets exhibit rather uniform distribution.

Similarly, the transverse and in-plane pore size distributions through the Z-direction for the commercial fine paper sample do indicate distinct differences between the top, middle and bottom sections (Figures 25 and 26). Hand sheet (670 CSF), on the other hand, even though exhibiting a wider distribution of larger pore sizes in the transverse direction, clearly show approximately identical, uniform distribution uniform through the thickness. Interestingly, both the commercial sheet and hand sheet show approximately similar range of pore size in the in-plane direction (1 to 4 microns) indicating that the both the commercial and hand sheet forming produce structures which are similar in the in-plane direction. This was seen again with refined hand sheet sample as well.

Also, the in-plane and transverse pore structure characteristics of hand sheets exhibit significant differences with the transverse structure being more open with wider distribution. The commercial sheets, however, do not show quite as significant differences between the in-plane and transverse planes suggesting that commercial paper making process under dynamic conditions may produce a structure which is more similar in the two principal directions. This may have potential significant implications with regard to differences in transport, mechanical and optical properties of commercial sheets between the orthogonal directions.

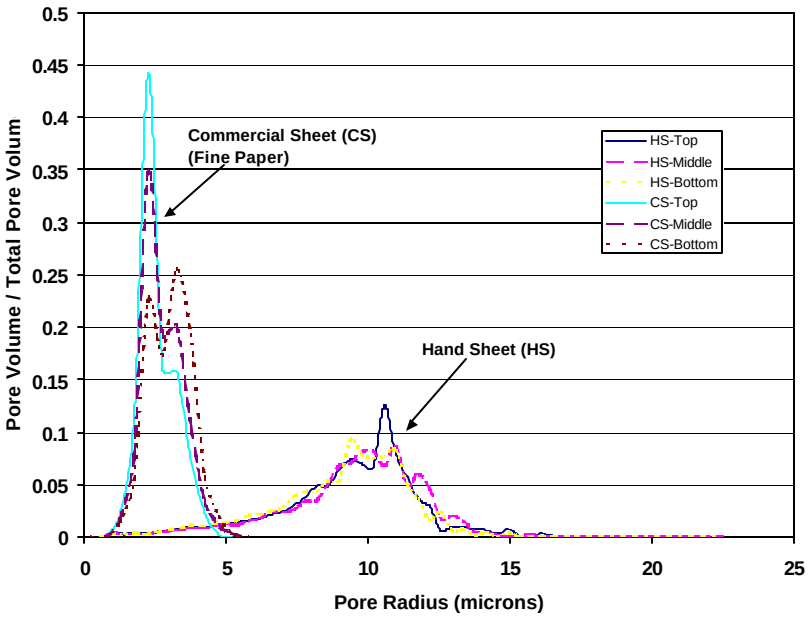

Figure 25. Z-directional transverse pore size distribution comparison between hand sheet and commercial fine paper

The differences between hand sheet structure and commercial sheet structure are also elucidated by distinct porosity-tortuosity relationship for the two structures. Commercial sheet structures even though have lower porosity (similar to highly refined hand sheet (280 CSF) in this study) and a lower range of pore size (Figure 25) the tortuosity values are also lower confirming a more open,

less tortuous structure (Figure 27). Again this could be due to the dynamic forming conditions on the paper machine with more fiber aggregates resulting in a less tortuous structure. Also, similar to porosity, surface area, pore size distribution, the mean tortuosity values were also found to vary through the thickness for commercial samples while remaining almost same for hand sheets. The porosity-tortuosity relationship is characteristic of a given structure and hence can provide a quantitative tool to benchmark existing paper making systems and to engineer paper structures.

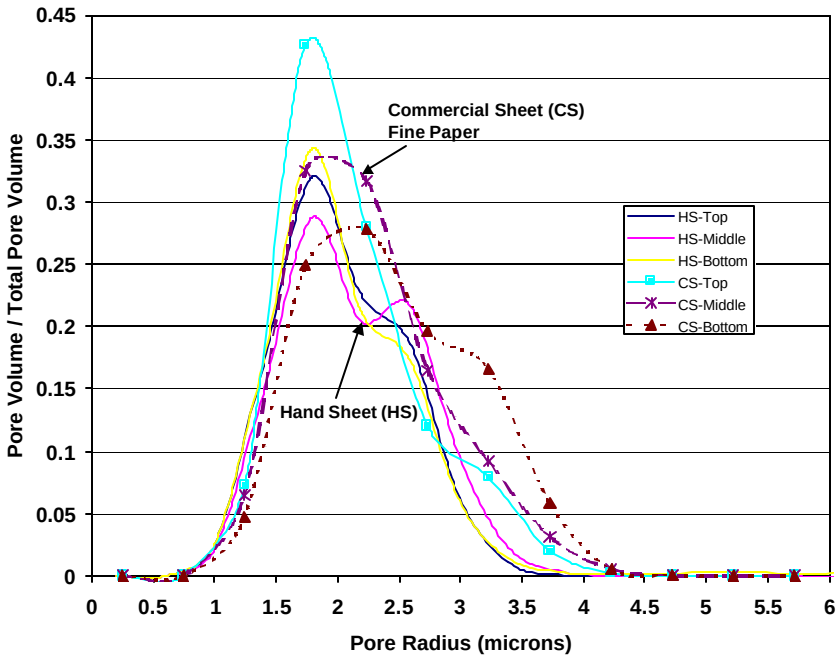

Figure 26. Z-directional in-plane pore size distribution comparison between hand sheet and commercial fine paper

Permeability

Using the 3D structural characteristics of the commercial and hand sheet structures the permeabilities were also estimated for low Reynolds number fluid flow through porous medium using Darcy's law [Scheidegger, 1974].

$$\vec{q} = -\frac{k}{m}\vec{\nabla} p, \qquad \text{Eq. 3.}$$

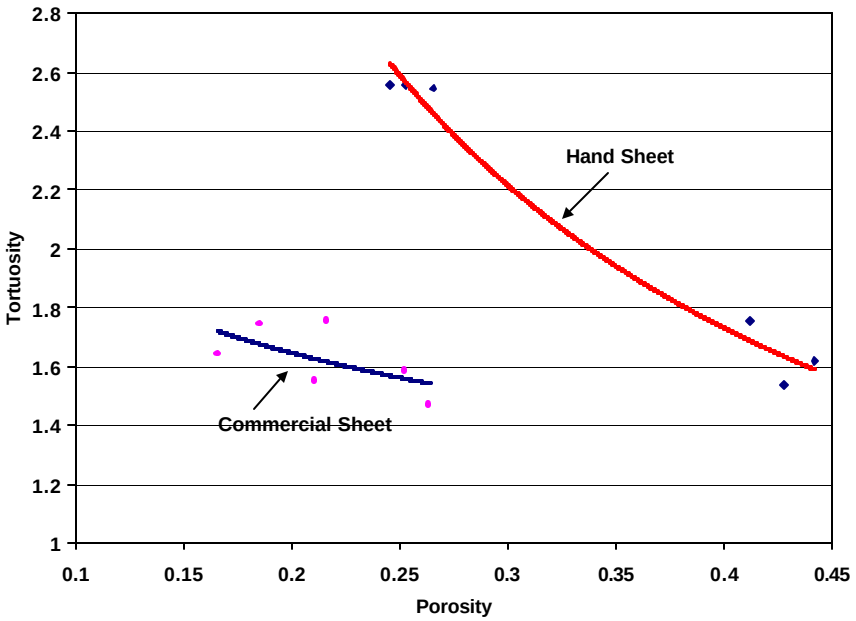

Figure 27. Effect of porosity on tortuosity of commercial and hand sheet structures

where $\vec{q}$ is the fluid flow velocity, m is the dynamic viscosity of the fluid and *p* is the fluid pressure. The permeability coefficient k measures the conductivity to fluid flow of the porous material, and is unknown, *a priori*. The most widely used formula that relates permeability with the relevant structural characteristics of the porous material, is the Kozeny-Carman equation [Scheidegger, 1974]

$$k = \frac{1}{ct^2 S_0^2} \frac{f^3}{(1-f)^2}. \qquad \text{Eq. 4}$$

Here f is the porosity, S_0 is the pore surface area in a unit volume of solid material, t is the tortuosity (i.e. the ratio of the average length of flow path to the thickness of the sample), and c is the dimensionless Kozeny's constant.

Using the above Kozeny-Carmen equation and the pore structure parameters including tortuosity obtained from X-ray tomography and image analysis the fluid permeability was then calculated. This method has been shown to agree reasonably well with lattice-Boltzmann simulations of fluid permeability for samples of varying structures (Aaltosalmi, 2003).

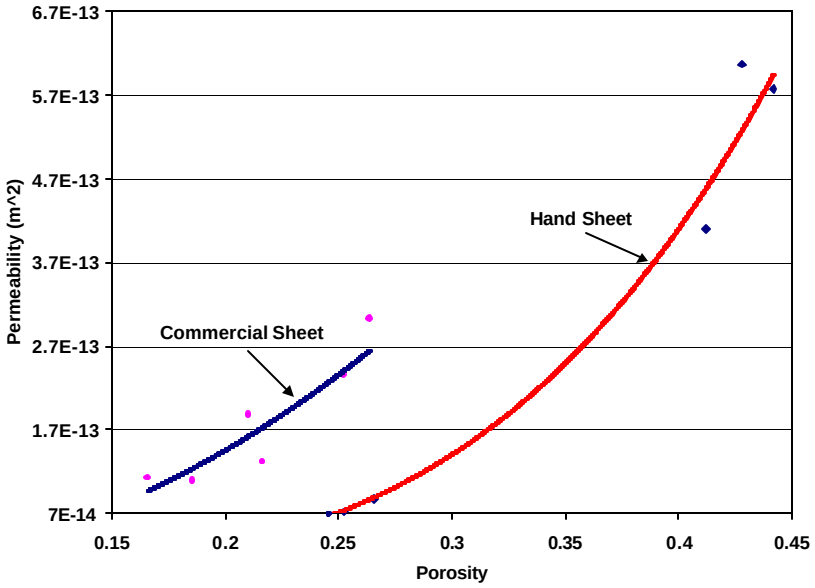

Figure 28. Effect of porosity on transverse permeability of commercial and hand sheet structures

As shown in Figure 28, the transverse permeabilities of hand sheet and commercial sheets show distinctly different relationships with porosity suggesting again different characteristic structures of each of the materials studied here. Commercial structures even at lower porosities tend to have higher permeabilities than hand sheets at the same porosity. This again suggests a more open, less tortuous structure for fluid flow even at relatively low overall porosities. This relationship again can be used to characterize paper and board made from a given paper making system and to engineer products for specific end-use applications.

Effect of papermaking processes on 3D structure: wet pressing versus vacuum dewatering

In tissue and towel manufacture, one of the key product properties is bulk. Increased bulk or decreased density is often accomplished by eliminating mechanical pressing of the sheet and instead replacing it with vacuum dewatering and through air drying. Here, we report the effect of wet pressing and vacuum dewatering on the internal sheet structure of paper using x-ray microtomography and image analysis.

Figure 29 shows the porosity comparison between wet pressed and vacuum dewatered samples. As we expect, the wet pressed samples have a lower porosity than the vacuum dewatered samples. WP1

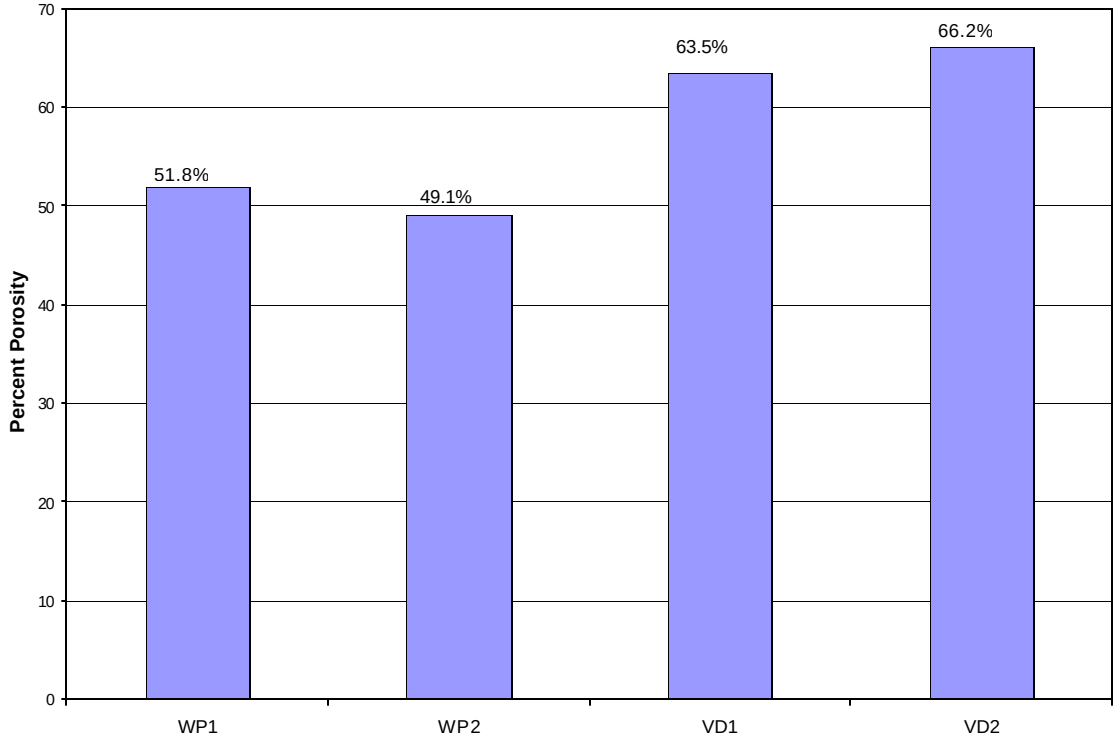

Figure 29. Porosity comparison between wet pressed and vacuum dewatered sheet structures

and WP2 represent two different samples of the same wet pressed structures. Vacuum dewatered sheets appear to be approximately 30% more open (higher porosity) than the wet pressed structures.

Figure 30 shows the specific surface area comparison for the wet pressed and vacuum dewatered sheet structures. Here again, the more open vacuum dewatered sheets have higher specific surface areas compared to the pressed sheets (approximately 50% higher specific surface area).

Fig. 31 and 32 show the pore size distribution obtained by image analysis in the XY, YZ and XZ views for two different structures (wet pressed versus vacuum dewatered). It is interesting to note that for any given sheet structure, the pore size distribution in the XY (or transverse) view is broader than the YZ or XZ views (in-plane views). The average pore size in the XY view is also larger than the other two directions. This indicates that potentially the fluid flowing in the transverse direction encounters a much more open pore structure with larger pore sizes compared to the in-plane direction. This may help partly explain the differences observed in in-plane vs transverse permeability experiments. The wet pressed sheet with closed, denser structure and lower porosity (49%) has a different pore size distribution in the in-plane and transverse directions (Figure 31) as compared to the more open, vacuum dewatered sheet (Figure 32) (higher porosity, 63%). As we go from a vacuum dewatered to a wet pressed sheet structure (Fig. 32 and 31), the pore size distribution shifts towards smaller pore size and the overall pore volume has decreased, as also indicated by the porosity values. But, the distinct difference between in-plane and transverse views is still very much

present. It is very interesting to note that the pressed sheet has a broader pore size distribution than the vacuum dewatered sheet. It is important to note that traditional methods such as mercury intrusion porosimetry can only give bulk pore size distribution information and can not distinguish between the in-plane and transverse directions. Comparison of our results using x-ray tomography and image analysis and traditional mercury intrusion porosimetry for samples of varying refining levels did indicate the narrowing of the pore size distribution with refining, shifting towards the smaller pore size. The pore size distribution by mercury intrusion was observed to be more close to the XY view than the other two views. One difference between the x-ray, image analysis and the mercury intrusion technique is that due to the lower resolution of the x-ray tomography technique used here (~4 microns), very small pores cannot be visualized by the current set-up. As a result, the pore volume distribution obtained by mercury intrusion at the small pore size ranges are higher than that obtained by x-ray tomography and image analysis. It is possible that with a higher resolution x-ray tomography (~1 micron) more accurate distributions at the lower pore sizes can be obtained.

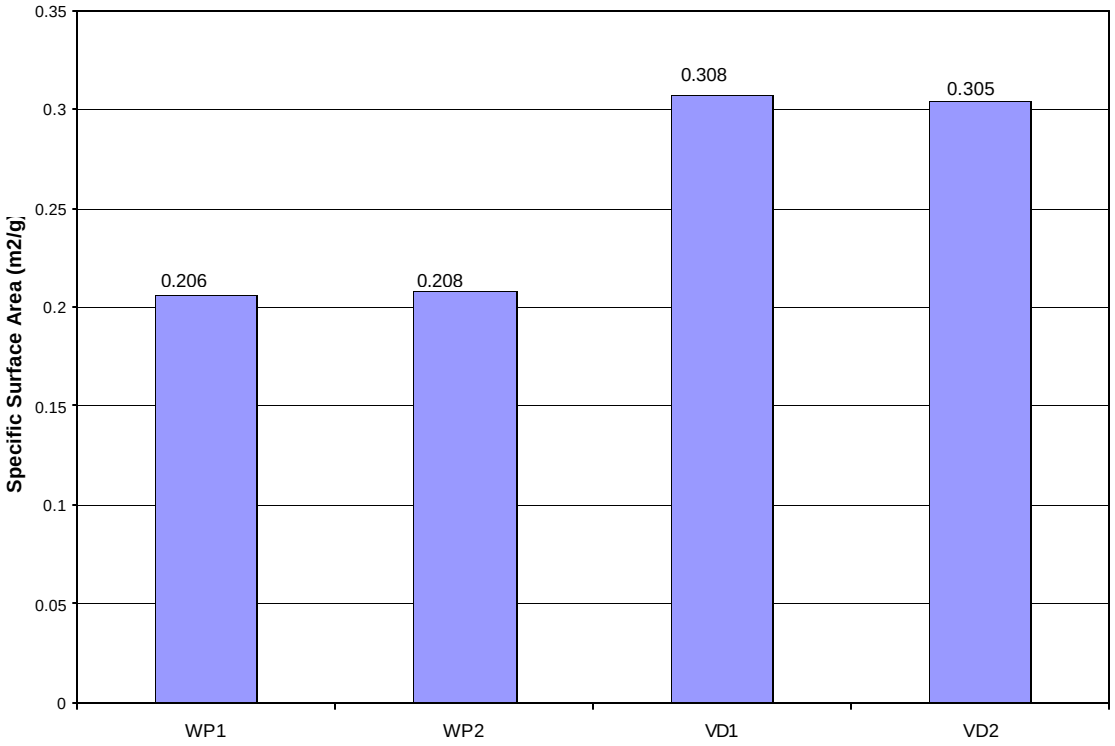

Figure 30. Specific surface area comparison between wet pressed and vacuum dewatered sheet structures

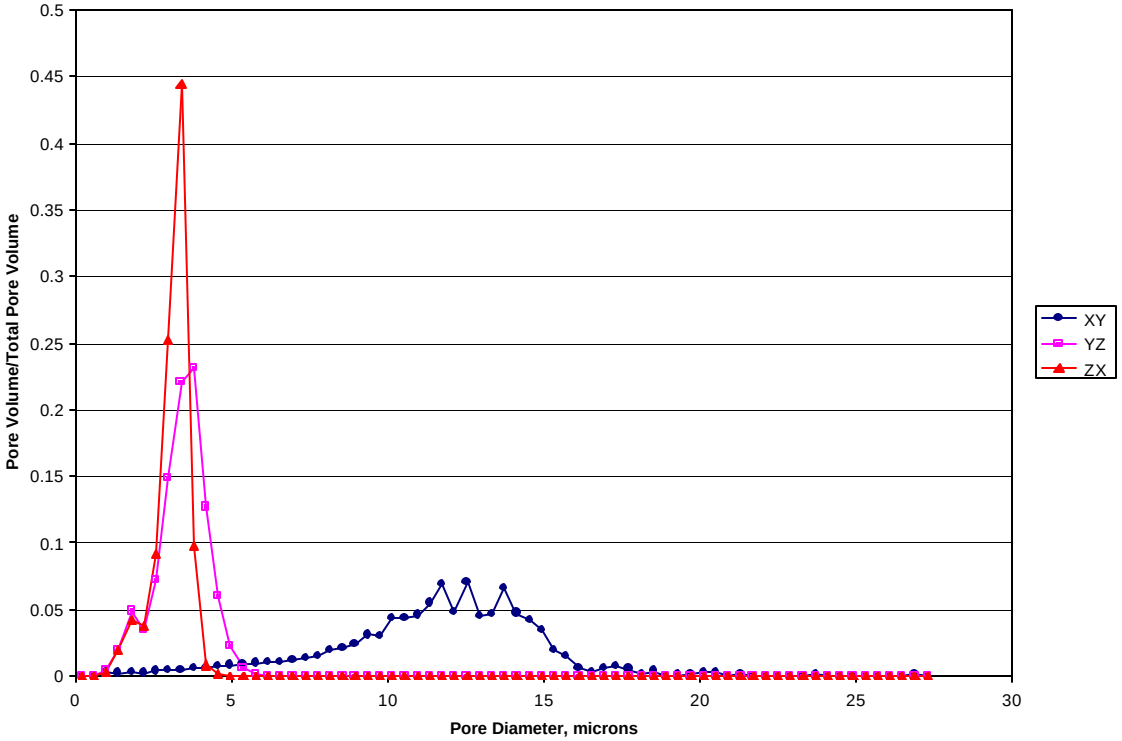

Fig. 31. Comparison of pore size distribution in the XY, YZ and XZ planes by image analysis for wet pressed sheet.

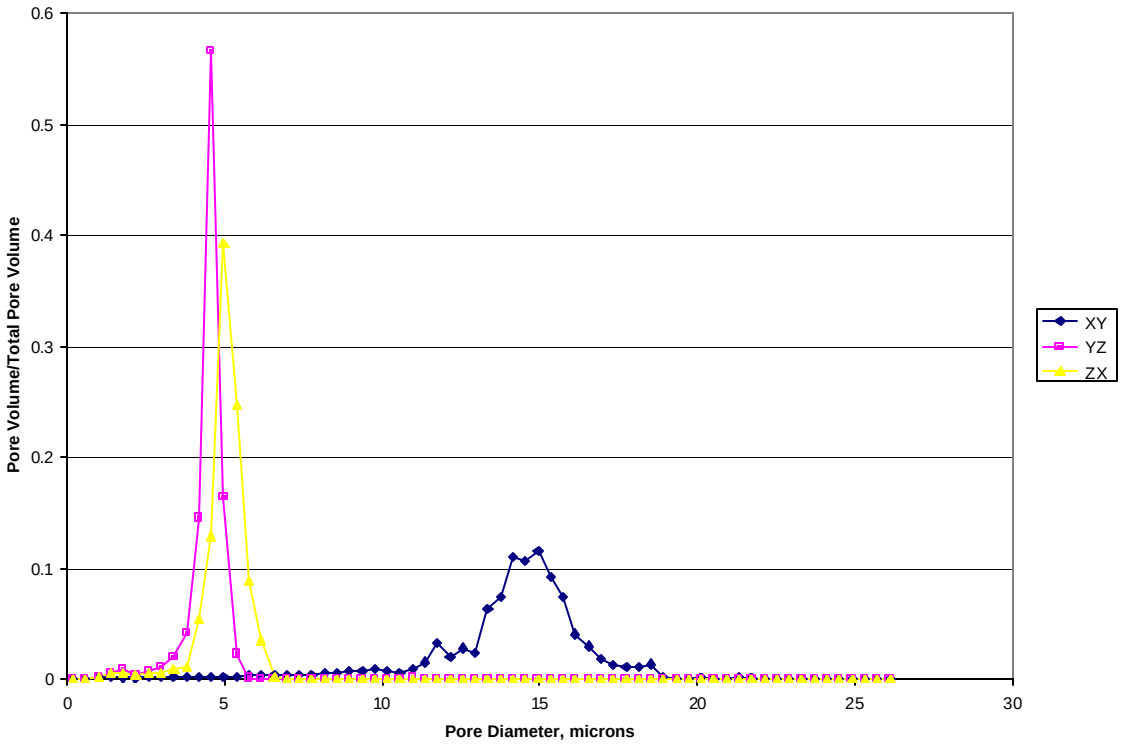

Fig. 32. Comparison of pore size distribution in the XY, YZ and XZ planes by image analysis for vacuum dewatered sheet.

COMPARISON OF 3D STRUCTURAL CHARACTERISTICS OF HIGH AND LOW RESOLUTION X-RAY MICROTOMOGRAPHIC IMAGES OF PAPER

One of the most important questions that need to be answered for successful application of a given technique is whether the technique is capable of giving images of sufficient quality and resolution to enable a reasonable quantification of the different 3D structural characteristics. As a first step towards identifying the necessary level of structural detail, we report here visualisation and 3D structural characterisation of images of paper samples obtained using both high- and low-resolution *X-mCT*. The paper samples were originally chosen to test the applicability of the phase contrast synchrotron radiation *X-mCT* to depict paper made from different raw materials. The high-resolution images from *X-mCT* represent physically small volumes, limited by the screen size of the detecting CCD screen and computational requirements. To enable a direct comparison, volumes having the same physical size (surface area) as the high-resolution images were created from the low-resolution images. The volumes were chosen small enough in the high-resolution images to avoid areas with edge artefacts. Additional data sets were also created from the low-resolution images, to give the largest paper volume available in the 3D images without including any edge artefacts. The size of the cross-section in the given direction will influence the result for some of the applied image analysis routines.

The paper samples were imaged by both monochromatic synchrotron radiation *X-mCT* in phase contrast mode (Samuelsen, 2001, Weitkamp, 2002) (resolution ≈ 1 μm, voxel = $\{0.35\ \mu m\}^3$) and polychromatic radiation *X-mCT* (Huang et al. 2002; http://www.skyscan.be/next/methods.htm) (res. ≈ 5 μm, voxel = $\{2\ \mu m\}^3$). The images were obtained at the synchrotron facility at ESRF, Grenoble and using a SkyScan-1072 system respectively. The low availability and high cost of obtaining high-resolution measurements limited the number of images to a single data set. As the availability is higher and the cost is lower, two data sets were obtained using low-resolution technique to improve the representativity.

The images were reconstructed and processed according to the routines from previous work on low (Huang, 2002) and high (Antoine, 2002) resolution 3D images from *X-mCT*. Additionally were detached volumes of fibrous and porous phase smaller than 216 μm^3 removed by a 3D filtering technique. In order to include the surface areas of the volumes, the surfaces were defined using the rolling ball algorithm (Aronsson, 2002).

The measured 3D structural characteristics were porosity, specific surface area, diffusive tortuosity and hydraulic pore radii distribution in the principal directions. The image analysis routines were based on the principles in previous work on analysis of low-resolution 3D images of paper (Ramaswamy, 2001, Huang, 2002). There was one major exception from these principles; a definition of the surface with the rolling ball algorithm to include the surface area. The diffusive tortuosity measurements were based on 1000 successful paths through the paper volume with a random starting point on the appropriate volume edge. In addition, we used the numerical lattice-Boltzmann method to compute the flow permeability and the tortuosity of flow paths for fluid flow through the samples. The results allow an interesting comparison of the 3D structural characteristics of low- and high-resolution images and provide insights into the level of structural details required for predicting optical, transport and mechanical properties of paper and board.

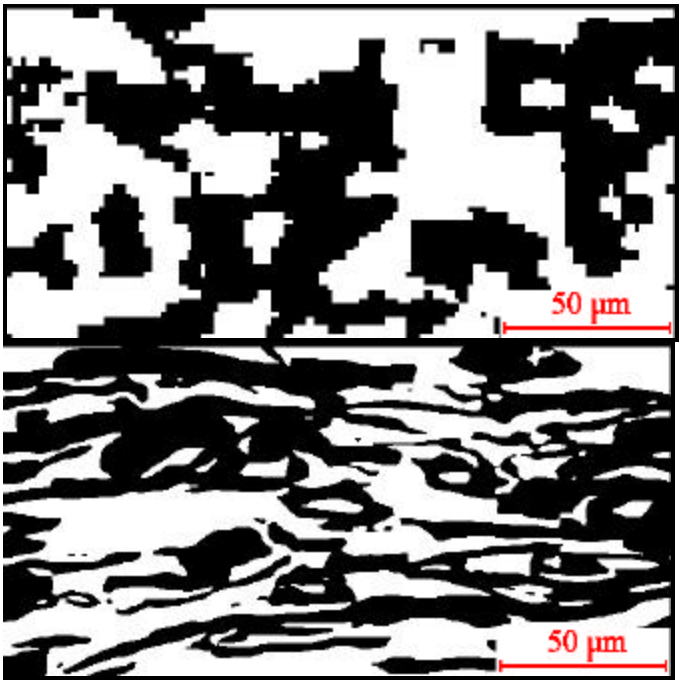

Figure 33: *Top:* Part of a binarised cross-section with low resolution. *Bottom:* Part of a cross-section with high resolution. Fibres are black and voids are white.

There is a clear difference in appearance of the images obtained with the two different resolutions, as seen in Figure 33, where the two cross-sections represent the same physical size of the newsprint paper. The difference is even clearer when looking at the binary volumes in a 3D perspective in Figures 34 and 35. The two volumes represent the same physical size, except thickness, for the newsprint sample. It is clear from the visual comparison, that the high-resolution technique preserves the topology of the fibrous and porous structure better than the low-resolution technique. The observed difference may influence the measurements done on the 3D images. It is also likely that the higher level of detail in the high-resolution images makes the images more suitable for predicting optical properties through modelling of the light scattering in the digital paper structure. For optimal modelling it is desirable to get a resolution equal to or lower than half the wavelength of visible light (= 0.2 µm) to detect all optically active surfaces in the paper structure.

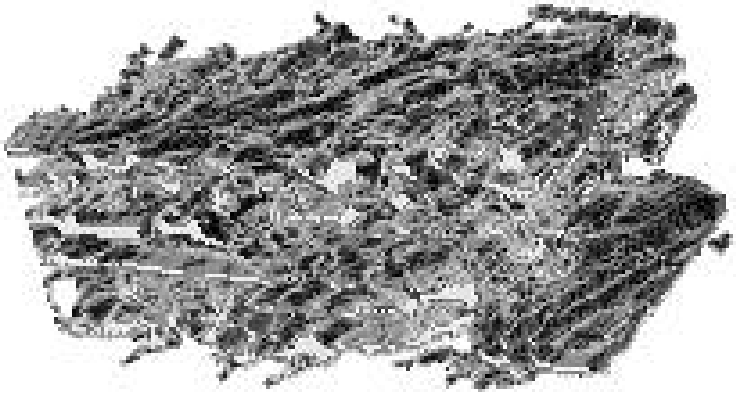

Figure 34: Low-resolution 3D image of a newsprint sample. (The size of the image is kept smaller than for the high resolution image due to the considerably physically larger voxels in the 3D image. However, the physical size of the volumes are equally large).

Figure 35: High-resolution 3D image of a newsprint sample.

The pore size distribution is determined as the hydraulic radius, as seen going through the volume in the principal directions. The hydraulic radius is defined as the ratio between pore area and perimeter. The resolution and image size are expected to influence both.
The influence of resolution can be seen from the hydraulic pore radii distribution in Figure 36.

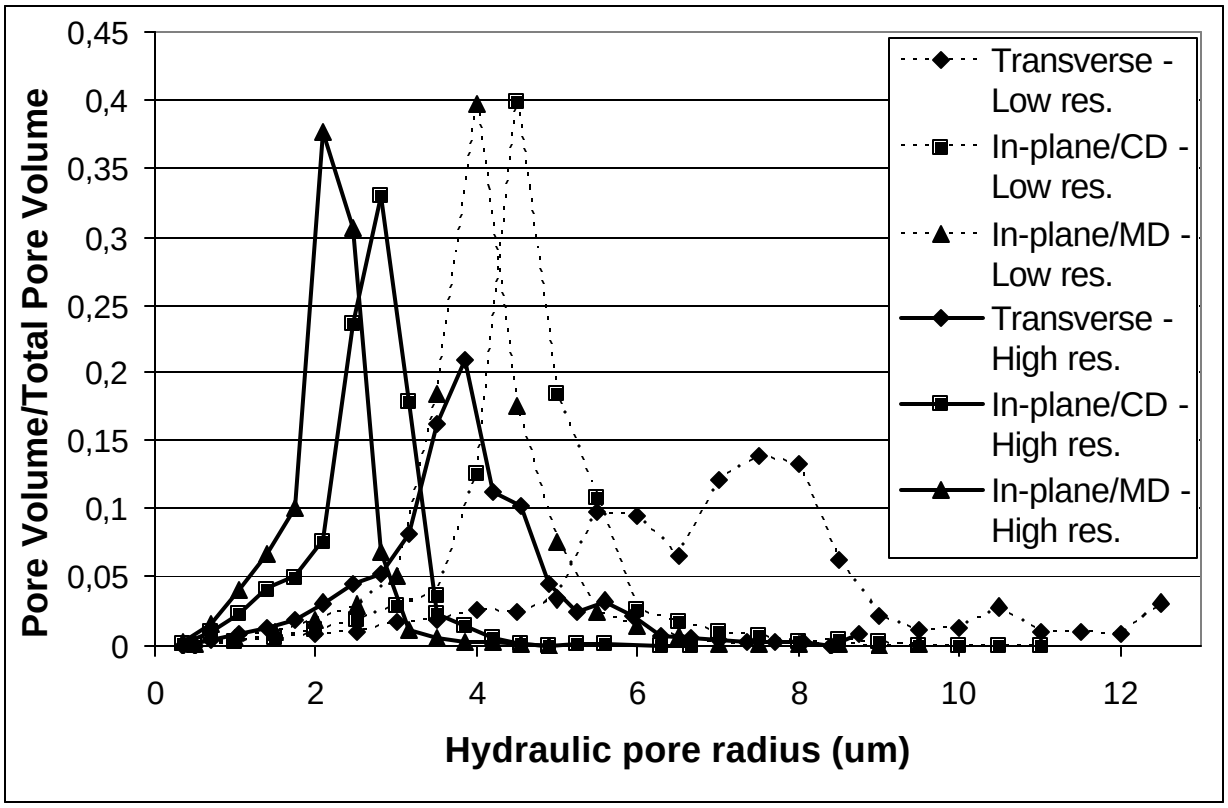

Figure 36: Hydraulic pore radii distribution for newsprint samples. The thicker lines show the distributions in the principal directions for the high-resolution images.

The distributions in Figure 36 clearly shift towards lower hydraulic radii when the image resolution is increased. As the measured pore area is less likely to be influenced by the resolution, the shift is most probably caused by a longer pore perimeter. A longer perimeter can be expected when the resolution is increasing. This is a well known phenomenon, *e.g.* when measuring the coast line of a country on a map. The high-resolution images will thus show more correct values, although both imaging methods are capable of getting the right ratio between the distributions and more or less the same shape on the distributions. The low-resolution images, are as for other parameters, more exposed to noise.

The pores will be limited by the edges of the cross-sectional images, as the majority of the pores are interconnected and stretching out of the boundaries in the physically small cross sections. This will affect the measured hydraulic radii, and the magnitude of the effect is dependent on the image size. The influence of image size can be seen in Figure 37, which shows the hydraulic pore radii distribution for hand sheet in low resolution with small and large volume size. The increased volume size causes generally larger hydraulic radii as the edge effect is reduced. Presumably, this is a general effect that would also be observed on the high-resolution images, if larger volumes were available. Although the cross-sectional area increases 4-13 times, the shift to larger pores is

relatively small. This should indicate that the edge effects do not have a major influence even in the smallest analysed volumes.

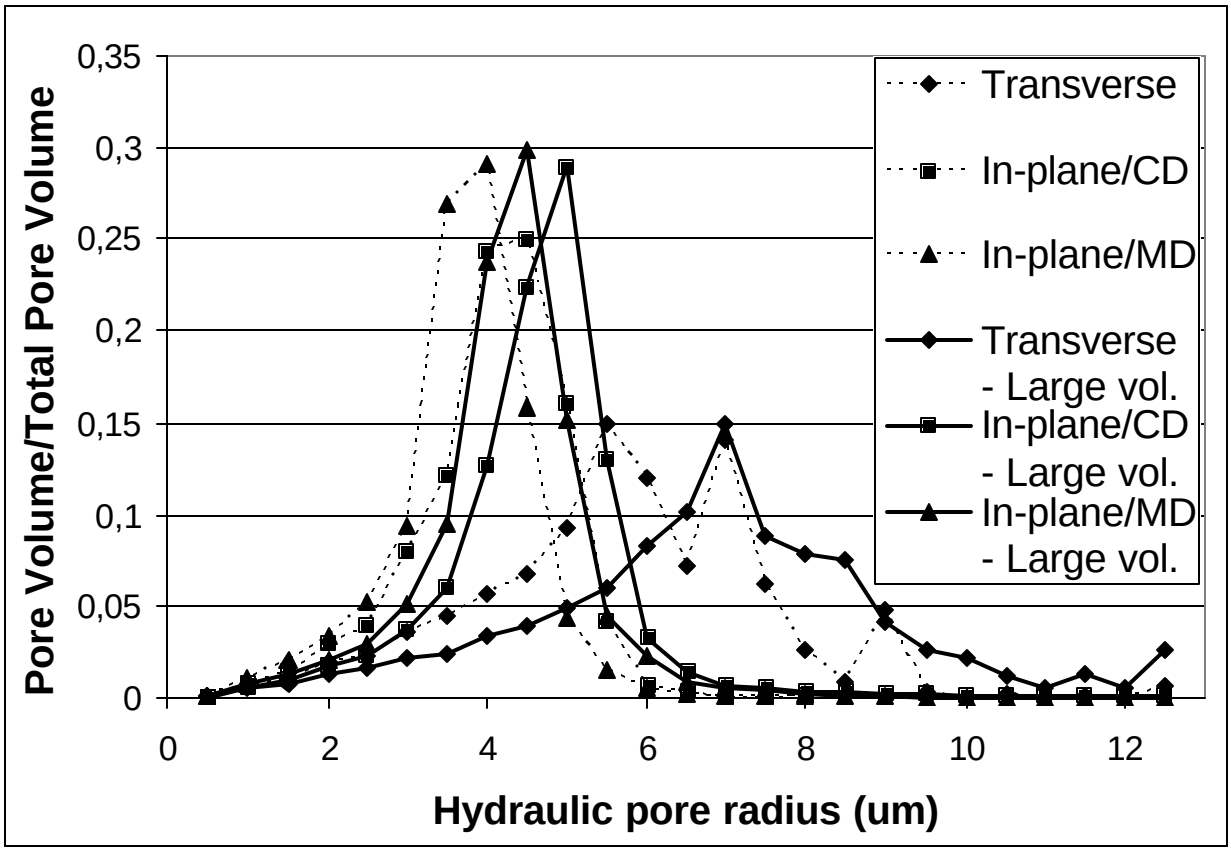

Figure 37: Hydraulic pore radii distribution for low-resolution hand sheet samples. The thicker lines show the distribution in the principal directions for the large volume.

Surface Structure Characterization of Porous Materials Using X-ray Micro Computed Tomography

Surface structure characteristics of porous materials such as paper and board play an important role in surface related applications, i.e. writing, printing, coating etc. The difference in surface structure between the top and bottom sides of the porous material, i.e. "two-sidedness" due to processing and raw material characteristics may lead to differences in end-use performance. Non-contact methods such as laser profilometry have been used to measure some aspects of the surface topography in an attempt to characterize the surface structure. Here we present methods to characterize the surface structure of porous materials using X-ray micro computed tomography and image analysis.
One of the complex problems involved in surface structure characterization of porous materials is the actual identification of the "surface". Edge detection algorithm using "jumps" in pixel intensity is used to identify the "surface" of the sample image. In tomography images, edges characterize sample boundaries and are therefore useful for identification of the "surface". The input image is

smoothed with a Gaussian kernel and edges are located by searching for zero-crossings of the Laplacian of this smoothed image.
For surface structure characterization, relevant parameters may include flatness, relative inclination of surfaces, porosity, roughness, frictional properties etc. In our study, surface volume distribution, contact fraction and surface pit distribution are used to characterize the surface structure. Since the method involves detecting the edges or boundaries on either side of the image, this also leads to estimation of thickness distribution or non-uniformity of thickness throughout the sample. Surface volume distribution measures the non-uniformity of sample surface height. Contact fraction can be regarded as 2D porosity at the surface. Surface Pit Distribution measures the non-uniformity of the width between two peaks on a specified surface level. Surface structure analysis on both surfaces of a sample leads to quantitative estimation of "two-sidedness". Here we report surface structure characteristics, two-sidedness and thickness distribution of varying paper samples. The methods reported here are suitable for low and high resolution X-ray tomography images.
As paper is a macroscopically homogeneous surface, the characterization is not always straightforward under the microscope. The real 3-D surface structure of porous materials is shown in Fig-38.

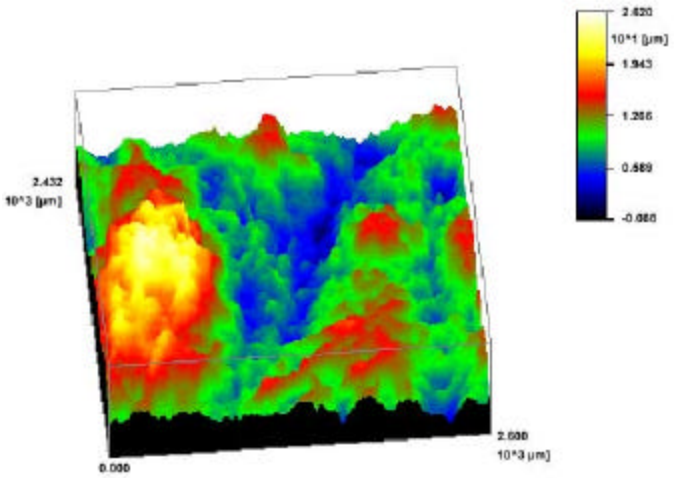

Fig-38. 3-D surface structure of porous materials

For surface structure characterization, relevant parameters may include flatness, relative inclination of surfaces, porosity, roughness, frictional properties etc. In our study, surface volume distribution, contact fraction and surface pit distribution are used to characterize the surface structure. Since our method involves detecting the edges or boundaries on either side of the image, this also leads to estimation of thickness distribution.

In the following sections, we present a method based on edge detection algorithm to characterize the surface structure of porous materials using X-ray micro computed tomography. We describe several measurements for measuring the surface roughness and provide an example of those measurements on a bleached kraft paper sample made on a pilot paper machine (denoted as BKP).

A paper sample in X-ray micro computed tomography image is shown in Fig. 39. Details on the X-ray computed tomography and the image collection method is described elsewhere (Goel, 2001, Goel, 2000, Ramaswamy, 2001). We apply the edge detection algorithm to find the surface of paper sample in the image. Edges are places in the image with strong intensity contrast, or a jump in pixel intensity. In tomography images, edges characterize sample boundaries and are therefore useful for identification of the "surface". On an "ideal" image, edges could be detected simply by identifying color discontinuities. On the "real world" image, the edges are typically not very abrupt and high frequency noise can occur in the image due to the image visualization and conversion process. It is more appropriate to think of edge detection in terms of smooth surface fitting and analyzing rapid changes of the first derivatives or zeros of the second derivative of the pixel intensities, i.e., Fig. 40. These types of techniques were developed originally by Marr and Hildreth (Marr et al., 1990) and by Canny (Canny, 1987).

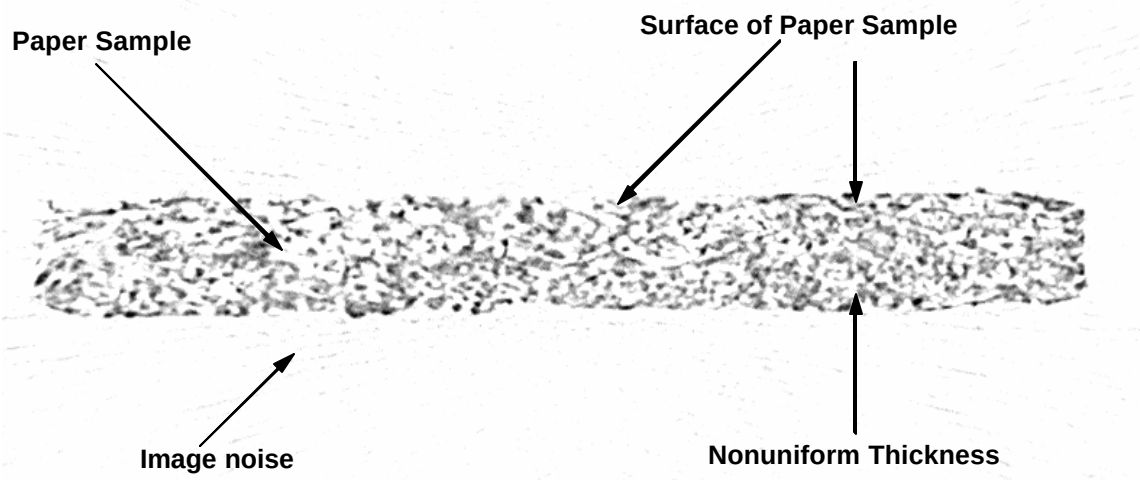

Fig-39. Tomography Image (low resolution ~3-4 micron) of Paper Sample (side-view)

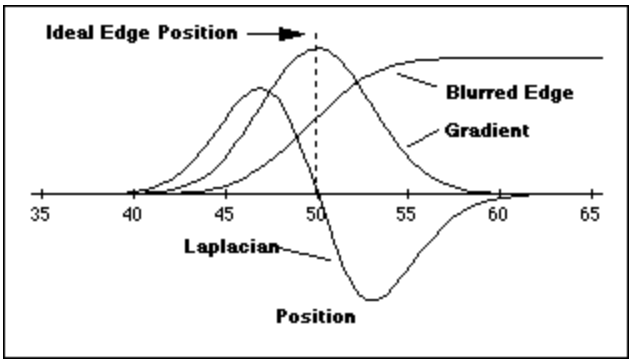

Fig-40. Edge detection based on the zero crossing of the Laplacian as determined by the second derivative

Various steps in the surface detection algorithm is given as follows: 1) the input image is smoothed with a Gaussian Kernel of some fixed width s ; 2) compute the second directional derivative, or the Laplacian; 3) identify zero crossings generated in the Laplacian of an image; 4) accept or reject the resulting edges based on signal-to-noise evaluation technique.
A Gaussian Kernel is a smoothing filter that provides the least amount of spatial blurring for any desired amount of random noise reduction. The filter operates with a convolution kernel that is a Gaussian function, which is defined in the following equation. The parameter s in the equation denotes the sigma value or standard deviation of the Gaussian functions. When used for generating a convolution kernel for a Gaussian filter, the sigma value enables the user to make fine adjustments to the amount of spatial averaging that occurs in the image.

$$g(x, y) = \frac{1}{s\sqrt{2p}} e^{-(x^2+y^2)/2s^2}$$

Eq. 5

The Laplace operator is a very popular operator approximating the second derivative which gives the gradient magnitude only. In digital images the Laplacian is often approximated by a convolution sum. In our work, the Laplacian of the sample image can be obtained by convolving the image with one of the following three convolution masks (all three have very similar result):

$$\begin{bmatrix} -1 & 3 & -1 \\ 3 & -8 & 3 \\ -1 & 3 & -1 \end{bmatrix} \qquad \frac{1}{3}\begin{bmatrix} 1 & 3 & 1 \\ 1 & -8 & 1 \\ 1 & 3 & 1 \end{bmatrix} \qquad \frac{1}{3}\begin{bmatrix} 2 & -1 & 2 \\ -1 & -4 & -1 \\ 2 & -1 & 2 \end{bmatrix}$$

Once we find the position of zero-crossings of the Laplacian, it may not be the real boundary of the sample because of the image noise in the adjacent area. In order to identify the real boundary we use signal-to-noise evaluation technique by comparing the zero-crossings of the Laplacian with adjacent pixel Laplcians. In our work, we check the next 10 pixels (~ 20 microns) after the position of zero-crossings of the Laplacian to make sure the edge we detect is indeed the real boundary of the sample otherwise we reject it. Visual inspection of the detected edge of the sample with actual images proved quite accurate.

There are a number of different ways in which the surface roughness can be defined in relation to a reference plane pressed against the surface (Bristow et al., 1986). In this work, surface volume distribution, contact fraction and surface pit distribution are applied as the measurements of the surface properties, as in Fig. 41. Since our method involves detecting the edges or boundaries on either side of the image, this also leads to estimation of thickness distribution.

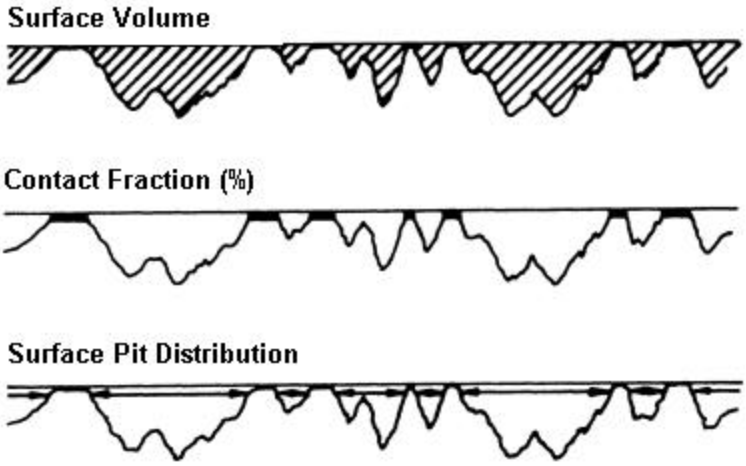

Fig-41. Methods for measuring the surface roughness

Thickness distribution measures the non-uniformity of sample thickness. Surface volume distribution measures the non-uniformity of sample surface height. Contact fraction can be thought of as 2-D porosity. Surface pit distribution measures the non-uniformity of the width between two peaks on a specified surface level. An example of those measurements on a bleached kraft paper sample (pilot machine made sample denoted as BKP) is shown in Fig. 42~45.

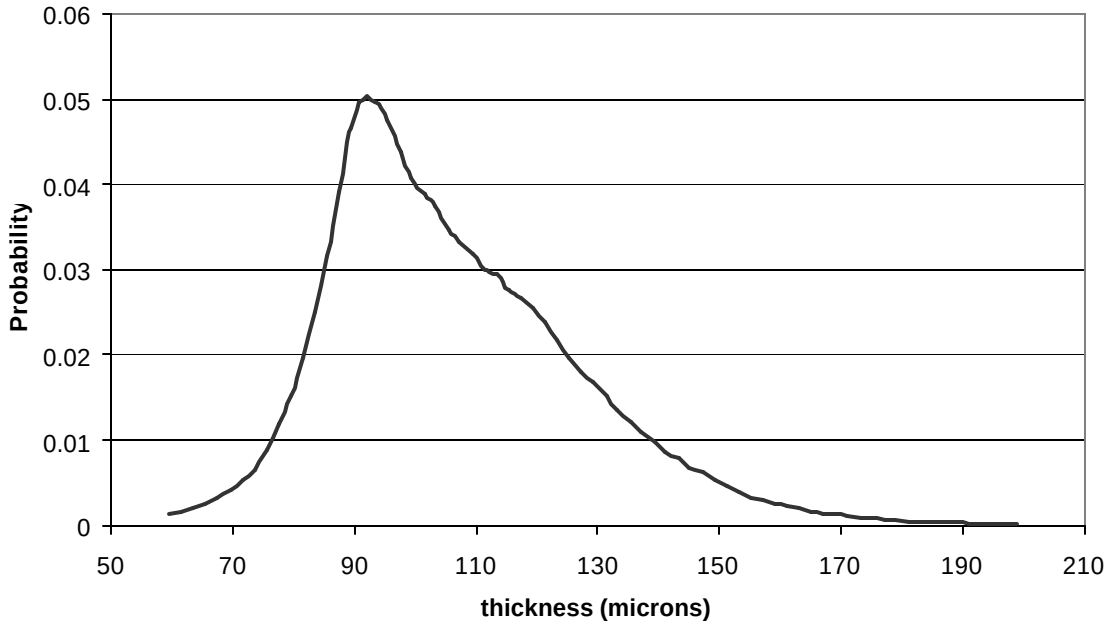

Fig-42. Thickness Distribution of BKP sample

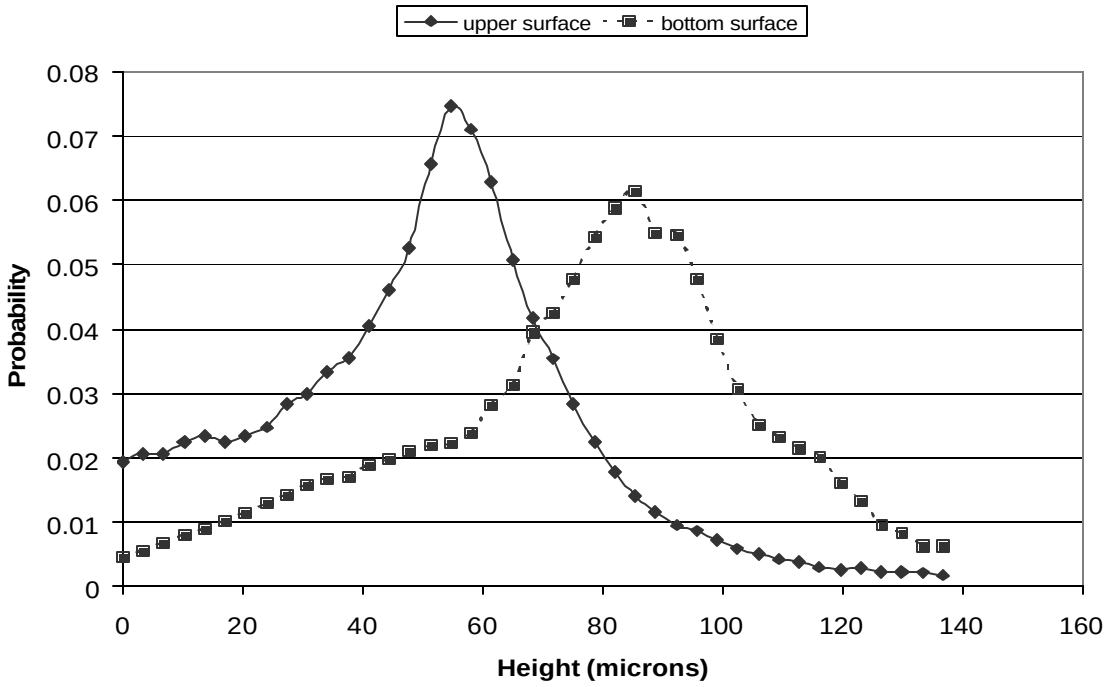

Fig-43. Surface Volume Distribution on the top and bottom sides of BKP sample

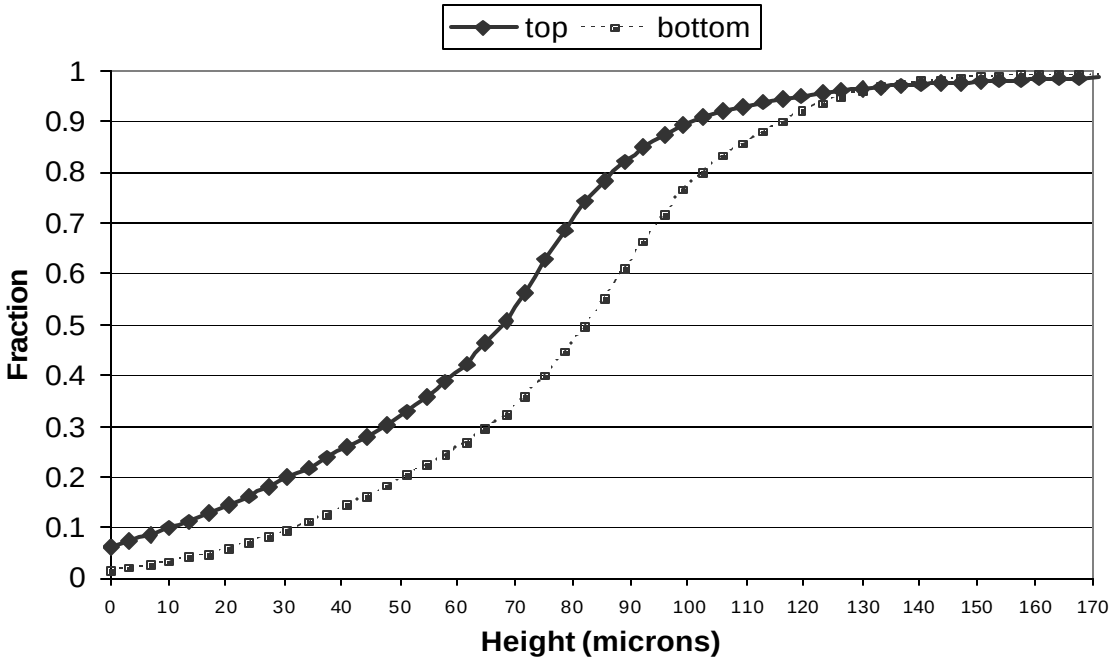

Fig-44. Contact Fraction distribution for the top and bottom side of BKP sample

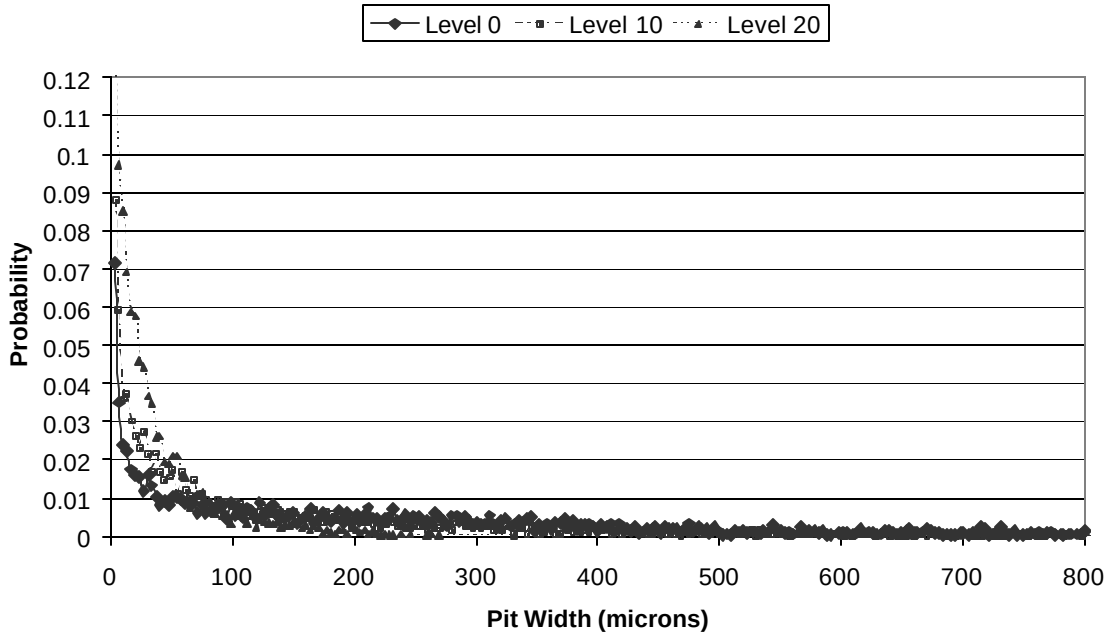

Fig-45. Surface Pit Distribution for the top side of BKP sample

As shown in Figure 42, a narrow thickness distribution with a smaller deviation will represent a more uniform thickness distribution throughout the sample. Dimensions of the sample used in this analysis are 1600 x 200 x 1000 microns. The pilot machine made paper sample used here does show reasonable thickness variation with a range of approximately 60-200 microns and a mean of ~95 microns. Surface volume distributions represented as height distributions from a fixed plane for the top and bottom sides of the sample sheet are different showing the difference between the two sides (Figure 43). The resolution and pixel size of the image (~3-4 microns and 2 microns respectively here) will also play a critical role in identifying the differences.

Contact fraction distribution for a perfectly smooth surface will be a vertical line at the origin. As shown in Figure 44, the cumulative distribution of the contact fraction indicates a relatively smoother surface for the top side compared to the bottom side. The reference height or plane for each surface is taken as the first non-zero contact point. Compared to the surface height or volume distribution surface pit distribution show a much larger magnitude indicating wider but shallow surface pits.

The surface structure characteristics determination methodology described here complements our earlier method to analyze the bulk structure and Z-D structure of porous materials. The measurements of surface structure characteristics include thickness distribution, surface volume distribution, contact fraction distribution and surface pit distribution. Method developed here even though shown for low resolution X-ray tomography images are equally applicable for high resolution (~1 micron) images. As one would expect, the surface structure characteristics will be critically dependent on the quality and resolution of the images. This presents a useful tool to characterize and engineer the surface structure of porous materials such as paper and board tailored to specific end-use applications. This will also help troubleshoot problems related to manufacturing and end-use applications.
Our future work will focus on evaluating the effect of process parameters and fiber raw materials on surface structure characteristics using high and low resolution images as well as predicting paper properties and end-use performance during industrial applications.

Method to predict transport properties using actual 3D structures of paper and board

Paper and paper board are complex three dimensional bi-continuum of interconnected pores and cellulose fibers. Transport properties such as vapor diffusivity, liquid permeability and thermal conductivity etc. in porous media are inherently related to the resistance offered by the three-dimensional structure. Brownian motion random walk simulation in actual 3D structures of paper and board obtained by X-ray micro tomography are reported to evaluate transport properties of paper and board. The an-isotropic transport properties predicted by the simulation for varying paper structures agree closely with experimental data

Presently, there is no general analytical model that can accurately predict the transport properties of fibrous composite structures such as paper and board. Simple models such as Stokes-Einstein equation and Maxwell relation can be used to describe diffusion coefficients of solutes diffusing through a continuum. Cussler *et al.* (Cussler, 1988) have derived analytical expression showing the

relationship between (normal/effective diffusivity) and the aspect ratio of the particles and the porosity of the medium for simple particle orientations. For heterogeneous composite media with complex three dimensional structures such as paper and board a more suitable approach for predicting effective diffusivities is to use Monte Carlo simulations of molecular trajectories based on Brownian motion. Following this approach, Eitzman *et al.* (Eitzman et al., 1996) have used a hybrid technique to predict diffusivities of flake filled membranes using artificially generated two-dimensional structures. Hellen et al. (Hellen et al., 2002) have used random walk simulation and first passage time distribution principles to calculate the flux and the effective diffusion coefficient in model fiber networks. The above simulations in one and two dimensions, however, failed to take into account the heterogeneous, complex three-dimensional structures of composite fibrous medium.

Transport properties such as vapor diffusivity, liquid permeability and thermal conductivity etc. in paper are inherently dependent on the resistance offered by its complex three dimensional structure. Because of its heterogeneous and complex fibrous structure, no general analytical model could be applied accurately to predict its transport properties. Stokes-Einstein equation and Maxwell relation can be used to describe diffusion coefficients of solutes diffusing through a continuum of periodically arranged spheres but at very high porosities.

The diffusivity in a porous medium such as paper, where the pores are permeable and fibers are almost impermeable at very low relative humidities, is a quantity that takes into account the porosity of the medium and the tortuous paths that the diffusing molecules have to take through the complex geometry of the paper and board. There are various examples which involve diffusion during papermaking and its end use application. The water vapor diffusion in commercial papermaking processes is the main mass and heat transfer mechanism during drying of the wet paper web. Therefore a better understanding of the diffusion phenomena by which water moves through paper could lead to significant improvements in pressing, coating, drying, finished product quality, printing and energy efficiency of the process.

Cussler *et al.* [Cussler, 1988] have derived analytical expression showing the relationship between the ratio of normal to effective diffusivity and the aspect ratio of the particles and the porosity of the medium for simple particle orientations in flake filled membranes. For heterogeneous composite media with complex three dimensional structures such as paper and board a more suitable approach for predicting effective diffusivities is to use Monte Carlo simulations of molecular trajectories based on Brownian motion. Following this approach, Eitzman et al. [Eitzman et al., 1996] have used the hybrid technique to predict diffusivities of flake filled membranes using artificially generated two-dimensional structures. They found that diffusion of carbon dioxide through silicone–polycarbonate membranes containing oriented flakes is proportional to the square of the volume fraction of the flakes, to the square of the aspect ratio, and to the square of the cosines of the angle of the orientation of the flakes. Their results were consistent with Monte Carlo simulations.

Cussler et al [Cussler, 1988] using Monte Carlo method in similar flake filled membrane systems found that diffusion depends on tortuous paths around the flakes, slits between flakes, and on constricted transport from entering these slits. Their calculation showed that a simple analytical equation by Aris [Aris, 1986] predicts these three effects.

Any of various physical phenomena in which some quantity is constantly undergoing small and random fluctuations can be treated as Brownian motion. It was named after Scottish botanist Robert Brown, the first to study such fluctuations in 1827. Diffusion is a physical process in which a substance tends to spread from regions of high concentration to regions of lower concentration. Thus, diffusion is a macroscopic manifestation of Brownian motion on the microscopic level. It is thus possible to study diffusion by simulating the motion of a molecule and computing its average behavior. A few examples of the countless diffusion processes can be explained in terms of Brownian motion include the diffusion of water vapor in paper, diffusion of pollutants through the atmosphere, and the diffusion of calcium through bone tissue in living organisms.
As shown by Einstein, motion of such molecules in one dimension collectively obeys the following equation (Einstein, 1926)

$$\frac{\partial f}{\partial t} = D\frac{\partial^2 f}{\partial x^2} \qquad (6)$$

Where, D is the diffusion coefficient and f(x, t) is the number density function. The solution of above equation for the initial condition of a point source at time zero diffusing outward is given by

$$f(x,t) = \frac{n}{\sqrt{4\pi Dt}}\exp\left(-\frac{x^2}{4Dt}\right) \qquad (7)$$

Where,

$$n = \int_{-\infty}^{\infty} f(x,t)dx \qquad (8)$$

Equation (7) describes the instantaneous particle distribution function. The mean square displacement of any particle at a given time t can then be determined by using equation (8).

$$< x^2 > = \frac{\int_{-\infty}^{\infty} x^2 f(x,t)dx}{\int_{-\infty}^{\infty} f(x,t)dx} = 2Dt$$

(9)

Equation (9) shows that mean square displacement is linearly proportional to time. This is the central premise of all diffusion like processes including conduction of heat and electricity. Equation (9) applies to motion in one dimension. Nonetheless, for isotropic medium, the motions in each dimension are independent of one another then mean square displacement in three dimensions is given by:

$$< S^2 > = < x^2 > + < y^2 > + < z^2 > = 6Dt \qquad (10)$$

From equation (9)

$$< x^2 > = 2Dt$$

Above equation is applicable only when diffusion can occur everywhere, but paper is a two-phase heterogeneous medium consisting of cellulose fibers and voids. Hence, above equation cannot be applied directly for such systems. At low humidities if we assume pore is the only conducting phase and fibers are non-conductive then the volume fraction where diffusion can occur will be same as porosity (e) of sample, hence equation (9) can be modified as

$$\varepsilon < x^2 > = 2Dt \qquad (11)$$

From the kinetic theory of gases, free space diffusion coefficient is given by

$$D_o = \frac{1}{3}\bar{\lambda}\bar{v} \qquad (12)$$

Where,

$\bar{\lambda}$: mean free path of the molecules

$\bar{v}$: mean molecular velocity and

Combining equations (11) and (12) yields

$$\frac{D}{D_o} = \frac{3}{2}\frac{e}{\bar{l}}\frac{< x^2 >}{\bar{v}t} \qquad (13)$$

Where $\bar{v}t$ is the average distance traveled by the particle in time 't' and $< x^2 >$ is the ensemble average displacement in 'x' direction.

Method

Hand sheets of 300 gsm were prepared in our laboratory by refining bleached softwood kraft pulp to different levels so as to obtain different structures. Refining increases inter-fiber bonding and makes fibers flexible enough to conform well around each other, thus leading to denser sheet and lower porosity. Basically refining is a mechanical treatment of fibers to develop optimum papermaking properties. These samples ranging in freeness from 220 to 670 ml CSF (Canadian Standard Freeness Tester) were then visualized using X-ray micro tomography and characterized using image analysis.
The sample of freeness 330 has been removed from our analysis due to its abnormal behavior during experiments as well as simulation.

Following table shows some of the main structural characteristics of our paper samples (hand sheets) which were helpful in our analysis:

Table 1. Properties of hand sheets (paper samples) investigated [Goel, 2003]

CSF	Porosity	Dimension (μm^3)	SSA* (m^2/g)	Geometric Tortuosity *Inplane*	*Transverse*
670	0.43	752x752x160	0.189	2.037	1.572
570	0.36	880x880x160	0.148	3.191	1.962
460	0.31	880x880x160	0.134	3.316	2.163
280	0.26	752x752x200	0.112	3.916	2.599
220	0.25	920x920x200	0.103	5.337	2.289

* Specific Surface Area

Brownian motion random walk simulation in actual 3D structures of paper and board obtained by X-ray micro tomography were to estimate their pore diffusivity characteristics. A sequence of microtomographs was imaged at approximately 2µm intervals and the three-dimensional pore-fiber structure reconstructed. The figure shown below shows the trajectory of a molecule inside our paper sample. For ease of visualization in Figure 46, fibers have been removed from the volume but kept during the actual simulation. Zigzag random motion of the molecule following each and every step of the way is referred here as 'true random walk' (TRW).

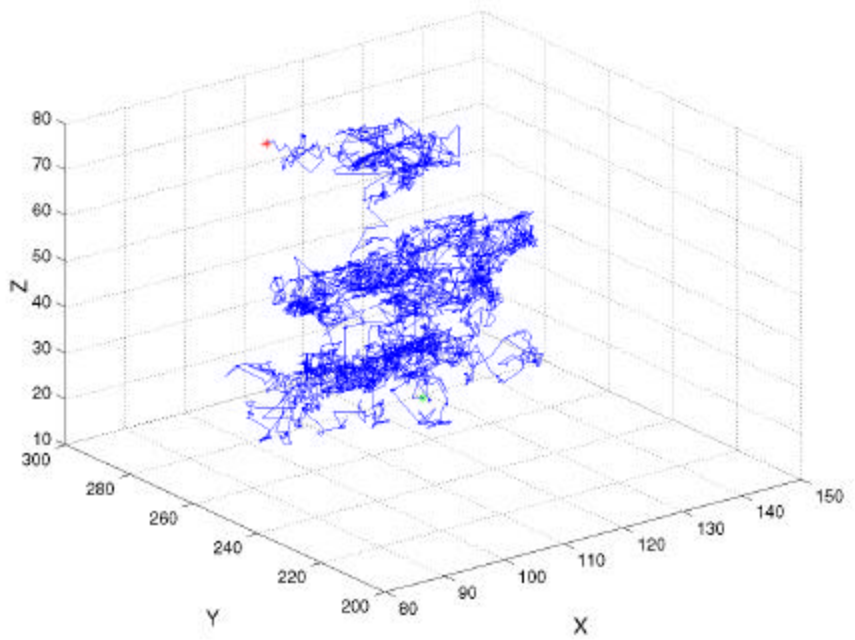

Figure 46: Zigzag path traversed by a molecule inside paper sample [Goel, 2003]

The simulation developed in this work relies on some idealizations and assumptions. First noteworthy assumption is that fibers have been treated as impermeable objects, which is only true at very low humidities. The case for permeable fibers will be treated later. As molecules are moving inside the pores and the size of most of the pores is significantly greater (Cussler, 1997) than the mean free path of molecules, so the assumption of neglecting Knudsen diffusion is justified (ratio of mean pore size to $\overline{\lambda} > 20$).

First Passage Time (FPT) Method

During diffusion in paper or other porous materials where mean free path is much smaller than the pore size, a large amount of computational time would be required to investigate the whole structure. Hence, to gear up the computation, first passage time has been adopted, which while decreasing the computational time does not alter the actual process. Zheng and Chiew (Zheng et al., 1989) have shown that First Passage Time (FPT) principle is derived from the solution of point source diffusion equation. They were the first to implement this technique successfully. FPT method as illustrated in Figure 47is followed when the molecules are within the pore surface. When they are closer to the fiber surface true random walk is followed. To accommodate this, an imaginary boundary layer of thickness five times the mean free path is drawn outside every fiber. When molecule is within this boundary layer, it will advance using true random walk. Outside the boundary layer, distance to nearest fiber interface will be calculated and an imaginary sphere of the radius of this distance will be constructed as shown in above figure and molecule will jump from the center of this sphere to its surface. The direction will be decided by 'hyper cube rejection method' (http://astronomy.swin.edu.au/~pbourke/geometry/spherepoints). The method ensures that the direction of jump of molecule is completely random. The time invested by a molecule from center of the sphere to its surface, if it were following a random walk, is approximated as $R^2/6Do$ (Siegel et.al., 1986, Zheng et al., 1989, Eitzman, 1992), where 'R' is the radius of sphere and 'Do' is free space diffusion coefficient. This relation is valid only if the trajectory is at least five times the mean free path, and is not valid otherwise.

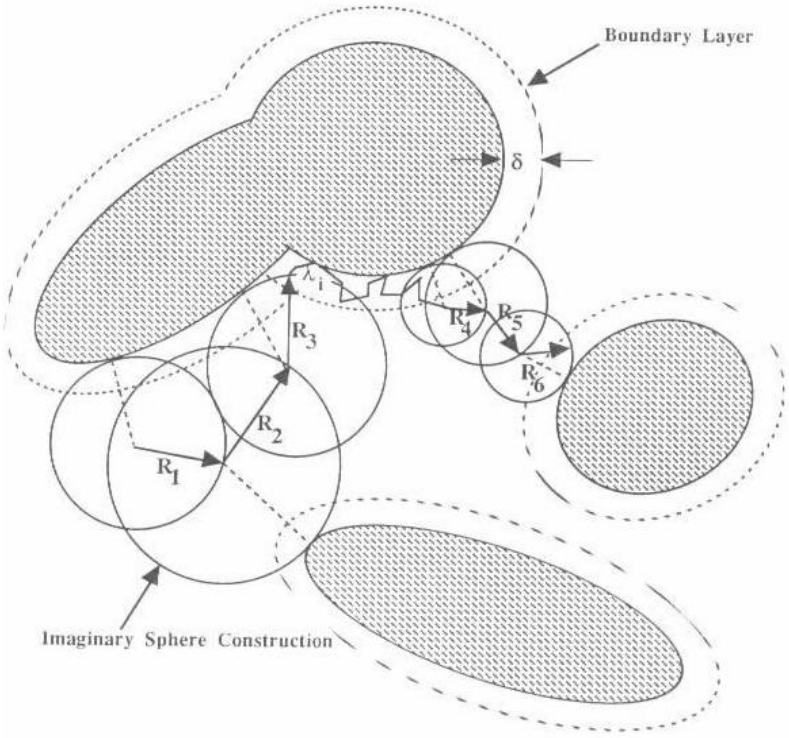

Figure 47 Illustration of First Passage Time Method (Melkote, 1990)

Description of Simulation Procedure

As our method involves the displacement covered by molecule in any direction, if the dimension of sample in any direction is less than other directions then molecule will have less displacement in that direction. In paper samples Z-dimension i.e. thickness was much less than X and Y dimension (Table 1). Therefore, molecules will travel less displacement through Z direction in comparison to X and Y directions.

To overcome this dimensional restriction, previous method developed by Goel [Goel, 2003] has been modified by randomly picking cubes inside the sample and allowing molecules to probe the structure inside these cubes. Length of each side of the cube has been taken equal to the thickness of each sample as this was the largest Z-direction dimension. Due to non-uniform and heterogeneous structure of our paper samples, smaller cubes chosen inside sample showed significant variation in porosity and hence in tortuosity and diffusivity. Taking into account this inherent variation, many cubes were picked inside each sample until values of diffusion coefficient converged. The number of cubes for our sample was typically 100. The average value was then reported as “pore diffusivity” of sample by taking arithmetic average of all the values obtained from several cubes.

The code runs one by one in each cube i.e. the algorithm is same for all the cubes. First of all, our method, which is an improved version of Goel's code [Goel, 2003], reads and binarizes all the tomographic images. Threshold for our sample came out to be 1. So the voxels having intensity below it were assigned zero intensity i.e. black (pore) and above it 255 i.e. white (fiber). Once this binarization is done, random walk simulation for each molecule is run one by one in randomly picked cubes inside the paper samples. We chose 1000 molecules or tracers for our simulation again to obtain convergence. Earlier work by Goel [Goel, 2003] showed convergence can be obtained for number of molecules greater than or equal to 1000. Hence, we have 1000 molecules in 100 random cubes i.e. a total of 100, 000 molecules or random walkers for each sample.

The start for each molecule trajectories is a randomly picked point inside a cube that is three fourth of whole volume in size so that molecule or tracer will have same probability to escape in any direction. If the starting location falls inside a pore pixel, it is kept as an initial starting point; if it falls inside a fiber, it is discarded but used to calculate porosity of the cube in case of periodic spheres. In paper samples porosity was directly found by calculating the fraction of void pixels. The reason for discarding point inside fiber is that fibers have been treated as impermeable. The distance from this starting point to the surface of the nearest fiber pixel is then calculated. If the distance is more than or equal to five times mean free path, the tracer follows 'first passage time' as discussed above, otherwise it advances with its free path taken from following exponential distribution [Loeb, 1934],

$$f(l) = \frac{1}{\bar{l}} e^{-l/\bar{l}} \qquad (14)$$

l is calculated by,

$$l = -\bar{l} \ln(1-x) \qquad (15)$$

In above equation, $x \in [0,1)$, is a random number uniformly distributed between zero and one. For our simulation, x calculated each time with the use of function srand48( ) in programming language C, which generates uniformly distributed numbers between 0 and 1. $\bar{l}$ is mean free path of molecules, calculated as follows [Cussler, 1997]:

$$\bar{l} = \frac{K_B T}{\sqrt{2}\, p\, p\, s_{12}^2} \qquad (16)$$

Where,
T : temperature in ^oK
K_B : Boltzmann Constant
p : Pressure in atmosphere
s_{11} : collision diameter in angstroms

At T = 298 and p = 1 atm:
$K_B = 1.3806*10^{-23}$ J.K^{-1}
$s_{11} = 2.551$ A^o
Substituting the above values in equation 16 we get,
$\bar{l} \sim 0.14$ µm

The simulation method used here is valid for any diffusing species as long as corresponding values of $\overline{l}$ and Do are used. Since kinetic theory is used to calculate normal diffusivity, molecular diffusion of simple systems such as He-He was used in the simulation. Since the end result is reported as normalized diffusivity ratio, i.e. D/Do this can then be used to predict diffusion coefficient of other species in porous media.

When a molecule trajectory hits pore-fiber interface, that point of intersection has been found and molecule is reflected back to its original position in pore and then the same procedure reported earlier i.e. FPT and true random walk, is repeated again as discussed above until tracer escapes from the sample. If the molecule does not escape from the sample after traveling a total distance of greater than 1m (10^6 μm) then it is treated as trapped in dead pore and not considered for diffusivity calculations. In order to estimate pore diffusivity in each of the three orthogonal directions, mean-square displacement and distance covered by tracer in each direction (x, y and z) are recorded in separate files. The raw data for mean-square displacement vs. the total distance traveled for all 1000 tracers is shown in Figure 58. Then our program 'bucket_new.m' written in MATLAB, which separates the raw data into buckets of equal distance intervals and then calculates the ensemble average, is used to get the final value of pore diffusivity.

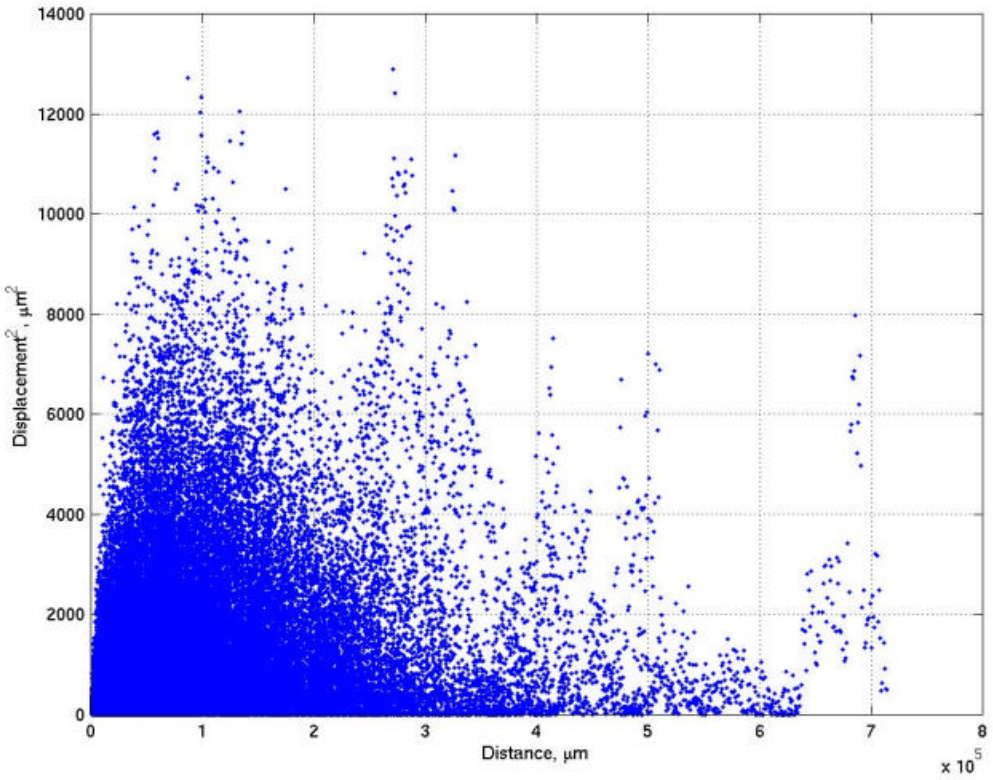

Figure 58 Displacement^2 vs. Distance for sample 460 of porosity 0.31 for inplane diffusivity

Due to the random nature of molecular motion, as one would expect, there is a whole range of displacement for each distance. In order to obtain an ensemble average as shown in Einstein's relation, we divided total distance into several equidistant buckets. For example the maximum

distance covered by all molecules is 7 x 10^5 µm and as we are recording this at every 1000 µm distance traveled, so the number of buckets will be 7 x 10^5 / 1000, which is 700. The size of buckets is 1000 µm. In order to ensure that almost all of the molecules traverse the whole structure, we chose the 95 % criteria. So, if the percentage of molecules in a given bucket is less than 95 then we will reject that bucket. This criterion reduces the total number of buckets to approximately 10-20 resulting in a very good linear correlation. The correlation coefficients are generally around 0.99 as shown in Figure 49.

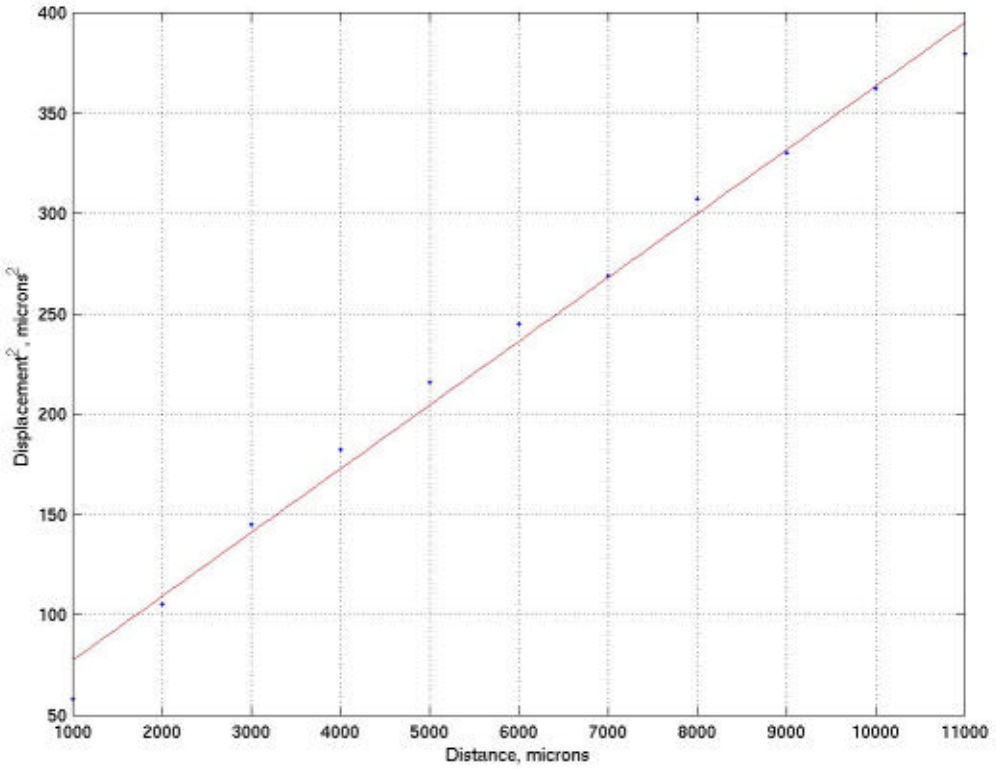

Figure 49 Linear fit for raw data shown in Figure 48

So, from above figure the slope (S) of the line is calculated, which will be used in the following formula. The pore diffusivity is then calculated as follows,

$D_{eff} = 1.5SDo/ \overline{l}$ (17)

Where,

D_{eff}: normal diffusion coefficient in pore

S : slope of plot for mean-square displacement vs. the total distance traveled

Do: free space normal diffusivity

$\overline{l}$: mean free path of the molecule

Transport Properties - Results and Discussion

Brownian motion random walk simulations were then conducted in each of the paper samples of varying structure and the results are reported below. To verify our simulation method, we studied the effect of porosity on effective diffusivity (D) for an array of periodic spheres having simple cubic cell arrangement. Porosity of the periodic structure was changed by changing sphere's radii within a given total volume. Results from random walk simulation were then compared with well know analytical expressions given in the literature [Akanni et al., 1987]. The limitation of these analytical expressions is that they are valid only at high porosities (~1). Our simulation values compare reasonably well with these analytical values. Analytical expressions reported in the literature are given as follows [Akanni et al., 1987]:

Maxwell:

$$\frac{D}{D_o} = \frac{2\varepsilon}{(3-\varepsilon)} \tag{18}$$

Wakao:

$$\frac{D}{D_o} = \frac{e^2}{\sqrt{3}} \tag{19}$$

Rayleigh:

$$\frac{D}{D_o} = \frac{2e - 0.3938(1-e)^{10/3}}{3 - e - 0.3938(1-e)^{10/3}} \tag{20}$$

The effective diffusivity values in the three orthogonal directions (X, Y and Z) viz. Dx, Dy and Dz values respectively for varying structure were the same because of symmetry of the structure. Values calculated from analytical expressions are compared with simulation values in the following table.

Table 2 Simulation and analytical values at different porosities for periodic spheres

Porosity	Sim_1	Sim_2	Maxwell	Wakao	Rayleigh
1	0.960646	0.946614	1	1	1
0.996	0.951023	0.941066	0.993846	0.992016	0.994012
0.967	0.924944	0.923025	0.950769	0.935089	0.951303
0.887	0.787582	0.791927	0.839615	0.786769	0.839544
0.732	0.604440	0.613937	0.645385	0.535824	0.644737
0.475	0.324558	0.305229	0.376238	0.225625	0.364671
0.355	0.205070	0.210936	0.268431	0.126025	0.242276

0.250	0.122861	0.125593	0.18158	0.062350	0.133988

Sim_1: Values obtained from Big Cube (total sample volume: containing the array of periodic spheres)
Sim_2: Values obtained from averaging the smaller cubes inside Big Cube (total sample volume)

In the Figure 50, diffusivity values obtained from our simulation have been compared to the analytical expressions given by Maxwell, Wakao, and Rayleigh. As it is evident from Figure 50, values obtained from our simulation are in close agreement with analytical values at different porosities. Interestingly, simulation results lie in between Rayleigh, Maxwell, and Wakao expressions for the whole porosity range.

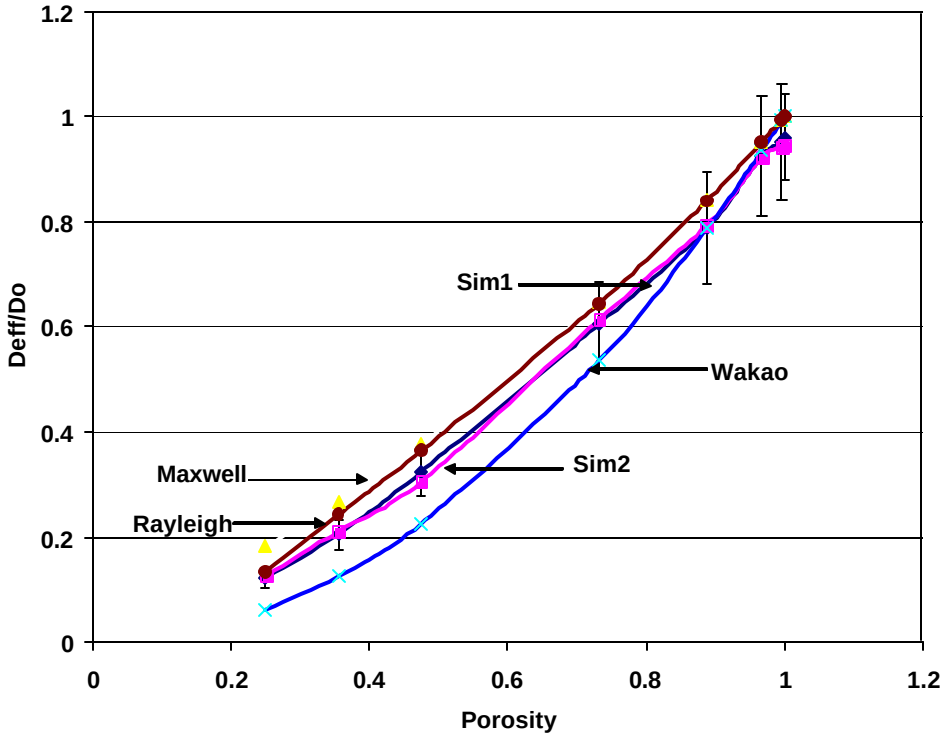

Figure 50 Comparison of diffusivities at varying porosities

We randomly picked many smaller cubes inside the big cube and then the average value of diffusivity and porosity is reported as final results. The C language function ***srand48 ( )*** which we use to create random numbers is used for this purpose. The ratio of the size of bigger cube to smaller cube was approximately 10.

It can be observed from Figure 50 that the diffusivity values are directly proportional to porosity. The reason is more open and less tortuous structure with increasing porosity. The figure also shows the variation in diffusivities ratios (95% confidence intervals) at all porosities.

As shown in Figure 51, the variation in D/Do among smaller cubes at different porosity ranges from approximately 4% to 9%. This variation can be partly explained by variation in porosity among the cubes, as shown in Fig 52.

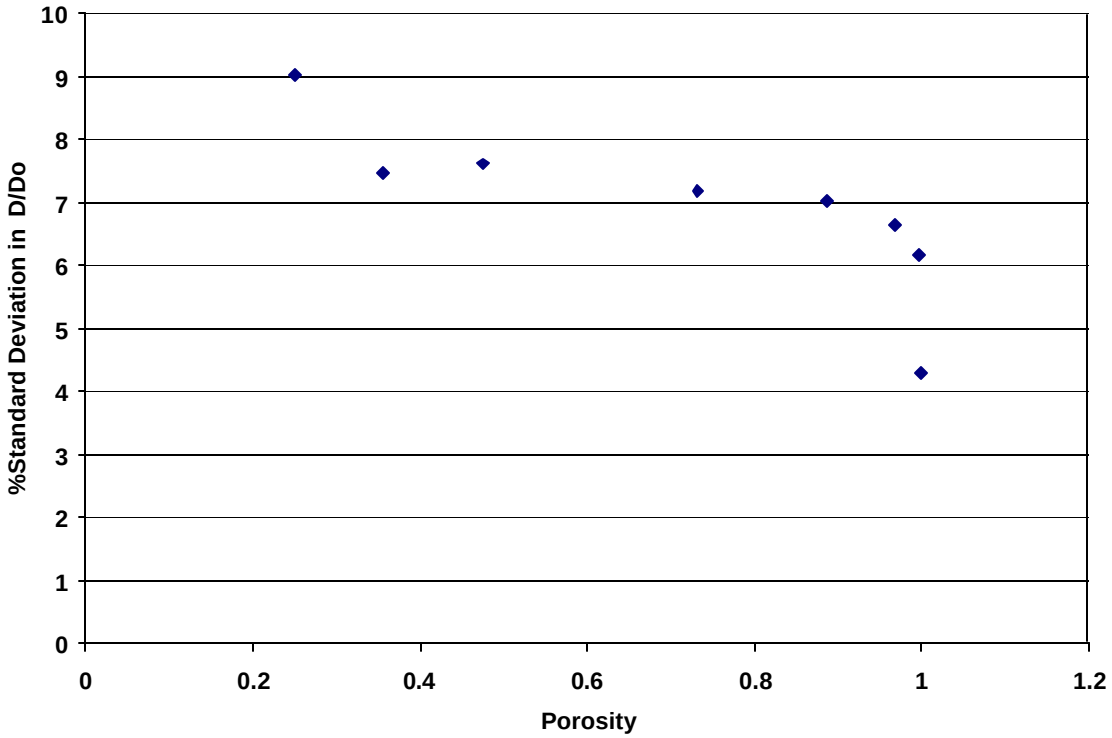

Figure 51: Percentage Standard Deviation in D/Do as a function of porosity using small cubes within the big cube

Using the definition of tortuosity (t) [Cussler, 1997]

$$\frac{D}{D_o} = \frac{e}{t} \qquad (20)$$

Values of t were estimated using D/Do and *e* obtained from simulation. It is interesting that the t increases approximately from 1 to 2 as *e* decreases from 1 to 0.

Figure 52 Porosity variations among small cubes

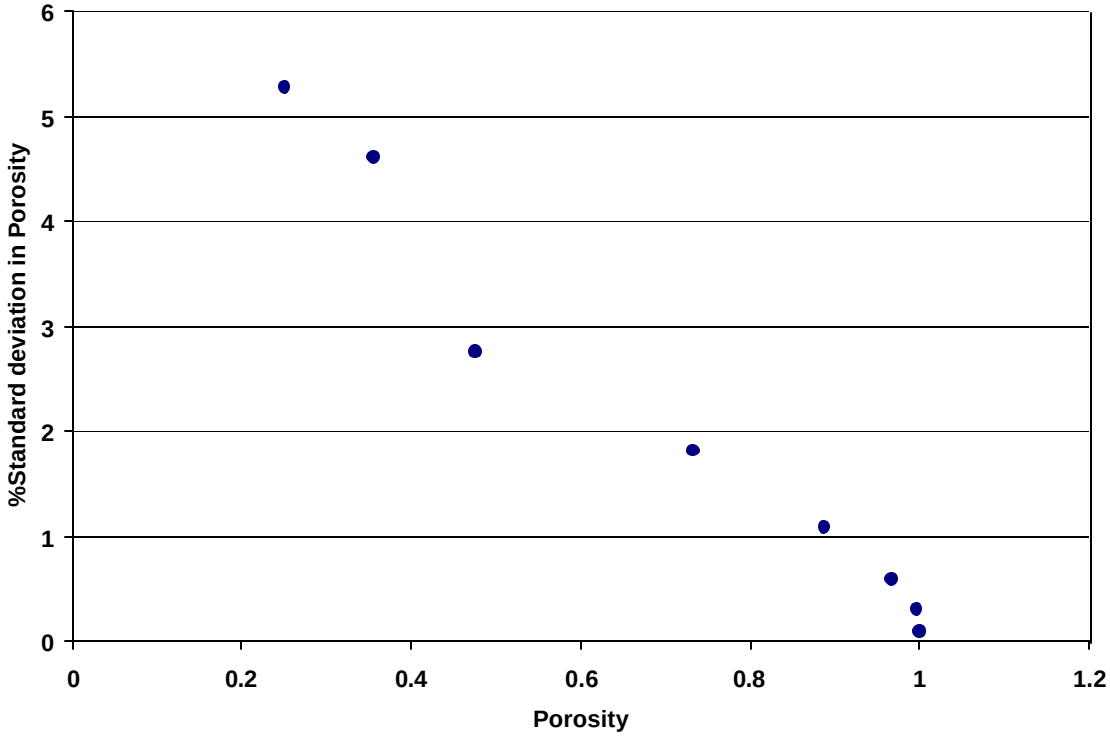

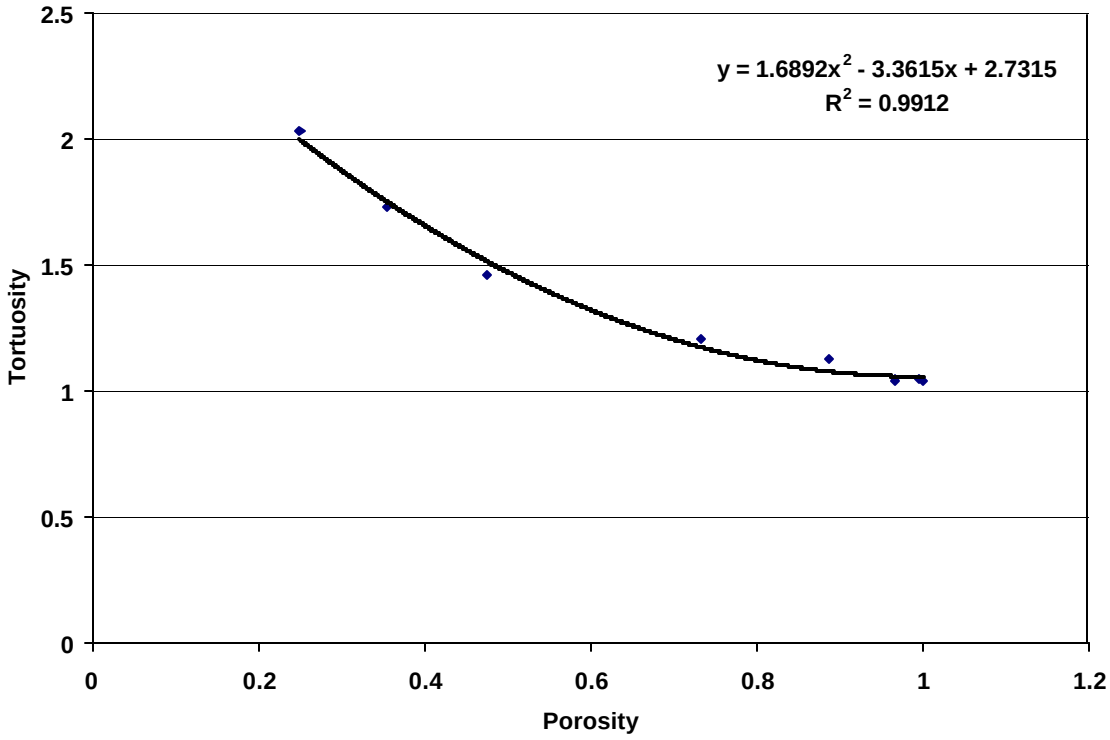

Figure 53 Tortuosity vs. porosity for periodic spheres

Summarizing results with periodic spheres, our simulation compares reasonably well with analytical expressions, interestingly lying between two of the well known relations reported in the literature (Akanni et al., 1987). Method of selecting small cubes inside bigger volume is well justified. However, it involves inherent variability in structural characteristics which needs to be considered in comparing predictions from the simulation.

After having obtained verification of our methodology with periodic spheres, now we move on to predicting effective diffusivities in actual paper structures. As described earlier, paper samples of varying structure were obtained from mechanically treating softwood kraft fibers. The 3 D internal structure of the samples were then obtained using X-ray micro computed tomography.

Using a similar approach as in periodic spheres, smaller cubes of sides equal to thickness of paper samples were randomly selected within the total volume. Random walk simulation using FPT and true random walk was then conducted in each sample and average results are reported. The effective diffusivity values were then compared with experimental data.

Experimental data used in this work for comparison to simulation results was obtained by Ramarao et al. [Massoquette, 2003a, Massoquette, 2003b] for the same paper samples of varying structures. The diffusion cup experimental set up is shown in Figure 55 [Lescanne et al., 1992, Massoquette, 2003a]. The experimental set up for in-plane diffusivities is shown in Figure 54. More details on the experimental set up, procedures and data collection and analysis can be found in Massoquete et al.[Massoquette, 2003a].

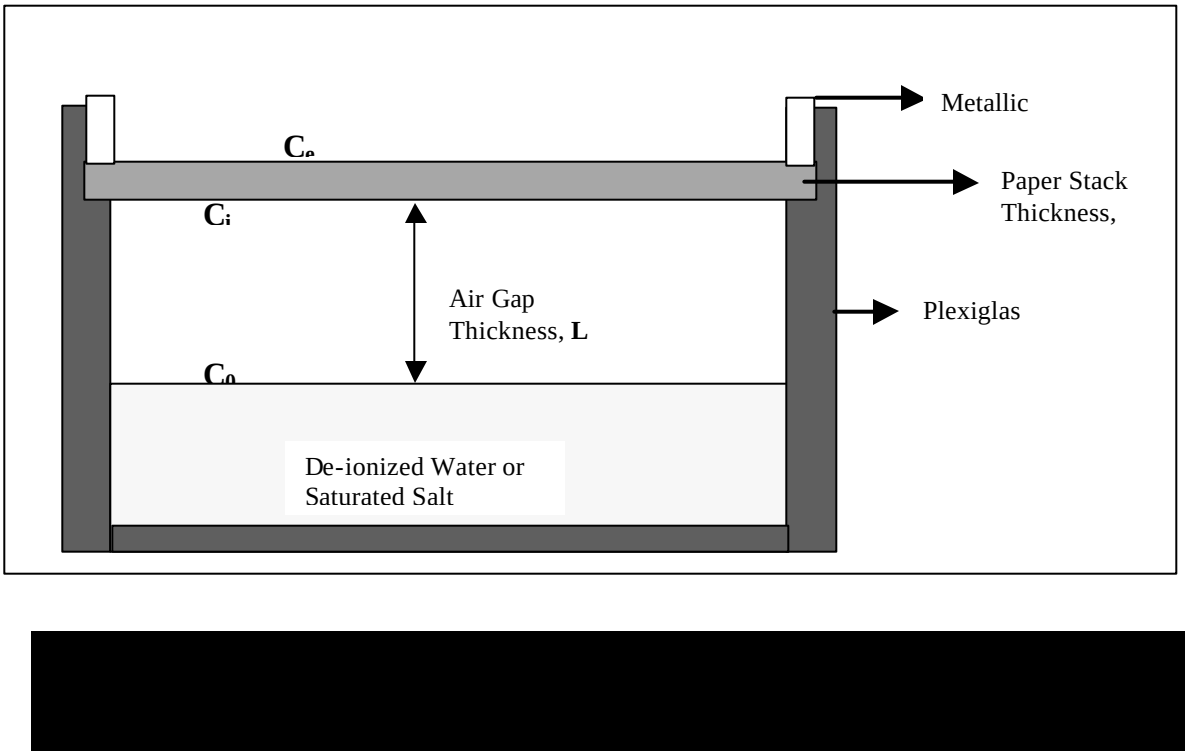

Figure 54: The diffusion cup experimental set up used by Massoquete et al. . [Massoquette et al., 2003a] for measuring diffusivity in the transverse (z) direction of paper sheets

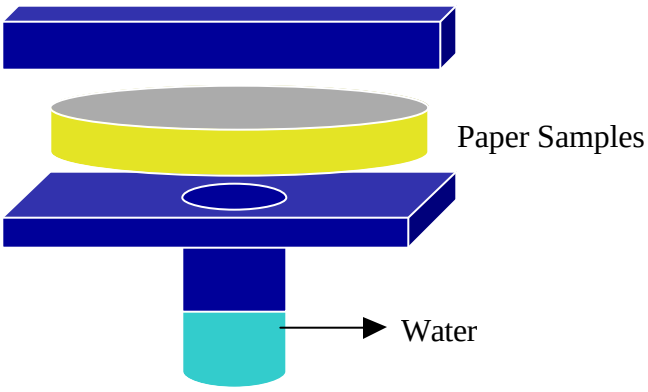

Figure 55 Experimental set used in-plane diffusion coefficient by Massoquete et al. [Massoquette et al., 2003a]

Values obtained from our simulation for in-plane and transverse diffusivity and their comparison to experimental data are tabulated below.

Table 3 Comparison of experimental and simulation In-plane Diffusivity results for paper samples of varying structure

CSF	Porosity	*Simulation* Dp/ Do	*Experiment* Deff/Do *
670	0.4300	0.2102	0.1254
570	0.3586	0.1614	0.1438
460	0.3103	0.1182	0.0596
280	0.2583	0.0970	0.0735
220	0.2457	0.07357	0.1208

Table 4 Comparison of Transverse Diffusivity results for hand sheets (paper samples)

CSF	Porosity	Simulation	Experiment	
		Dp/ Do	Dp/ Do	Deff/Do *
570	0.3586	0.0733	0.0577	0.061538
460	0.3103	0.0551	0.0232	0.034077
220	0.2457	0.0290	0.0100	0.020577

* : Experimental values taken with 30% RH as the open face boundary condition
Dp : Effective diffusion coefficient in pore, cm^2/s
Deff : Effective diffusion coefficient in whole structure, cm^2/s

As tabulated above, both experimental and simulation results indicate that in-plane diffusivities are greater than transverse diffusivities, owing to the layered structure of paper samples. In general, simulation results are in close agreement with experimental results. Nevertheless, there are differences between experimental and simulation results. There may be several reasons for that, one of the reasons could be due to differences in size of the sample i.e. experiments have been carried on the paper sample of approximately 10 cm^2, where as simulation has been performed using approximately only 1 mm^2. The second reason could be due to change in structure with RH or moisture. We are using paper structures which are imaged while being dry. However, experimental values determined at RH 30% so that may change the pore size distribution and the overall structure. Swelling of cellulose fibers in our paper samples during moisture uptake might also alter the fiber diameter. At higher RH we may have two conflicting effects. One is fiber swelling resulting in increased diffusion through fiber. The other is the overall structure. If the pore space in overall structure is only conducting phase then because of fiber swelling pore diffusion will decrease. On the other hand, if the pore space is also opened up with increased fiber swelling then this may increase pore space diffusion. Theses results are explained further using the following figures.

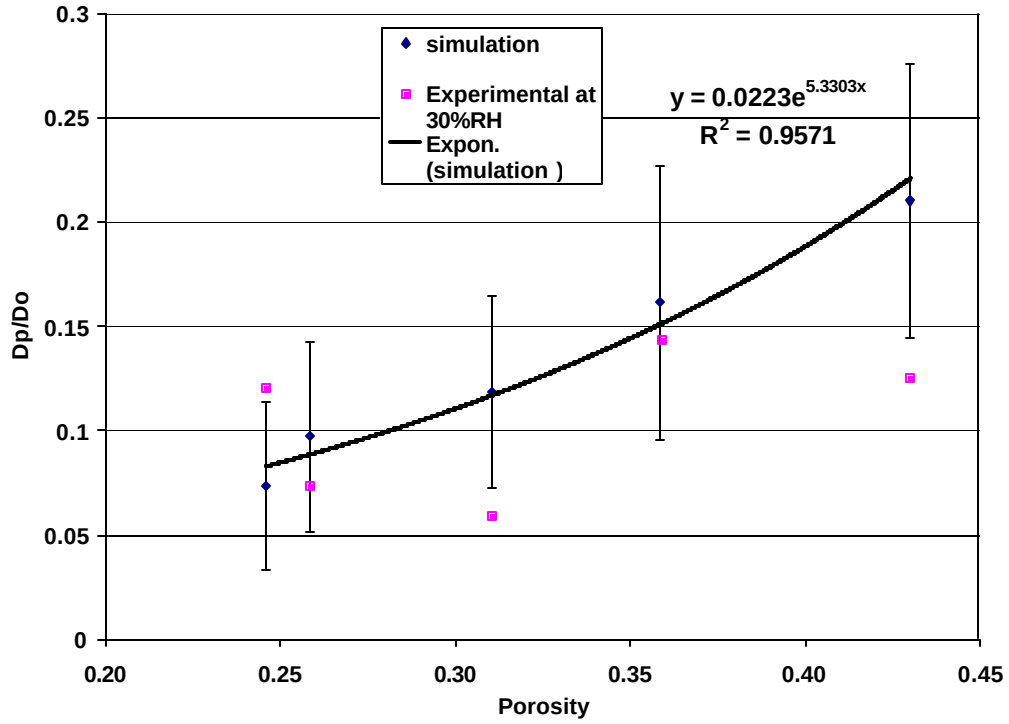

Figure 56 Comparison between simulation and experimental inplane diffusivity values for hand sheet

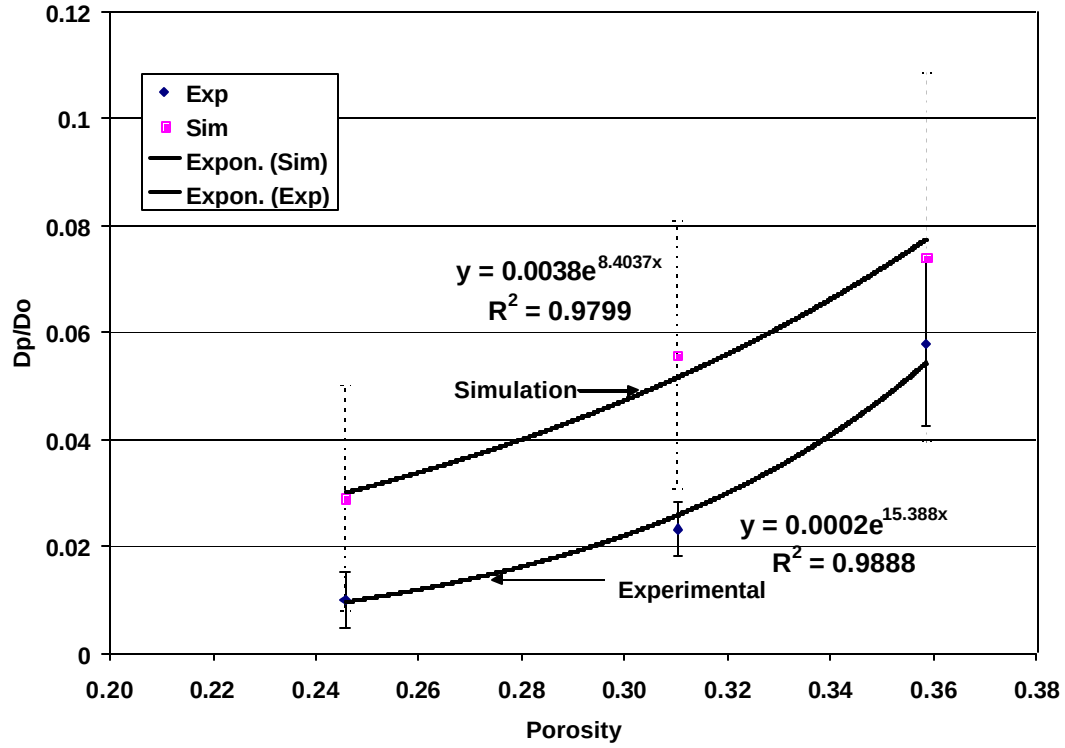

Figure 57 Comparison between simulation and experimental transverse diffusivity values for hand sheets

In all the plots 95% confidence interval has been used. Above plot shows that most of the inplane values are in fair agreement with experimental values. Overall, Dp/Do increases with the increase in porosity. The simulation results show a more uniform relationship with porosity. The experimental in-plane diffusivity values have more scatter due to difficulty in accurately measuring in-plane diffusivity.

As clearly visible from above figure that transverse diffusivity values for both simulation as well as experiments increase with increase in freeness. In other words, paper samples which are less refined have higher values of diffusivities than the more refined samples. As seen in Figures 56 and 57, general trend observed both in simulation and experimental results are very similar indicating that our method is able to capture the overall effect of structure on diffusional transport. One of the reasons for the diffusivities trend in Figure 56 and 57 is due to decrease in porosity with increased refining. The transverse diffusivities by random walk simulation range from 2% for CSF 220 to 14 % for CFS 670 of the normal diffusivity of water vapor in air and agree closely with experimental data. Inplane diffusivity values are approximately 2 to 3 times higher than transverse diffusivity. Dp/Do, pore diffusivity ratio, from simulation is higher than from experimental work at any porosity. This shows that we are underestimating the tortuosity possibly due to lower resolution of our images, hence giving the higher pore diffusion coefficient.

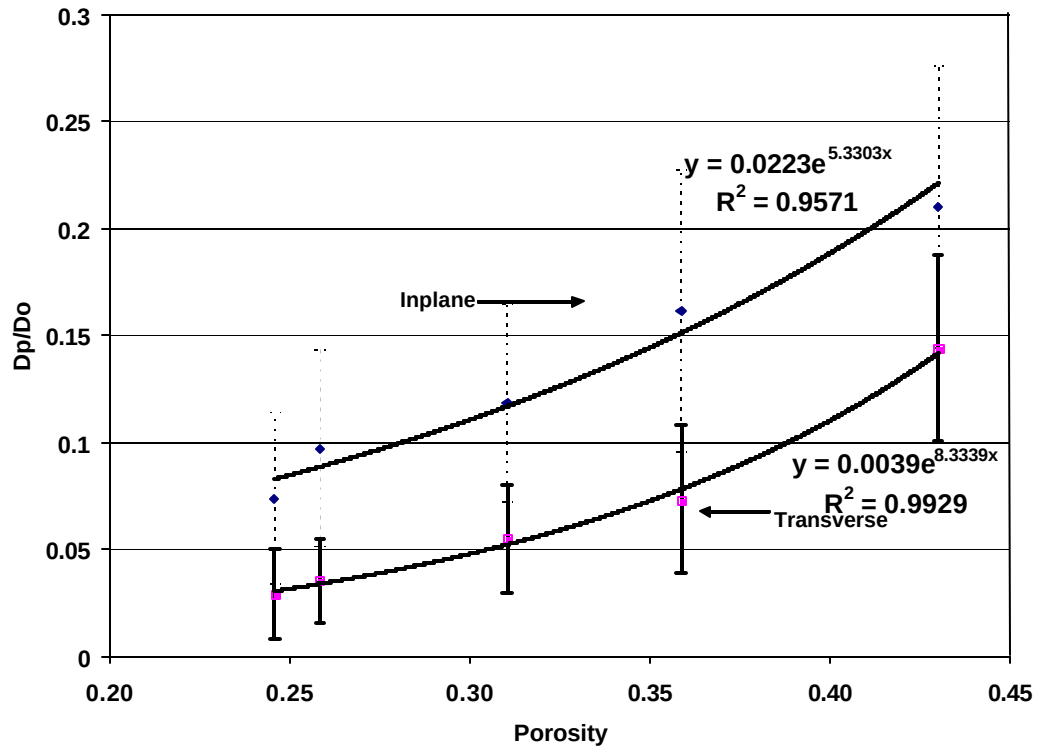

Figure 58 Comparison between transverse and inplane diffusivity values (from simulation) for hand sheets

In the above figure, all the diffusivity values have been obtained by simulation. For all the samples in-plane diffusivities are higher than the transverse values (by approximately twice) suggesting that paper structure exert more resistance to transport in the transverse direction than in in-plane direction. The reason for this kind of behavior can be explained as follows. Because of the layered structure of paper, most of the fibers are oriented along inplane direction such that when water vapor molecules diffuse, they experience less resistance because of the less tortuous path in comparison with transverse direction path (Figure 58). Tortuosity values were obtained according to Equation 20 and plotted in Figure 59. In-plane diffusivities are approximately 2 times higher than transverse diffusivities.

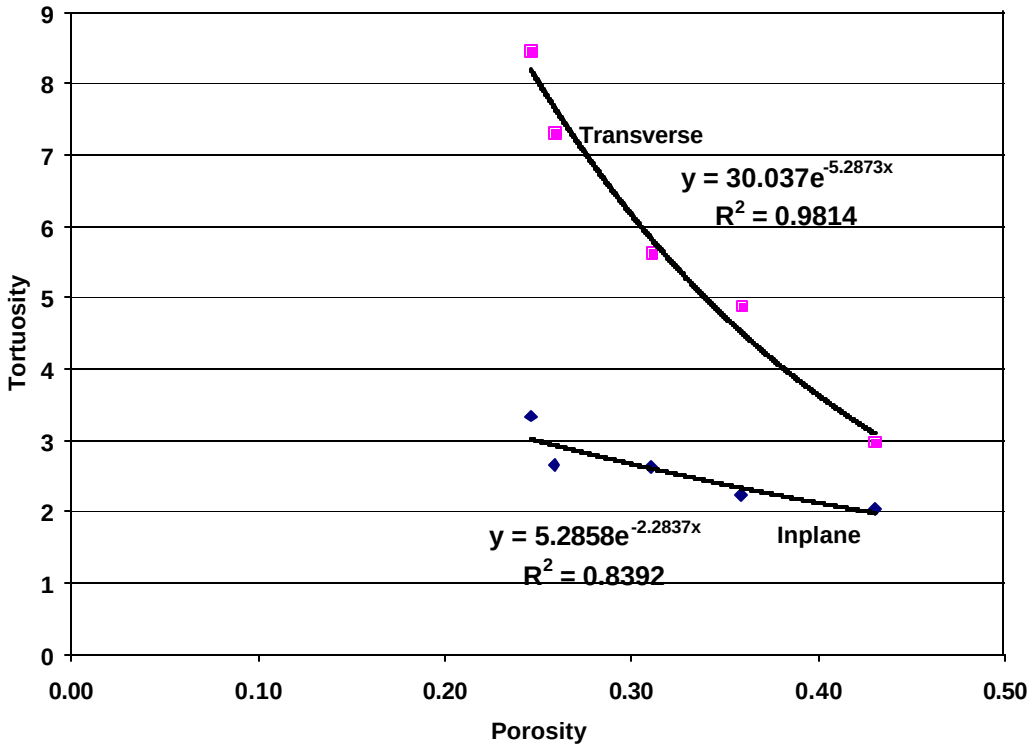

Figure 59 Comparison between transverse and inplane tortuosity values (from simulation) for hand sheets

Pore Diffusivity - Summary

We have developed random-walk algorithms which enable us to compute the pore diffusivity of heterogeneous media such as paper. Random-walk simulation technique combined with image analysis has been shown to be a promising tool to assess the transport characteristics of paper at low humidity. It has been found that transverse diffusivity values are lower than the inplane diffusivity values for all the paper samples. This trend has been observed both in simulation as well as in experimental results. The diffusivity values increase with the increase in porosity because of more open and less tortuous structure. A good agreement has been found between simulation and experimental results for transverse and inplane diffusivity values. For some samples the experimental and simulation do not agree well. The probable reason for this could be the swelling of fibers at RH 30%, hence hindrance to the actual path for diffusion to occur during experiments. The

second reason could be the underestimation of tortuosity because of low resolution of the 3 D structure of paper samples obtained using X-µCT.

Although the method adopted here is based on some assumption, idealization, and limitations, nonetheless it builds a foundation to deal with more complicated problems in future. This intriguing model could be of practical significance to papermakers if applied carefully.

SIMULTANEOUS DIFFUSION IN PAPER

Introduction and Background

Fluid transport occurs in a variety of physical processes of interest to engineers, physicists, physiologists, and biologists. The diffusion of water vapor within porous materials such as paper is a phenomenon of practical interest in paper and chemical engineering as well as in several other life sciences. Water vapor diffusion in paper has significant impact on the performance of various paper properties and its end use applications.

The three dimensional structure of paper i.e. the matrix of fibers and void spaces of paper plays very critical role during its manufacturing processes due to its impact on the transport properties for water and water vapor. Cognizance of relationships between the fibrous structure and its transport coefficients could be beneficial in maintaining the quality of the final product and saving the energy during papermaking operations such as wet web dewatering, pressing, drying, and coating. As paper is subjected to various relative humidity during end use applications, understanding moisture diffusion in paper is essential for optimizing the performance paper products.

The transport of water or other liquids in a fiber web is a dynamic phenomenon. The fiber web is a porous medium with pores of different sizes. Fibers can be considered impermeable only at very low relative humidities that we have modeled as “Pore Diffusion”. In this section we will again consider the same complex structures i.e. same paper sample. But at higher relative humidities, pores as well as fibers will behave as permeable media, although the rate of diffusion could be much slower in fibers than in pores.

The basic laws of mass, momentum and energy transport constitute a framework within which majority of chemical engineering problems are coined. The partial differential equations known as equation of change determine how aforementioned properties change with position and time within a given region. Manuel Laso [Laso, 1994] suggested a novel approach to the solution of these equations. He also provided possible approaches for treatment of boundary conditions within the stochastic framework. He used stochastic approach to show that it provides a natural microscopic interpretation of the processes underlying the continuum-mechanical equations of change.

Many investigators [Nakashima, 2002, Hellen et al., 2002, Rosium, 1993] determined pore diffusivity in various porous materials, for some materials it was actually effective diffusivity where only one medium was conducting. Reyes et al. [Reyes, 1991] determined the effective diffusivities in catalyst pellets. They simulated compressed and sintered porous media by using random-loose

aggregates of spheres distributed in size and partially overlapped to achieve the required porosity. They used Monte Carlo techniques to determine diffusivities in Knudsen, transition, and molecular diffusion regimes.

Some researchers [Massoquette, 2003a, Massoquette, 2003b Lescanne et al., 1992, Laso, 1994] used different modeling approaches and did experimental work in the pursuit to study the diffusion of water vapor in paper. Nevertheless, not much work has been done with regard to simultaneous diffusion in porous media as far as simulation is concerned. But at the same time many researchers have investigated various porous media and obtained their diffusion coefficient by analytical and experimental method. A few researchers have found effective diffusivity of various paper samples using diffusion cell [Nilsson, 1993] and diffusion cup method [Lescanne et. al., 1992].

L. Nilsson et al. [Nilsson, 1993] investigated the diffusion of water vapor through pulp and paper in a diffusion cell. The diffusion cell used in their experimental work was having two chambers differing in relative humidity. Paper samples used in their experiments were of many varieties and of varying basis weights (weight per unit area). Their experiments were performed at different temperatures and relative humidity to see the effect of the same on the effective diffusivity. They concluded that effective diffusivity in paper is independent of relative humidities when below 58% contrary to what has been found by Massoquete et al.[Massoquette et.al., 2003b] and Ahlen [Ahlen, 1970].

Lescanne et al. [Lescanne et. al., 1992] studied diffusion mechanism of water in paper using the cup method. They used eight sheets of paper of 300 g/m^2 for their experimental work. They designed a model of linear relaxation to describe the diffusion in paper for both steady and unsteady states. Their theoretical and experimental results were in good agreement.

Liang et al. [Liang et.al., 1990] measured the transport rates of water, n-propanol, and mixtures of these two through samples of kraft pulp and filter paper. Their experiments were done at different temperatures and relative humidity to see the effect of the same on the effective diffusivity. Their results showed that gas-phase transport within pores and interstices dominates the mass-transfer process. Transport coefficients for n-propanol decrease as the relative humidity was increased. They found that dominant mechanism of gas-phase transport is probably bulk-gas diffusion. They also found that transport coefficients for water in filter paper increase with increase in relative humidity. One of their findings was that transport coefficients for water tend to increase more sharply with increasing temperature than for n-propanol.

Nilsson and Stenström [Massoquette, 2003a] used a cell model to describe fibrous porous medium consisting of cylindrical and band-shaped fibers to study diffusion in paper and nonwoven fabric though their thickness. Their theoretical model was based on solution to the diffusion equations at steady state and agreed well with analytical correlation given by Raleigh (1892). The model was also compared with the experimental data which they obtained using the diffusion cell [Nilsson, 1993]. The model for diffusion around cylindrical fibers predicted well the diffusion through nonwoven medium. Diffusion through pulp sheets and hand sheets of unrefined pulp was described well by the model for band-shaped fibers. Nonetheless, their model could not work for newsprint, for which it

gives lower diffusivity values. The presence of fines and fillers in newsprint could be the reason for this anomalous behavior as mentioned by them.
Foss et al. [Foss et al., 1999] devised a model of simultaneous heat and mass transfer to explain transient moisture sorption by paper from humid air. Three resistances for water vapor diffusion namely the laminar boundary layer above the surface of the paper sheet, tortuous voids between the fibers, and vapor absorbed as liquid into fibers were incorporated in their model.

All of the researchers [Massoquette, 2003a, Massoquette, 2003b, Foss et al., 1999, Nilsson, 1993, Lescanne et. al., 1992, Liang et.al., 1990] mentioned above have studied the diffusion of water through paper only in the transverse plane i.e. through thickness except for Massoquete et al. [Massoquette et.al., 2003b] who have reported in-plane diffusivities as well.

Method

Hand sheets (paper samples) of varying porosity having different internal structure imaged by X-Ray Micro Computed Tomography. More details on hand sheets and image analysis were given in earlier sections.

The method used for simultaneous diffusion is based on stochastic dynamic approach [Laso, 1994]. In order to illustrate the method, let us consider unsteady state diffusion equation:

$$\frac{\partial f}{\partial t} = D\frac{\partial^2 f}{\partial x^2} \qquad (21)$$

Where, D is the diffusion coefficient and f(x, t) is the number density function

Above partial differential equation with some boundary conditions is not easy to solve numerically. So an analogy has been drawn between this equation (Eq 21) and Fokker-Planck equation (FPE, Eq 22). FPE [Risken, 1989] is also a partial differential equation like the above diffusion equation, and therefore not easy to solve. The main purpose of this analogy is that the FPE can be cast in the form of a stochastic differential equation (SDE). This SDE is much easier to solve numerically than FPE; actually it could be solved with the techniques which are much easier to implement than standard discretization methods such as finite difference, finite elements etc.

Fokker and Planck were the first to use Fokker- Planck equation (FPE) to study Brownian motion in a radiation field [Risken, 1989]. FPE is also known as diffusion equation in polymer kinetic theory [Bird et al., 1987]. It can be written in general form as:

$$\frac{\partial}{\partial t}p(t,x) = -\frac{\partial}{\partial x}.[A(t,x)p(t,x)] + \frac{1}{2}\frac{\partial}{\partial x}\frac{\partial}{\partial x}:[B(t,x)p(t,x)] \qquad (22)$$

Where:
t: time
x : d-dimensional vector of coordinates
$p(t,x)$: probability density

A(t,x): d-dimensional vector
B(t,x): positive-semidefinite symmetric *d* x *d* matrix

The term containing *A* in FPE (eq 22) is called drift term and term containing *D* is the diffusion term.

Assuming *A* and *D* satisfy certain conditions (Lipschitz, linear growth, continuity, symmetric positive semi-definite *D*), it can be proved [Kallianpur, 1980] that FPE corresponds to a Markov process with the following infinitesimal generator:

$$d = A(t,x)\frac{\partial}{\partial x} + \frac{1}{2}B(t,x) : \frac{\partial}{\partial x}\frac{\partial}{\partial x} \qquad (23)$$

and it is the solution of the multivariate stochastic differential equation:

$$dX_t = A(t, X_t)dt + C(t, X_t).dW_t \qquad (24)$$

where A(t,x) is same as in equation (FPE) and,

$$B(t,x) = C(t,x).C^T(t,x) \qquad (25)$$

Now comparing the diffusion equation 21 with FPE (eq 22) gives,

A(t,x) = 0 and B(t,x) = 2D, hence associated SDE for diffusion equation will be:

$$dX_t = \sqrt{2D}\, dW_t \qquad (26)$$

where *W* is a one-dimensional Wiener process [Gardiner, 1983].
Consequently the problem has been reduced from second order differential equation (21) to an ordinary first order stochastic differential equation (26).

Kloeden and Platen have covered numerical solution of SDEs comprehensively in Numerical Solution of Stochastic Differential Equation [Kloeden et al., 1992]. Time discrete approximation has been adopted to solve SDE (Eq. 26) of our interest. Using Euler-Maruyama approximation [Maruyama, 1986, Kloeden et al., 1992] we get for a given time discretization of the time interval [0, t_f]:
$0 = t_0 < t_1 < \ldots.. < t_i < \ldots\ldots < t_f$
Assuming them to be equidistant:
$t_{i+1} = t_i + ?t \qquad i=0,\ldots\ldots\ldots f\text{-}1$
the time discrete approximation to SDE (Eq.25) will then be:

$$X_{i+1} = X_i + \sqrt{2D\Delta t}\, W_i \qquad (27)$$

W_i : Gaussian random number with zero mean and unit variance.
The Eq 27 will be used later.

As we are dealing with the diffusion of water vapor at steady state, there is no accumulation of water vapor at the interface of fiber and pore and hence there should be equality of fluxes i.e.

$$Dqo\frac{\partial fq}{\partial x} = Do\frac{\partial fo}{\partial x} \tag{28}$$

Where,
Dqo : Intrinsic diffusivity of fiber
Do : Intrinsic pore diffusivity i.e. diffusion coefficient in open space.
Subscript 'q' corresponds to fiber and 'o' corresponds to pore or void
Since the equation to be solved in both medium is of the same form, SDE will also be of the same form for both the media.

The procedure adopted for molecular movement in simultaneous diffusion is same as pore diffusion (shown earlier) except at the fiber-pore interface. But now in simultaneous diffusion molecules can also enter inside fiber. Since diffusion coefficient of water vapor inside fiber (i.e. intrinsic fiber diffusivity) is not known *a priori*, several ratios of diffusivity (rod) have been taken.

As mentioned earlier that if particles jump within pore or fiber then it will advance according to the technique discussed in earlier. Now what happens if molecule jumps from pore to fiber or vice-versa? Following the approach by Laso [Laso, 1994], Figure 60 shows schematically the scenario when a molecule moves from pore to fiber.

From Pore to Fiber:

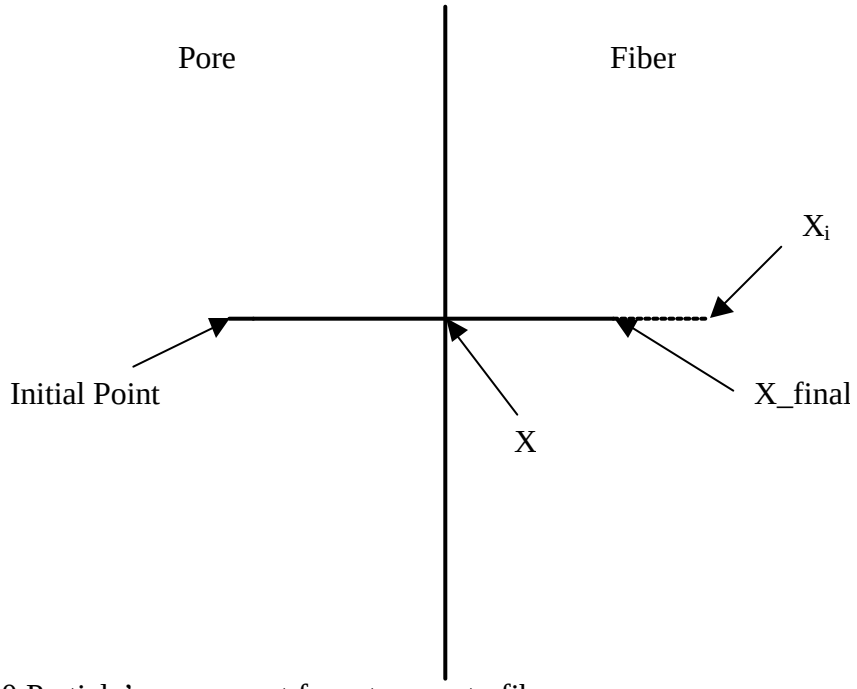

Figure 60 Particle's movement from to pore to fiber
(For explanation only, NOT TO SCALE)

As one would expect, due to the lower mobility of the entering medium the distance traveled will be less. Hence the modified distance for that step for the molecule is given as,

$$X\_final = X + \sqrt{rod} * (Xi - X) \quad (29)$$

Where rod = Dqo/Do

Prior to entering the lower mobility fiber we need to ascertain one important criteria, i.e. whether the molecule can enter the low mobility medium or not. This is of course dependent on the ratio of diffusivities. It has been shown by Laso [Laso, 1994] that the above condition can be mathematically met by satisfying

$$\mathbf{R} < \sqrt{rod} \quad (30)$$

Where **R** is a random number drawn from a uniform distribution in [0, 1], if the above condition is true then molecule goes from pore to fiber otherwise it will be reflected back into the high mobility medium (pore). This condition ensures equality of fluxes at the pore-fiber interface taking into account differences in mobility.

In the above figure if there were pore in place of fiber then molecule could have jumped to Xi but due to the difference in mobilities (?o > ?q), the final distance was modified according to equation 29. For example, if rod =1 that means mean free path of particle in fiber and pore is the same, hence equation reduces to,

X_final = Xi

Case I: rod =1, actually means that particle is just jumping in open space and so Di/D should be 1, where Di is effective diffusivity and i can be x, y or z directions. Our open space simulations give Di/Do values of 1.0 ± 0.01. This again confirms the validity of our simulation method.

Case II: rod = 0, actually means that particle is just jumping in pore space. Hence Di/D should be equal to pore diffusivities for the respective paper samples. As will be shown later, this is indeed the case. The random number R cannot be less than zero; hence particle can not enter the fiber.

Case III: 0< rod < 1 is the case in which we are interested. Here both pores as well as fibers are permeable. Since the intrinsic fiber diffusivities are not *a priori*, we conducted simultaneous diffusion simulations using possible range of rod from 0 to 1. This essentially covers the entire range of intrinsic diffusivities from impermeable to highly permeable (same as normal diffusion in open space). Basically we used rod = 0.02, 0.04, 0.06, 0.08, 0.1, 0.2, 0.4, 0.6, 0.8., which corresponds to various RH ranging from 0% to 100%.

Once the molecule crosses pore-fiber interface, it will advance by finding nearest pore. If this distance is more than five times mean free path then it will follow FPT method otherwise true random walk similar to method described in pore diffusion. The walk will be continued until molecule escapes from the sample. If condition (Eq 30) is not satisfied then particle will come back to pore and follow the same procedure as described above.

From Fiber to Pore:

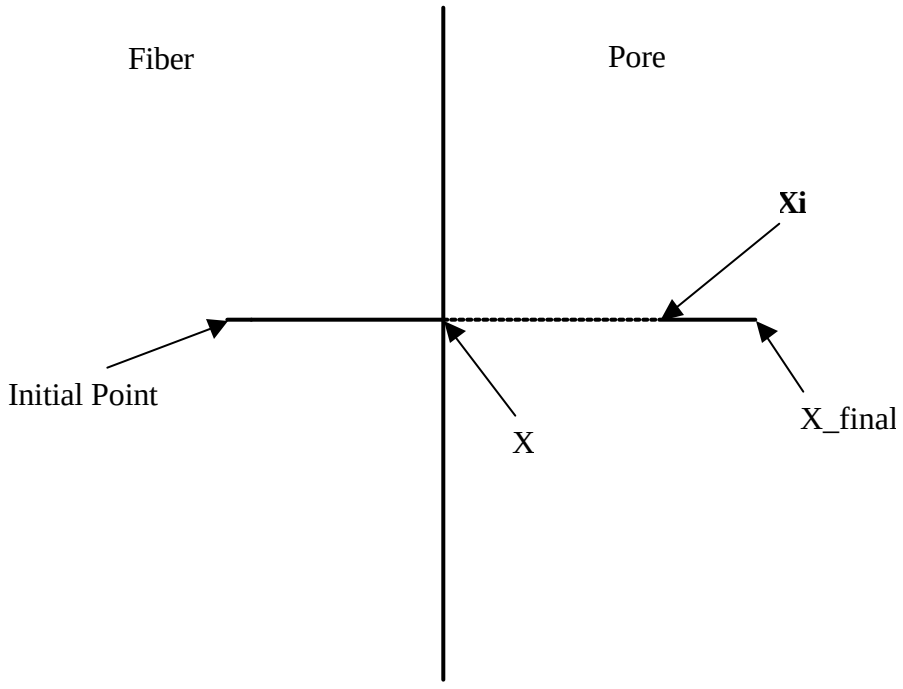

Figure 61 Particle's movement from fiber to pore
(For explanation only, NOT TO SCALE)

Similarly, when the molecule goes from low mobility medium (fiber) to high mobility medium (pore), as one would expect, the distance of travel should be increased due to higher mobility of entering medium. Modified distance when going from fiber to pore is given by,

$$X\_final = X + \frac{1}{\sqrt{rod}} * (Xi - X) \quad (31)$$

All the cases mentioned earlier in pore to fiber case are applicable for the above equation (31) except when rod =0 which will make left hand side of equation infinite. That means this equation is not valid at rod =0, which makes sense. Because, rod is 0 means just pore diffusion without any diffusion in fiber. Which means particle cannot enter fiber, hence particle cannot be inside fiber so there is no probability that particle will jump from fiber to pore when rod is zero. Thus invalidity of equation 31 at rod = 0 is justified.

Once the molecule crosses fiber-pore interface, it will follow the same method described earlier in pore-fiber case, i.e. a combination of TRW and FPT.

Results and Discussion

In this work we have presented an analysis of the process of bulk diffusion in complex porous media such as paper. At various 'rod', effective diffusion coefficients of the paper samples have been estimated using random walk simulation. The analysis is then explicated using following figures and plots. First of all as mentioned earlier, for the case of rod =0, our simulation yields effective pore diffusion. Following table shows the effective diffusion coefficient for the limiting cases of rod = 0 and 1 and how it compares with experimental data.

Table 5 Transverse Diffusivity results for hand sheets (paper samples)

CSF	Porosity	Simulation (Deff/Do)		Experiment
		(At rod = 0)	(At rod = 1)	(Dp/ Do)
570	0.3586	0.07398	1.02238	0.0577
460	0.3103	0.05576	0.99718	0.0232
220	0.2457	0.02897	0.98595	0.0100

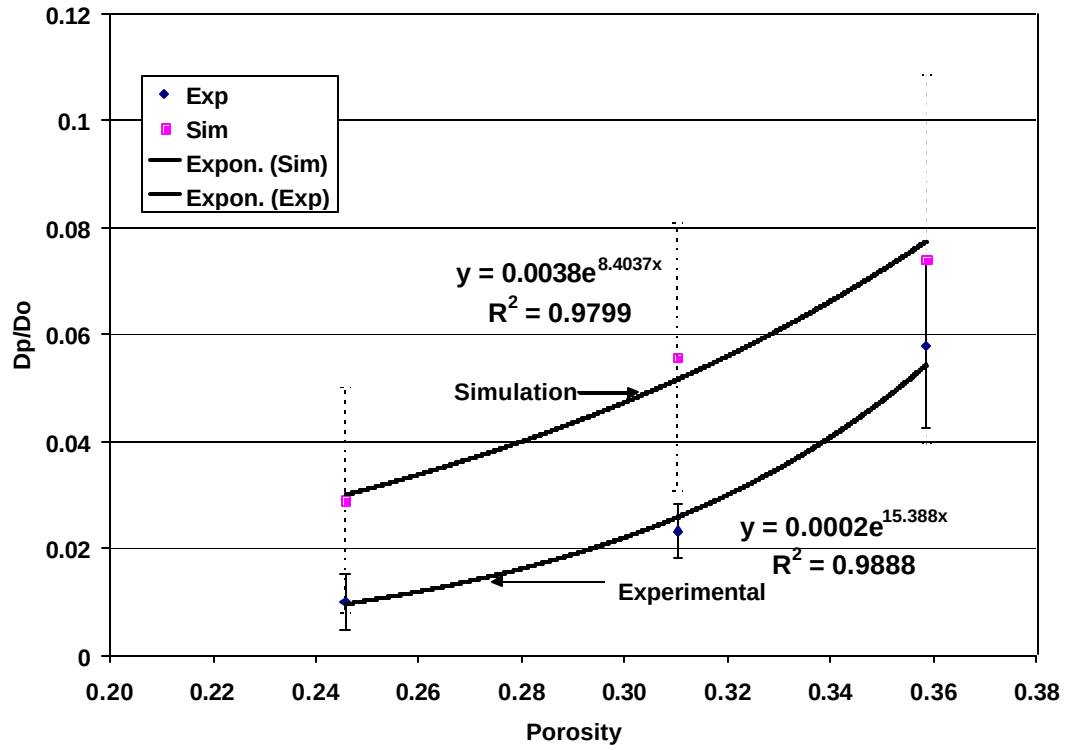

Figure 62 Comparison between simulation and experimental results for dimensionless transverse effective diffusivity in pore space vs. porosity

As shown in Table 5, our results compare reasonably well with experimental data at rod = 0, and theoretically expected values at rod =1. Comparison of effective pore diffusivity as a function of porosity is shown in Figure 62.

The simulation results are compared with the experimental values [Massoquette et.al., 2003b, Holmstad, 2004] at various RH. Following figure shows the comparison between these two for inplane diffusion coefficients at 50% relative humidity. Plot shows fair agreement between simulation and experimental results. Both results show that inplane diffusivity increases with the increase in porosity. The reason is less tortuous path followed by particles with the increase in porosity. The results could not be compared at other relative humidities because of unavailability of experimental data. Unlike transverse diffusivity results, even as the porosity increased approximately from 0.25 to 0.45, in-plane diffusivity increases from 0.15 to only ~ 0.21. This is again a characteristic feature of layered structures.

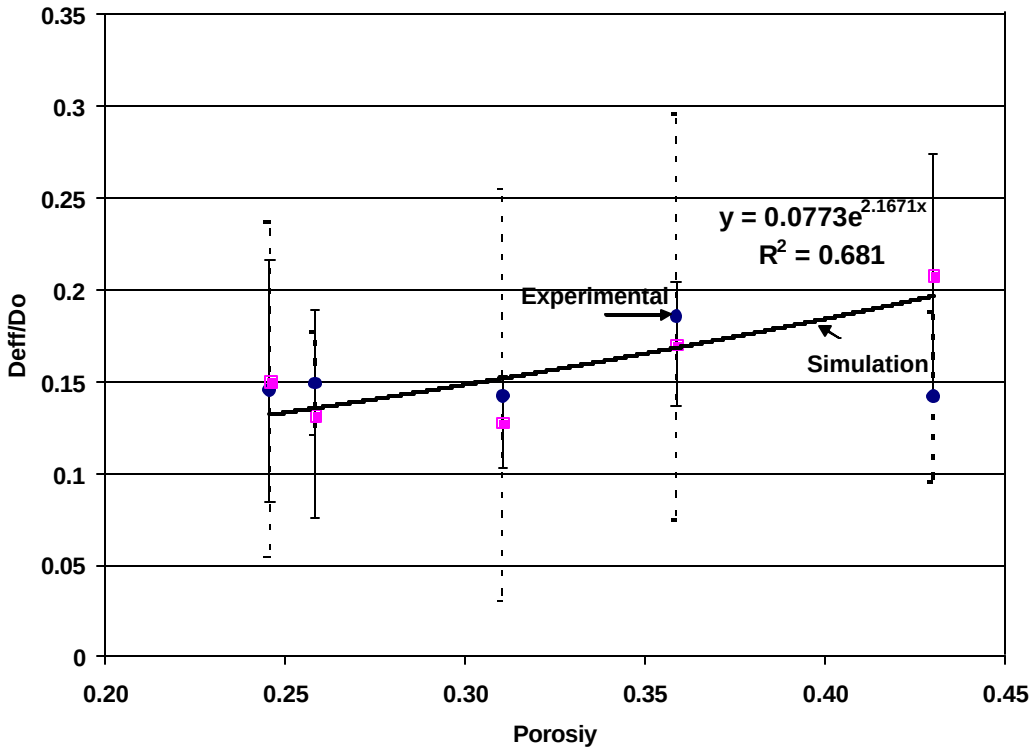

Figure 63 Comparison between simulation and experimental results for dimensionless inplane diffusion coefficient vs. porosity at 50% RH.

For transverse plane we got experimental data at various RH and hence they have been plotted in the following figures. We have plotted effective fiber phase diffusivity, Dq vs. RH, where Dq has been calculated as follows:

We have calculated Dp earlier where we assumed fibers to be impermeable and all the moisture transport occurring in pore space only. Deff has been calculated using stochastic dynamic approach [Laso, 1994] earlier in the present chapter. Now only Dq is left which has been calculated as follows,

Ramarao et al.[Massoquette et al., 2003a] have shown that:

$$Deff = Dp + \frac{rqDqq(e^{mq1} - e^{mqo})}{m(c_1 - c_o)} \qquad (32)$$

where,

q1, qo= Equilibrium moisture content of paper at RH h1 and ho respectively (kg of water /kg dry paper)

c_1, c_o = Water vapor concentration at corresponding relative humidities h1 and ho (gmol/ cm^3)

Dp = Effective pore diffusion coefficient (cm^2/sec)

Dqq = Reference bound water diffusivity within fiber matrix

m = Empirical constant
$?_{q:}$ = density of fiber
Deff = Effective effusion coefficient of whole structure

The above Equation 32 can be approximated as [Massoquette et al., 2003a],
Deff ˜ Dp + Dq (33)
or Dq ˜ Deff - Dp

Using experimental data and theoretical analysis solving simultaneous diffusion equation Ramarao et al.[Massoquette et.al., 2003b, Holmstad, 2004] reported Dp and Dq values for samples of varying structure considered here. Dq/Do values obtained from our simulation and experimental work [Massoquette et.al., 2003b, Holmstad, 2004] have been plotted against relative humidity for different samples. Effective fiber diffusivity values from simulation have been obtained by comparing the simulated total effective diffusivity (Deff) with experimental data at a given RH and using the corresponding ratio of intrinsic diffusivities (Dqo/Do). Using this rod and Deff, corresponding Dq can then be obtained.

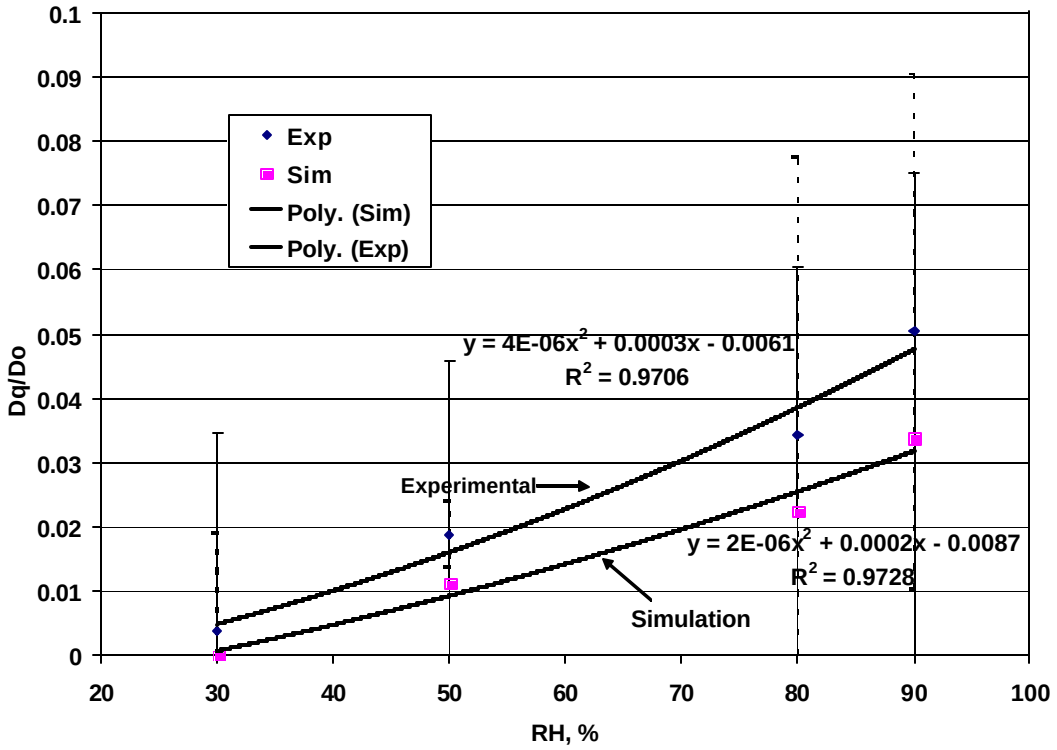

Figure 64 Comparison between simulation and experimental results of transverse diffusivity at varying Relative Humidity (RH) for sample 570 (e = 0.3586)

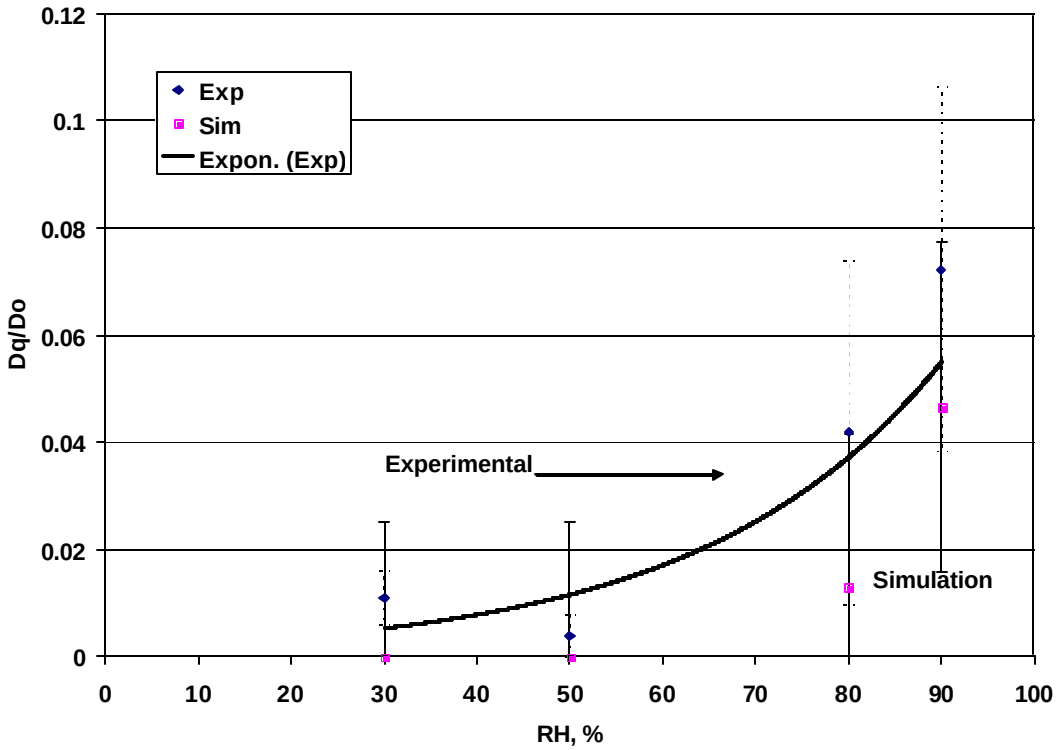

Figure 65 Comparison between Simulation and Experimental results of transverse diffusivity at varying Relative Humidity (RH) for sample 460 (e = 0.3103)

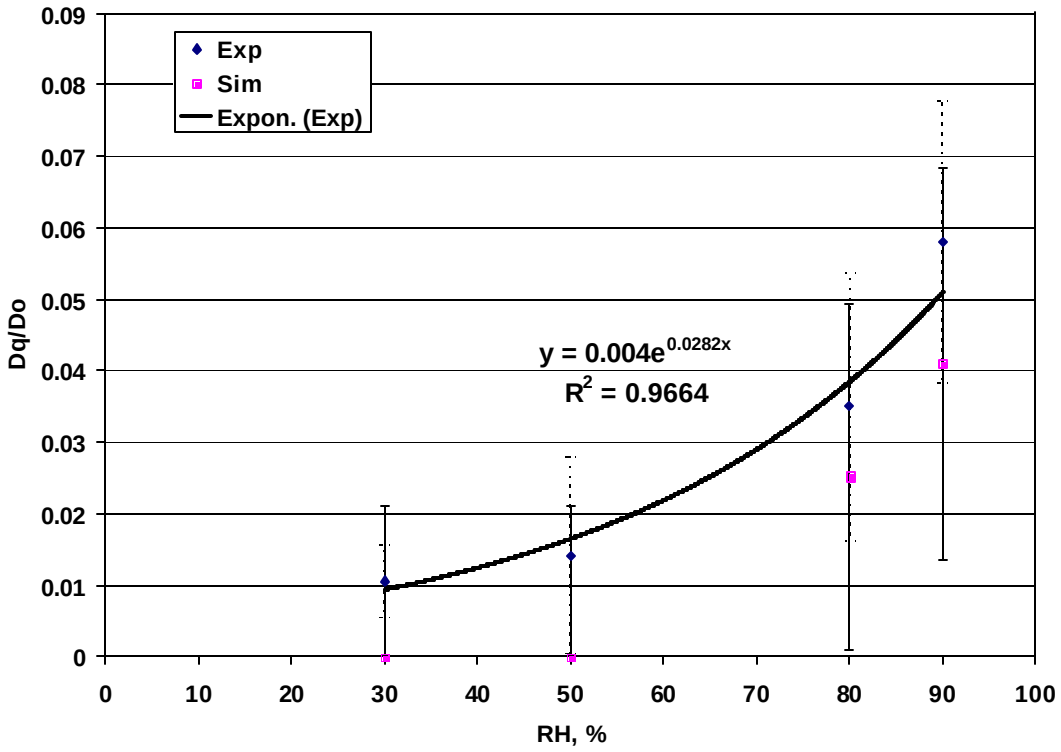

Figure 66 Comparison between simulation and experimental results of transverse diffusivity at varying Relative Humidity (RH) for sample 220 (e = 0.2457)

As expected, the overall trend is same for both simulation as well as experimental values i.e. increase in Dq/Do with the increase in RH. Simulation diffusivity values are lower than experimental values at any relative humidity. The reason could be the overestimation of tortuosity of the 3 dimensional structure by X-ray tomography because of its low resolution. This is probably due to the hygroscopic nature of cellulose fibers, which makes them more conductive with the increase in RH.

Effective diffusion coefficients are plotted against relative humidities in the following figures. Effective diffusion coefficient (Deff) is the diffusion coefficient for whole structure.

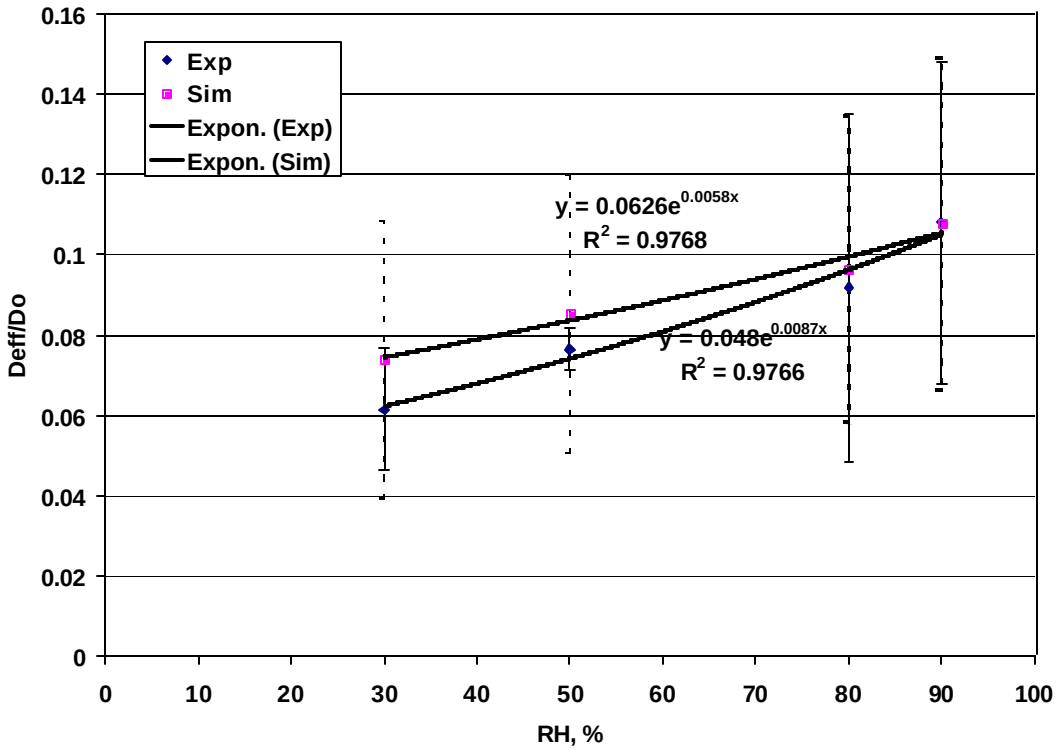

Figure 67 Comparison between simulation and experimental results of effective transverse diffusivity at varying Relative Humidity (RH) for sample 570 (e = 0.36)

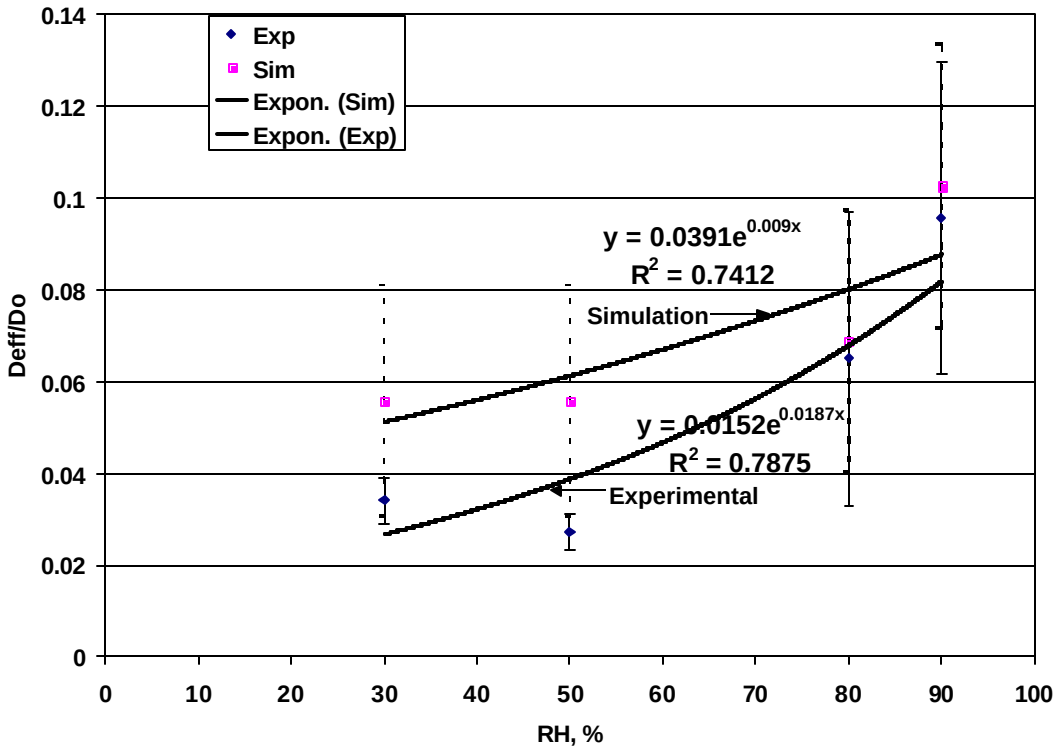

Figure 68 Comparison between simulation and experimental results of effective transverse diffusivity at varying Relative Humidity (RH) for sample 460 (e = 0.31)

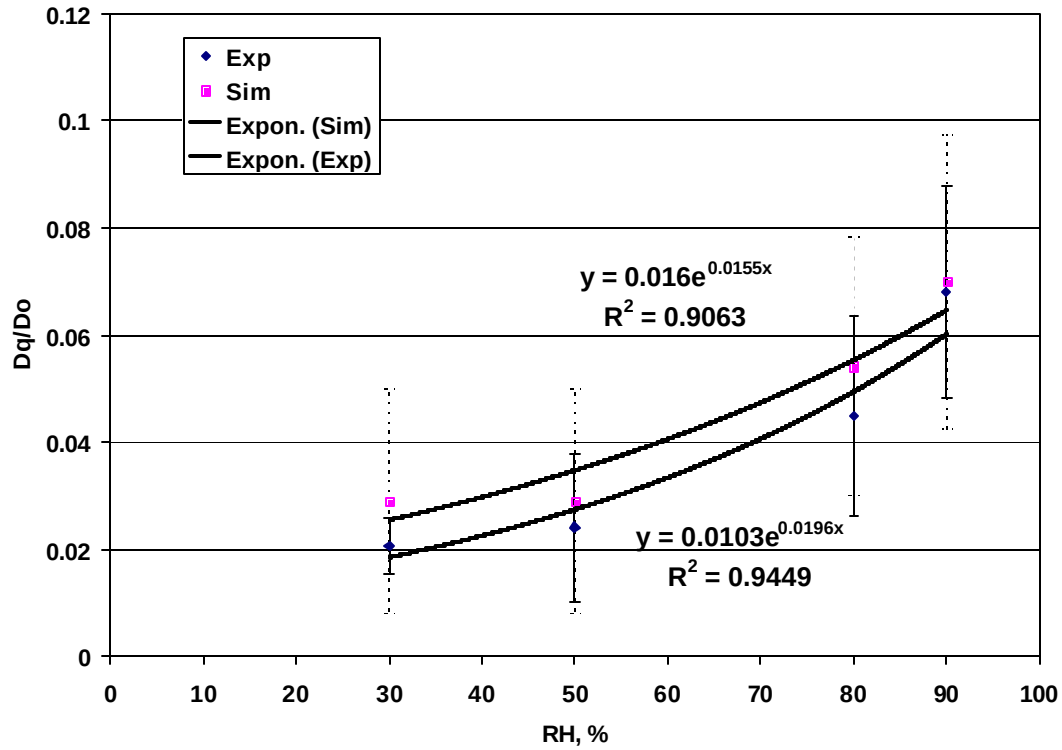

Figure 69 Comparison between simulation and experimental results of effective transverse diffusivity at varying Relative Humidity (RH) for sample 220 (e = 0.25)

Interestingly, effective diffusion coefficients by simulation for each sample are higher than the experimental values unlike Dq. The reason is same as for Dq but here we are underestimating pore space structure because pore and fiber spaces are complementary of each other. Overall trend is same for both simulation as well as experimental values i.e. increase in Deff/Do with the increase in RH. The reason for the above trend is that cellulose fibers are hygroscopic in nature, which makes them more conductive with the increase in RH and thus increase in fiber diffusivity which finally contributes to increase in effective diffusivity of paper samples

Knowing the rod corresponding to each RH, as described earlier, it is now possible to estimate the intrinsic fiber diffusivity at varying conditions. Following table shows Dqo/Do (rod) for paper samples at different RH and porosities.

rod =Dqo/Do (34)

Where, Dqo: Intrinsic diffusivity of fiber space

Do: Intrinsic diffusivity of pore space

Table 6 Dqo/Do (rod) for hand sheets (paper samples) at different RH

CSF	Porosity	Dqo/Do				
		At 30% RH	50% RH	80% RH	85% RH	90% RH
670	0.43	0	0	0	0.038	0.06
570	0.36	0	0	0.01	0.012	0.018
460	0.31	0	0	0.004	0.007	0.028
280	0.26	0	0	0.004	0.006	0.01
220	0.25	0	0	0.018	0.016	0.033

In the above table, for almost all the porosities rod ˜ 0 at lower RH confirming earlier prediction in literature that, fibers are non-conductive at low RH.

In general, for the slightly refined pulp fibers the intrinsic diffusivities increase from rod ˜ 0 (rod) at low RH to rod ˜ 0.06 at high RH. While for the highly refined fibers, Dqo increases from rod ˜ 0 at low RH to ˜ 0.03 at high RH. The increase in Dqo to explain the whole range of Deff in slightly refined fibers is about twice as that in highly refined fibers.

Following figures show the effect of rod on overall diffusion coefficient in all three planes (XY, YZ, ZX).

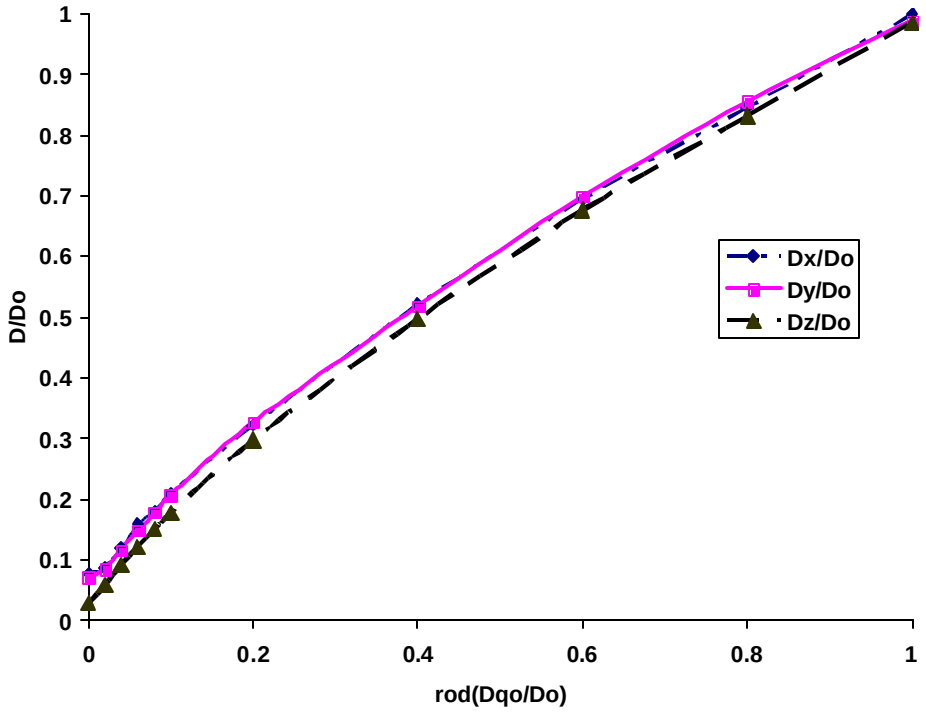

Figure 70 Dimensionless effective diffusion coefficient vs. rod for 220

Figure 70 shows, as rod increases D/Do also increases which is expected because larger rod means higher intrinsic diffusion coefficient of fiber and which in turn contribute toward increasing effective diffusion coefficient overall. It seems diffusivities are about same in X-Z plane (Dx/Do) and Y-Z plane (Dy/Do) at all rods, the reason is same as discussed for pore diffusion in Chapter 4 i.e. most of the fibers are oriented along in-plane such that when water vapor particles diffuse, they experience less resistance because of the less tortuous path in comparison with the transverse plane. Transverse values (Dz/Do) are lower than in-plane values at all rods except at rod =1 which is essentially an open space simulation where diffusivity in all three directions are the same. At rod =0 our simultaneous diffusion code gives the diffusivities values with less than 1% error compared to fiber impermeable case simulations. Hence both these extremes buttress the validity of the code. The following figures show the plot between rod and D/Do for all six types of paper samples.

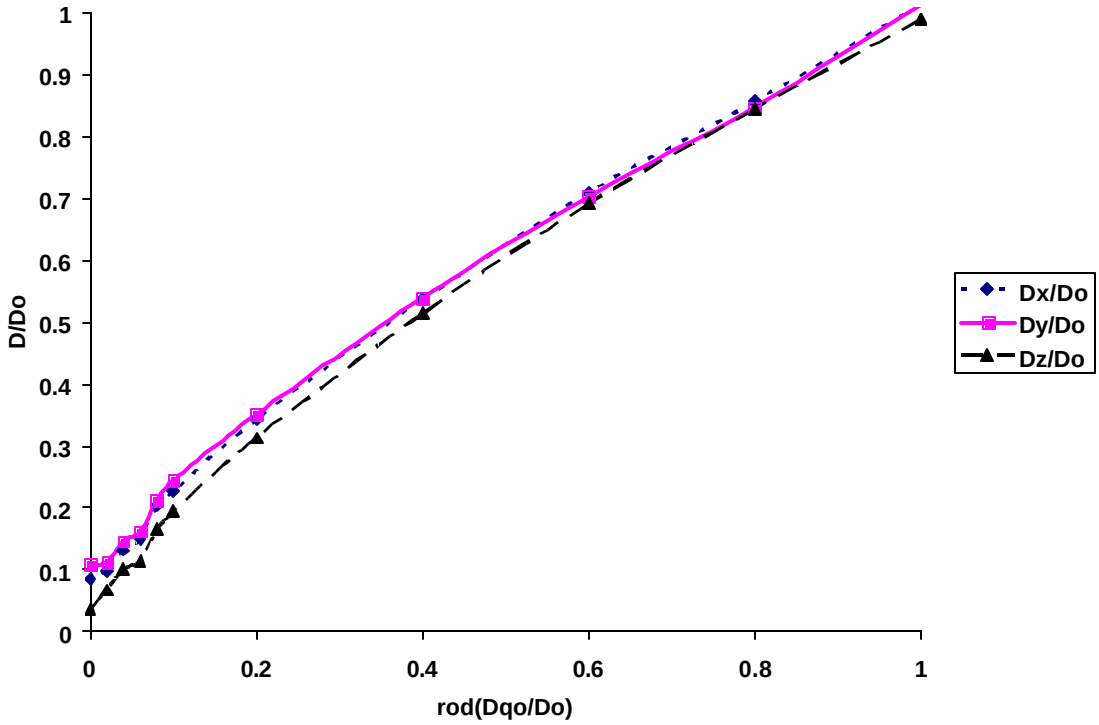

Figure 71 Dimensionless Effective diffusion coefficient vs. rod for 280

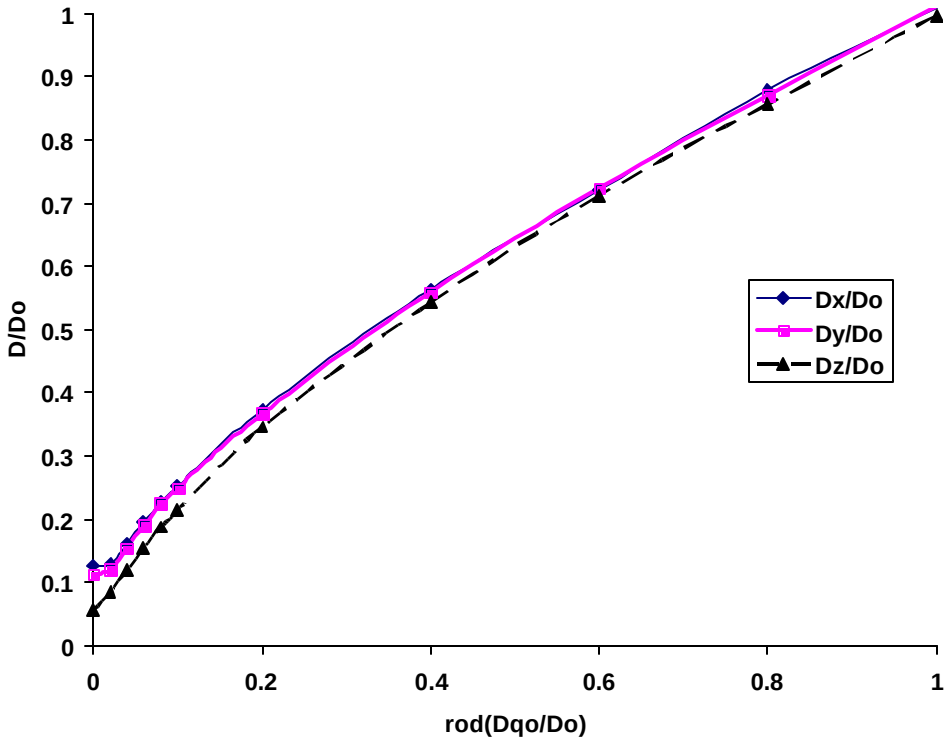

Figure 72 Dimensionless Effective diffusion coefficient vs. rod for 460

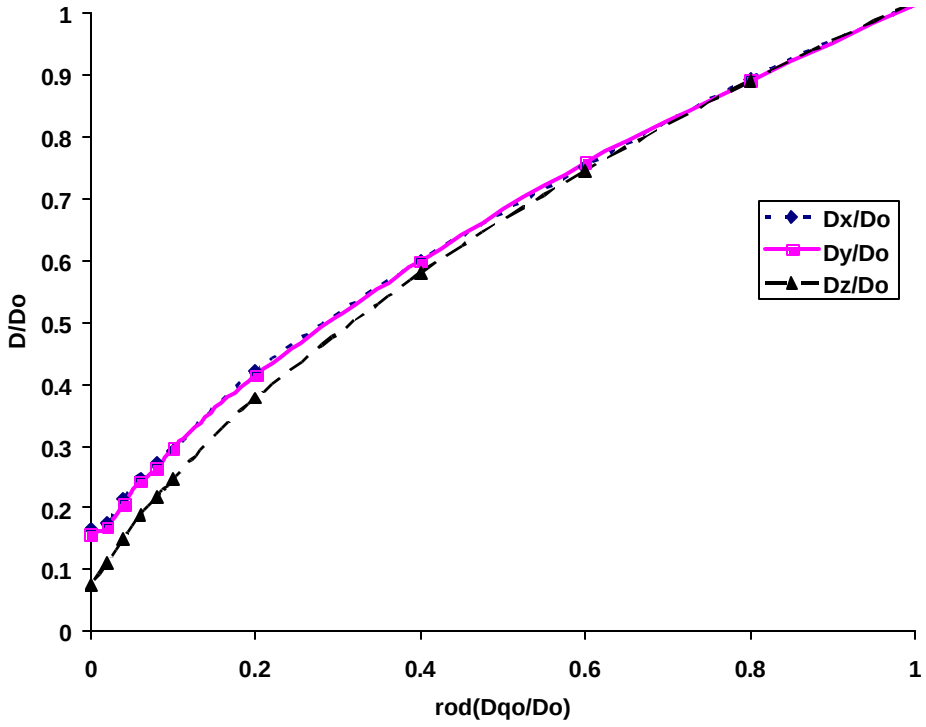

Figure 73 Dimensionless Effective diffusion coefficient vs. rod for 570

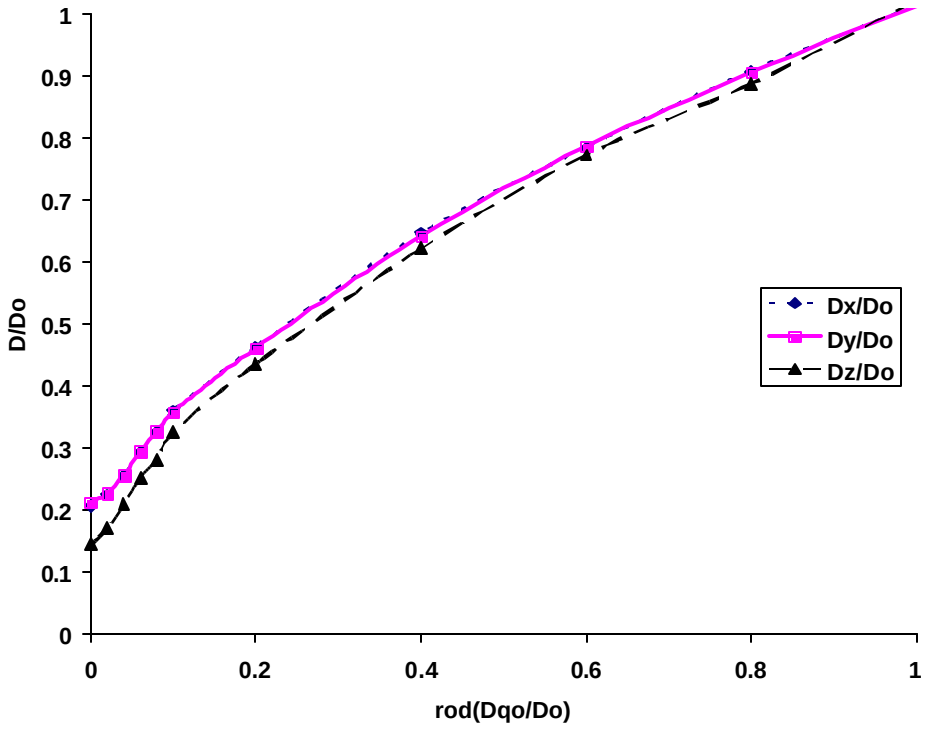

Figure 74 Dimensionless Effective diffusion coefficient vs. rod for 670

In all of the above figures, for a range of e from 0.24 to 0.43 effective diffusion coefficients decrease as rod decreases suggesting that the overall resistance offered by the structure increases with decreasing fiber diffusivity. Above rod >0.8, the diffusivity ratios in all three planes are almost the same suggesting that the structure behaves like an isotropic, homogeneous medium. At lower porosities, however, there are differences in diffusivities between the in-plane and transverse directions or the anisotropic nature of the structure becomes more prominent.

To show clearly where transverse values start deviating from inplane values, plots for 220 (lowest porosity) and 670 (highest porosity) samples only have been shown because all the samples follow the same trend.

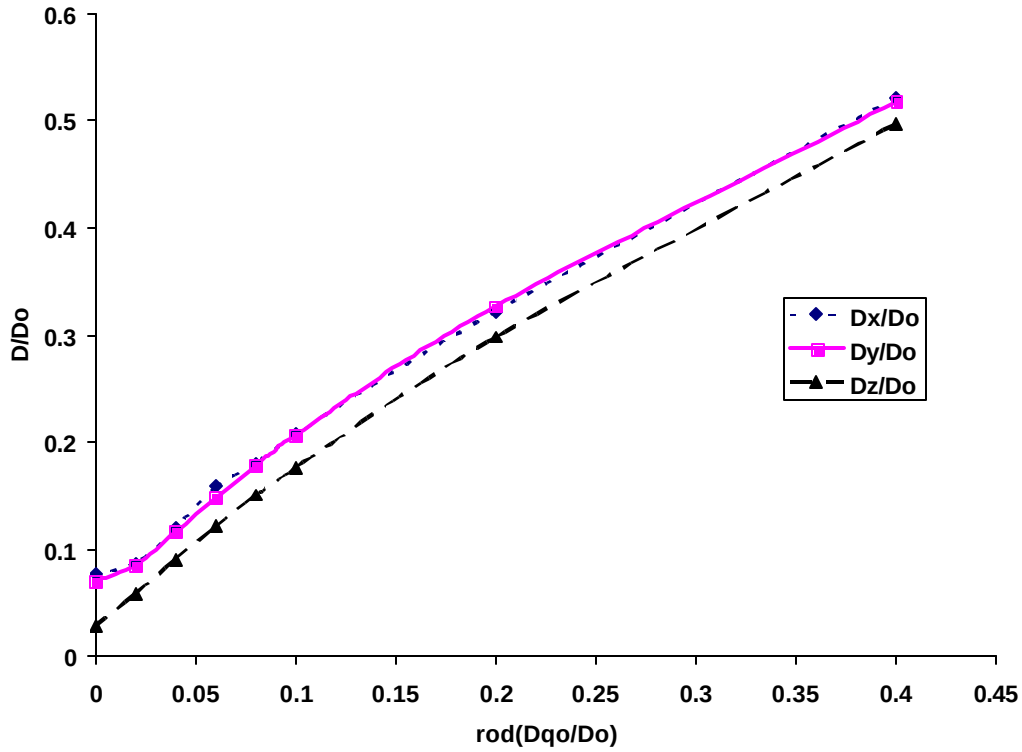

Figure 75 Dimensionless Effective diffusion coefficient vs. rod for 220

Above figure shows that transverse diffusion coefficient values are approximately 0.02 in magnitude less than inplane values at any rod except at rod = 0 (pore diffusion) where they are less than by 0.04. Where as, the percentage difference between inplane and transverse values goes up to 59% (at rod = 0) from 4% (at rod = 0.4). In a nutshell, we can say that as rod decreases heterogeneity of the structure starts playing a role and this occurs when rod < 0.4. Same type of nature has been found for CSF 670 (figure below).

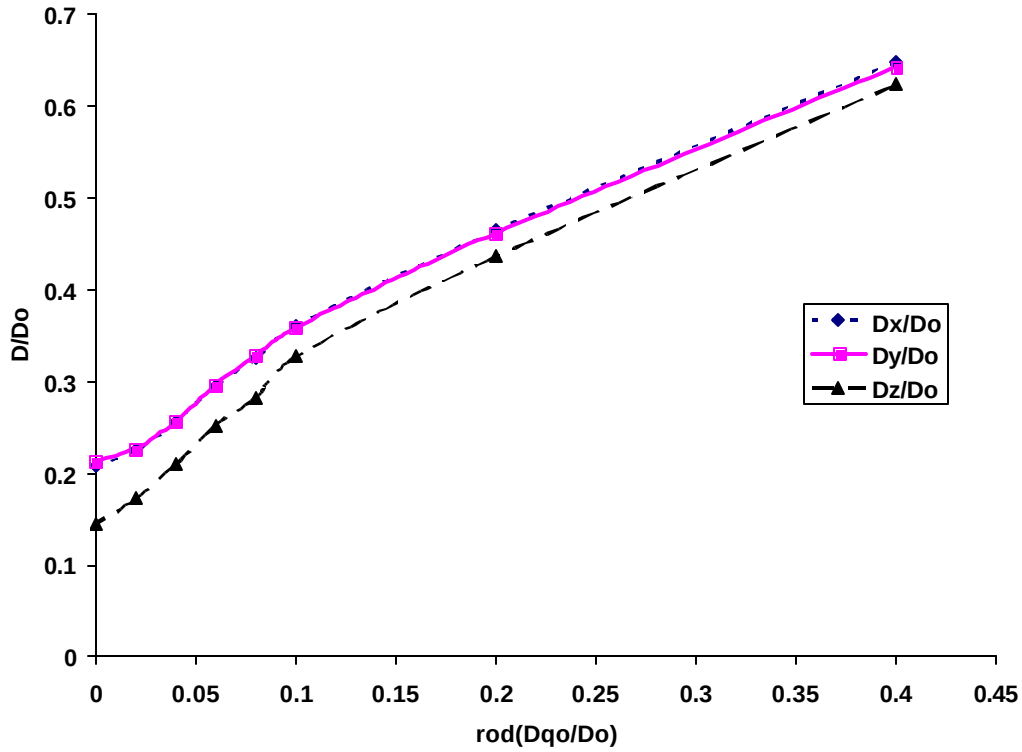

Figure 76 Dimensionless Effective diffusion coefficient vs. rod for 670

Following figure is an attempt to understand the comparison between samples at varying rod.

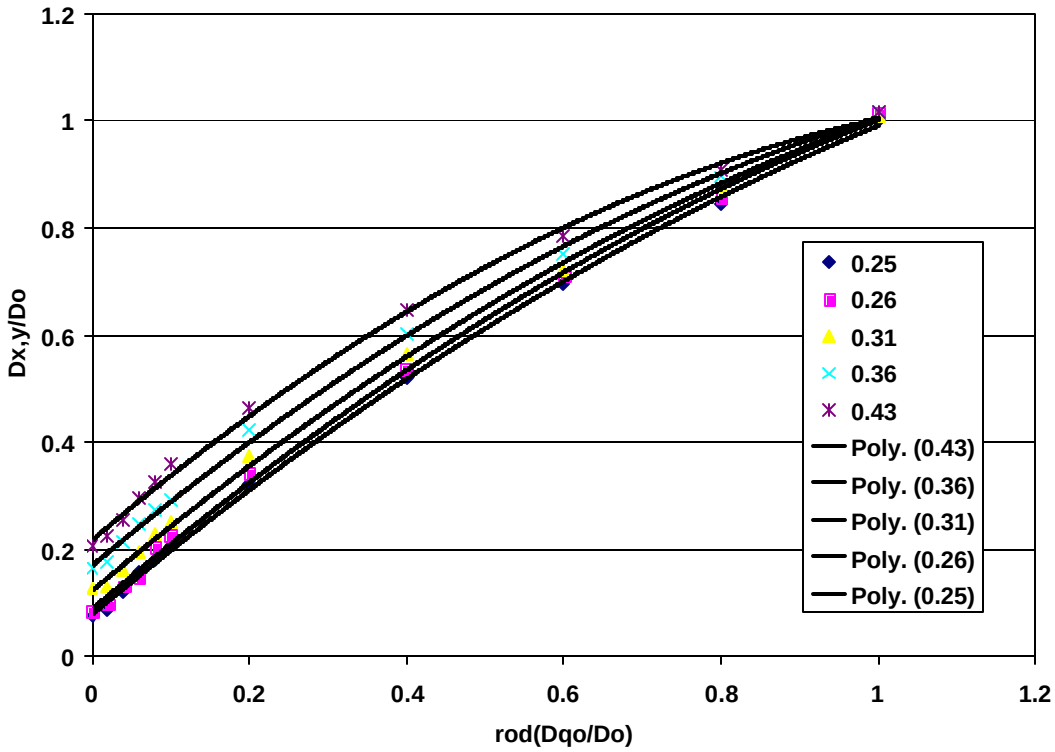

Figure 77 Dimensionless Inplane (XZ, YZ) diffusion coefficient vs. rod at different porosity

Above Figure 77 clearly indicates that as porosity of the sample increases the ratio (Dx/Do and Dy/Do) increases at particular rod. As the porosity increases structure becomes more open and less tortuous thereby giving passage to the water vapor molecules to diffuse more easily. It appears that there is not much difference among various samples for higher rods (>0.8). As discussed earlier, above these values of rod, structure behaves more or less like homogenous medium.

Similarly, transverse plane diffusivity values also decrease with decreasing porosity (Figure 78). This can also be explained similar to the in-plane diffusivity.

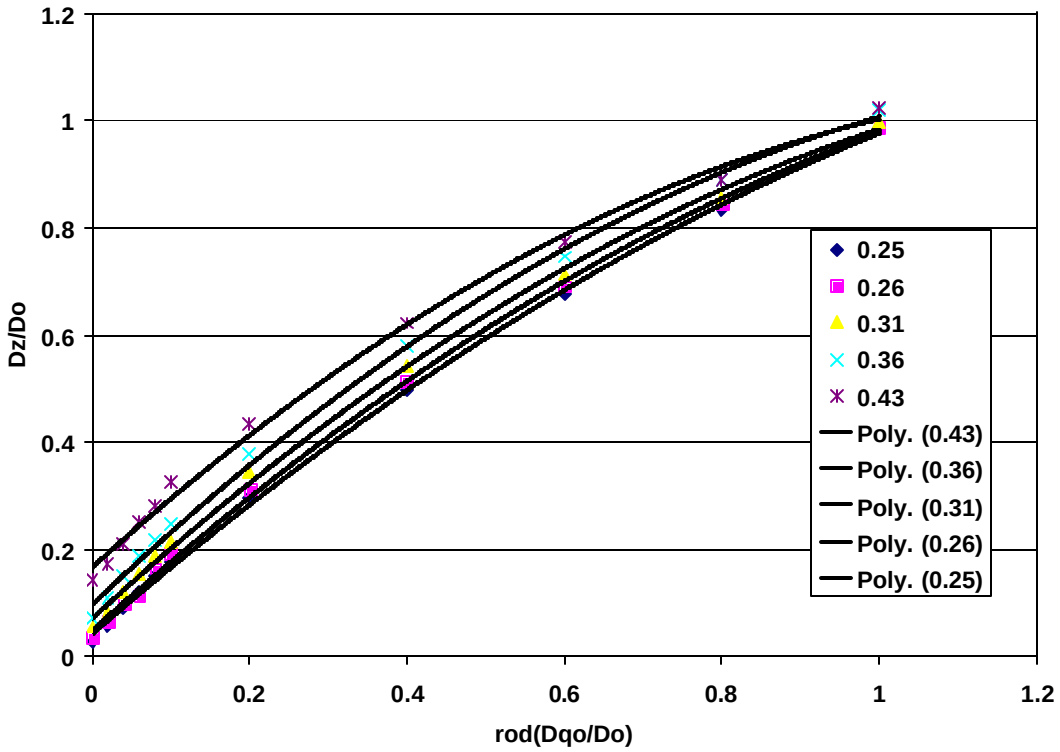

Figure 78 Dimensionless Transverse (XY) diffusion coefficient vs. rod at different porosity

In order to compare the effect of porosity of diffusivity ratio (D/Do), the following figure (Fig. 79) plotted at different rod values.

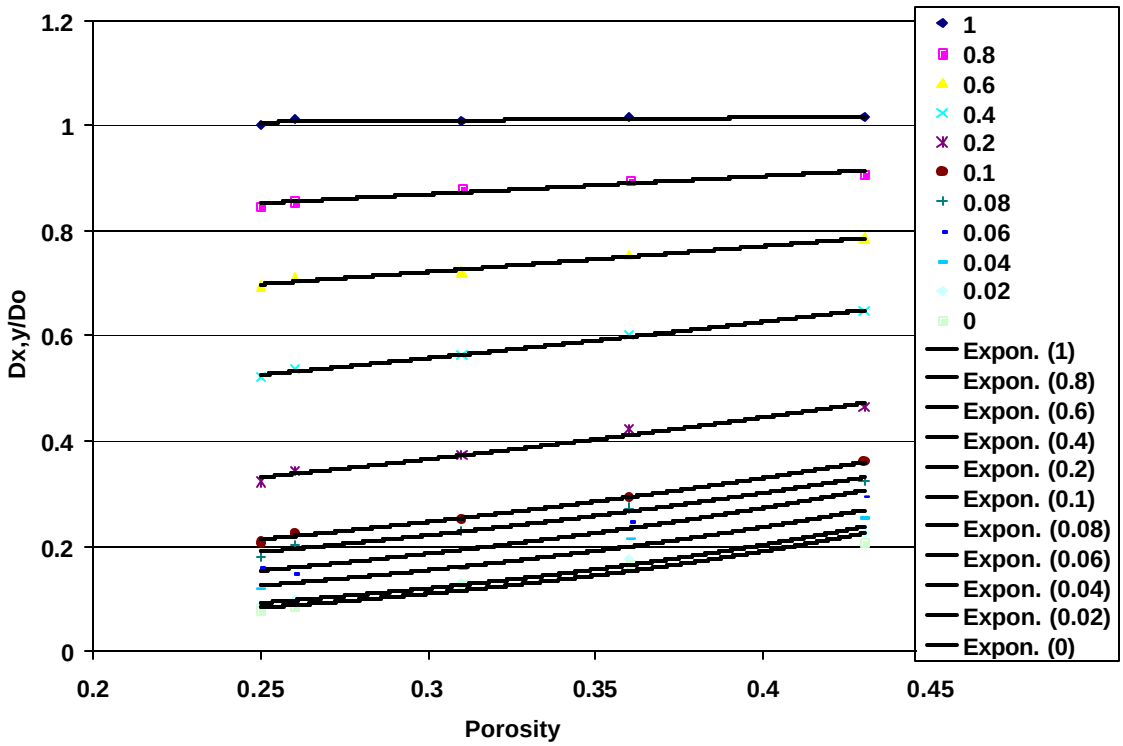

Figure 79 Dimensionless Inplane (YZ, XZ) diffusion coefficient vs. porosity at different rod

As porosity increases diffusivity increases at some particular rod. At particular porosity the Dx, y /Do increases as rod increases. The percentage decrease in inplane diffusivity values, from rod =0.4 to 0.2 is about 38 % for CSF 220 and goes down to 28 % for sample having highest porosity i.e. CSF 670. As mentioned earlier, the effect of structural characteristic on diffusion becomes more prominent at lower rods. Pore diffusion (rod =0) shows the biggest difference between structures. The percentage decrease in transverse diffusivity values (Fig. 80), from rod =0.4 to 0.2 is about 40 % for CSF 220 and goes down to 18 % for sample 670. The percentage decrease in inplane diffusivity values, from rod =0.04 to 0.02 is about 28 % for CSF 220 and goes down to 14 % for sample 670. The percentage decrease in transverse diffusivity values, from rod =0.04 to 0.02 is about 33 % for CSF 220 and goes down to 18 % for sample 670.

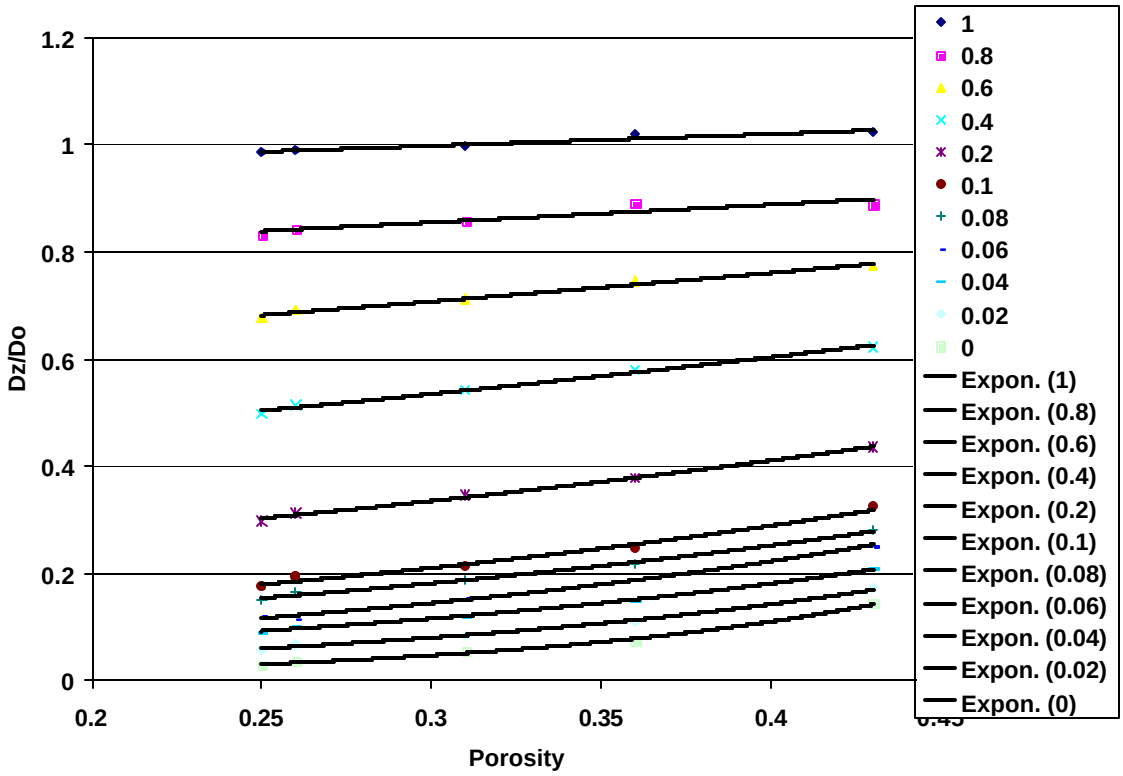

Figure 80 Dimensionless Transverse (XY) diffusion coefficient vs. porosity at different rod

Conclusions and Path Forward

A novel, non-destructive method to visualize and characterize the 3D structure of porous materials such as paper and board has been developed using X-ray micro computed tomography. A reconstruction of the void space by image analysis allowed us to obtain conventional measures such as porosity, interfacial area and pore size distribution. It appears that porosity shows a general decrease with refining level as would be expected. Pore size distribution analysis shows that for any given structure, the pore size distribution in the transverse view is broader than the in-plane views. The average pore size in transverse view is also larger than the in-plane views. Comparison of the sheet structure between a wet pressed and vacuum dewatered sheets show clear differences in the internal structure both in the in-plane and transverse views. As expected, the wet pressed sheets have a more closed structure with smaller pore sizes compared to the more open vacuum dewatered sheet with larger pores.

X-ray micro computed tomography and computer image analysis has been shown to be a suitable, non-invasive, direct method to visualize and characterize the complex 3D structure of porous materials including polymeric fabrics, paper, board etc. Structural characteristics have been shown to agree reasonably well with conventional techniques such as mercury intrusion porosimetry and optical microscopy with an error of approximately 3%. This technique can be used to benchmark structural characteristics of existing products as well as in new product development specifically designed for selected end-use applications. In addition to pore size distribution, the yarn size

distribution can also be used to estimate characteristic dimensions in all three principal directions. Using actual 3D structures obtained from X-ray micro computed tomography, direct simulations of fluid flow and vapor transport can be conducted using lattice-Boltzmann simulation and Brownian motion Random Walk simulations. These methods provide a novel way to estimate transport properties using actual geometric features of the porous media and also to simulate liquid and vapor transport during actual manufacturing process and end-use applications.

Results presented here clearly show the distinct differences in structure between commercially made fine paper and hand sheets. Commercial sheets do exhibit structural non-uniformity through the thickness direction. This offers a potential tool to characterize and solve problems related to two-sidedness etc. Commercial structures, even though more dense and less porous, are less tortuous and have higher fluid permeabilities at the same porosity. The differences between the in-plane and transverse structures are not so predominant in commercial sheets as compared to hand sheets. This could be due to the dynamic forming conditions on the commercial paper machine. The method shown here can be used to benchmark and truly engineer paper structures specifically designed for target end-use application.

We also present a image analysis method to characterize the surface structure of porous materials using X-ray micro computed tomography. This complements our earlier method to analyze the bulk structure and Z-D structure of porous materials. The measurements of surface structure characteristics include thickness distribution, surface volume distribution, contact fraction distribution and surface pit distribution. Method developed here even though shown for low resolution X-ray tomography images are equally applicable for high resolution (~1 micron) images. As one would expect, the surface structure characteristics will be critically dependent on the quality and resolution of the images. This presents a useful tool to characterize and engineer the surface structure of porous materials such as paper and board tailored to specific end-use applications. This will also help troubleshoot problems related to manufacturing and end-use applications.

Our future work will focus on evaluating the effect of process parameters and fiber raw materials on surface structure characteristics using high and low resolution images as well as predicting paper properties and end-use performance during industrial applications.

In this work we have presented a method using image analysis, random walk simulation, and stochastic dynamic approach to predict effective diffusivities in porous materials such as paper. Unlike previous methods, this method considers simultaneous diffusion in both the phases i.e. void (pore) and solid (fiber).

Techniques such as X-µCT enable us to capture the 3 D structural characteristics of porous materials such as paper. However, non-intrusive techniques to capture the nano structure of fibers *in-situ,* is years, if not decades, away. The method developed here overcomes the lack of nano-fibrous structure and provides a tool to estimate the effective transport properties of the medium as well as intrinsic characteristics of the fibers, which are hard to determine experimentally.

Pore space diffusivities predicted by the simulation method compares reasonably well with analytical expressions derived for periodic array of spheres. Pore space diffusivities of paper structures of varying porosities predicted by the simultaneous model with rod=0 compared favorably

well with experimental data. In-plane diffusivities are greater than transverse diffusivities in experimental as well as simulation results due to layered structure of paper. Diffusivities in both directions decrease with decreasing freeness values or decreasing porosity values.

Anisotropic diffusivities of paper structure (owing to the layered structure) by simulation showed characteristic differences between the two orthogonal planes, similar to experimentally observed behavior. As expected, transverse diffusivities are lower than in-plane diffusivities for all the paper structures studied. Effective diffusivity predictions by simulation are consistently higher than experimental values. One of the possible reasons can be that the resolution of 3D images may not be sufficiently high. The structures used in this work have 3-4 μm resolution. Also, if one has to use higher resolution (sub-micron) images then in addition to normal diffusion we may have to consider other diffusion processes such as Knudsen diffusion.

Effective diffusivities of the fiber phase predicted by the simulation agree reasonably well with experimental data at varying RH conditions. Similar to effective diffusivities of the whole structure, fiber phase effective diffusivities increase with increasing RH and porosity.

Intrinsic fiber phase diffusivity, a fundamental characteristic of the fiber structure is estimated for the first time using a combination of theoretical simulation and experimental data. In general, intrinsic diffusivities decrease with increasing refining potentially due to more consolidated fibers with more collapsed intrinsic fibrils. This suggestion is also supported by increasing intrinsic fiber diffusivity with increasing RH, potentially due to increasingly open, swollen fiber structures and possibly due to condensed phase contributing to overall diffusion. It is interesting, however, that overall change in effective diffusivities (about 2-5 times) from low to high RH can be explained by a small absolute change in rod (i.e. 0 to 0.06). There could be potentially couple of reasons for this behavior. One, this could be due to insufficient resolution of our 3 D structures. Second, fiber phase (with higher solid volume fractions, 0.8-0.6) is highly interconnected. A small change is sufficient to influence large changes in overall diffusivities of the structures. One way we could answer these questions is by conducting simulations for these samples using higher resolution images.

At present x-ray tomography can be used to visualize many porous media. So methods discussed in present work can be used to predict transport properties of various other porous materials for e.g. skin, fabric, rocks, biological cells and wood etc their relationship with structural characteristics.

There is wide variety of paper grades such as writing, printing paper, tissue, towel, packaging, newsprint, and specialty paper all of which have different types of wood fibers and chemical components. The operating conditions of paper machine also differ a lot depending on the final quality of paper. Hence, present model could be used to simulate diffusion for above mentioned papers. It will be interesting to compare the diffusions characteristics and their relationship to structure for various commercial papers.

In the present work, fibers have been treated as hollow cylindrical objects but in reality their internal structure is very complex with many micro-fibrils. So, the probability of “Knudsen diffusion” occurring inside fiber cannot be ignored. But as mentioned above with the present resolution it is not possible to visualize micro-fibrils. Hopefully in the future, if much higher resolution is available to

visualize the internal structure of fibers this may shed an additional light. It is also possible to include surface diffusion, which could play an important role under certain conditions, in our model.

Finally, the method developed as part of this project provides a viable tool for the papermaker to non-intrusively visualize the complex 3D internal structure of paper and board. The image analysis tools developed here also enable the papermaker to quantitatively characterize the internal structure so that it can be used to benchmark the products as well as to engineer the structure specifically designed for a given end-use applications. For the first time, paper makers have a sophisticated scientific tool at their disposal to truly optimize the fiber furnish, energy and cost efficiency of the manufacturing process to "engineer" the structure.

The method presented in this work also enable the papermaker to directly estimate the transport properties of their product and hence optimize their performance during manufacturing as well as during end-use. This will have significant direct impact on the fiber and energy efficiency of the whole papermaking process.

As the next step, we would like to extend this work to higher resolution X-ray micro computed tomography so that it can be made even more useful for the papermaker.

References

Ramarao, B.V. and Chatterjee, S.G., "Moisture Sorption by Paper Materials Under Varying Humidity Conditions", in *The Fundamentals of Papermaking Materials* (edited by C.F. Baker), PIRA International, UK, **2**: 703-749 (1997).

Bandyopadhyay, A., Radhakrishnan, H., Ramarao, B. V. and Chatterjee, S. G. "Moisture sorption response of paper subjected to ramp humidity changes: Modeling and Experiments" Ind. and Engng. Chem. Res., **39**, 1: 219-226 (2000).

Serra, J., *Image Analysis and Mathematical Morphology*, Vols. I and II. Academic Press, New York (1986)

Wang, J. Z., Dillard, D. A., Kamke, F. A. "Transient Moisture Effects in Materials." J. Mat. Sci., **26** : 5113-5126 (1991).

Habeger C. and D. Coffin. "Accelerated Creep Mechanics: Parts I and II." In *4th International Symposium on Moisture and Creep Effects on Paper, Board and Containers*, (edited by J.F. Bloch), EFPG, France, (1999).

Samuelsen, E.J., Gregersen, O.W., Houen, P.J., Helle, T." Three-dimensional imaging of paper by use of synchrotron X-ray microtomography", Proc. Tappi International Paper Physics Conference 307, (1999)

Samuelsen, E.J., Gregersen, O.W., Houen, P.J., Helle, T. "X-ray microtomography in paper", J. Pulp and Pap. Sci., 27 (2) (2001).

Gureyev, T., Evans, R., Stevenson, A.W., Gao, D., Wilkins, S.W. "X-ray phase contrast microscopy of paper" Tappi J. 84: 2 (2001).

Chow, C.K., Kaneko, T. "Boundary detection of radiographic images by a threshold method" *Information Processing* 71: 1529 (1972)

Kittler, J., Illingworth. J. "Minimum error thresholding", *Pattern Recognition* 19 (1): 41-47 (1986)

Analysis by Porous Materials Inc., Ithaca, NY, USA, 2000

Goel, A., Tzanankakis, M., Huang, S., Ramaswamy, S., Choi, D., Ramarao, B.V."Characterization of the three-dimensional structure of paper using X-ray microtomography", Tappi J. 84 (5): (2001).

Goel, A., Tzanakakis, E.S., Huang, S., Ramaswamy, S., Hu, W.S., Choi, D., Ramarao, B.V. "Confocal laser scanning microscopy to visualize and characterize the structure of paper" *AICHE Symposium Series*, No. 324, 96: 75-79 (2000).

SCHEIDEGGER, E. A., "The Physics of Flow Through Porous Media", The Macmillian Company, New York (1974).

Aaltosalmi, U., Kataja, M., Koponen, A., Timonen, A., Goel, A., Lee, G., and Ramaswamy, S. "Numerical Analysis of Fluid Flow through Fibrous Porous Materials", International Paper Physics Conference, Sept. 2003, Vancouver, B.C., Canada

Weitkamp, T. (2002): Imaging and tomography with high resolution using coherent hard synchrotron radiation, Doctoral thesis, Cuvillier Verlag, Göttingen, ISBN 3-89873-609-1.

Huang, S., Goel, A., Ramaswamy, S., Ramarao, B.V. and Choi, D. (2002): Transverse and in-plane pore structure characterisation of paper, Appita J. 55(3), 230-234.

Antoine, C., Nygård, P., Gregersen, Ø.W., Weitkamp, T. and Rau, C. (2002): 3D images of paper obtained by phase-contrast X-ray microtomography: image quality and binarisation, Nuclear instruments and Methods in Physics Research A 490, 392-402.

Aronsson, M. (2002): On 3D fibre measurements of digitized paper, Doctoral thesis, Swedish University of agricultural science, ISBN 91-576-6338-6.

Ramaswamy, S., Huang, S., Goel, A., Cooper, A., Choi, D., Bandyopadhyay, A. and Ramarao, B. V. (2001): The 3D structure of paper and its relationship to moisture transport in liquid and vapor forms, The science of papermaking, 12th Fundamental research symposium, Oxford, UK, vol. 2&3, 1289-1311 & 1641-1650.
Marr, D., and E.C. Hildreth. "Theory of edge detection", Proc. Roy. Soc. London., B-207:187—217 (1990).
Canny, J. "A computational approach to edge detection", in M. A. Fischler and O. Firschein, editors, Readings in Computer Vision: Issues, Problems, Principles and Paradigms. Morgan and Kaufmann, 1987.
J. Anthony Bristow and Petter Kolseth, "Paper Structure and Properties", Marcel Dekker, Inc., New York, 1986.
J. Anthony Bristow and Petter Kolseth, "Paper Structure and Properties", Marcel Dekker, Inc., New York, 1986.
Cussler, E.L., S.E. Hughes, W.J. Ward, R. Aris, "Barrier Membranes" J. Membrane Science, 38, 161 (1988)
Eitzman, D.M., R.R. Melkote, E.L. Cussler, "Barrier membranes with tipped impermeable flakes" AICHE Journal volume 42 (1): 2-9 (1996)
Hellen, E.K.O., Ketoja, J.A., Niskanen, K.J., Alava, M.J. "Diffusion through fiber networks" J Pulp Pap Sci. 28, no. 2: 55-62 (2002)
ARIS, R., "On a problem in hindered diffusion", *Arch. Ration. Mech. Anal*., 95(2): 83-91(1986)
GOEL, A., "Numerical Methods and Image Analysis to Predict the Transport Properties of Porous Media", *Ph.D. Thesis*, University of Minnesota, July, 2003.
EINSTEIN, A., "Investigations on the Theory of the Brownian Movement", Dover, New York (1926).
CUSSLER, E.L., "Diffusion: Mass Transfer in Fluid Systems", Cambridge (1997).
ZHENG, L.H., and CHIEW, Y.C., "Computer simulation of diffusion-controlled reactions in dispersions of spherical sinks", *J. Chem. Phys*. 90(1): 322-326 (1989).
http://astronomy.swin.edu.au/~pbourke/geometry/spherepoints
SIEGEL, R.A., and LANGER, R., "A New Monte Carlo Approach to Diffusion in Constricted Porous Geometries", *Journal of Colloid and Interface Science* 109(2): 426-440(1986).
EITZMAN, D. M., "Diffusion in Flake-Filled Barrier Membranes", *Ph.D. Thesis*, University of Minnesota, (1992).
MELKOTE, R. R., "Modeling of Transport and Reaction in Evolving, Fibrous Structures", *Ph.D. Thesis*, University of Minnesota, (1990)
LOEB, L.B., "The Kinetic Theory of Gases", McGraw Hills, New York (1934).
AKANNI, K.A., EVANS, J.W., and ABRAMSON I.S., "Effective Transport Coefficients in Heterogeneous Media", *Chemical Engineering Science* 42(8): 1945-1954 (1987).
Massoquete, A., Ramarao B. V., Lavrykov, S., and Ramaswamy, S., "The Effect of Refining on Anisotropic Moisture Diffusion in Paper", *ESPERA Research Report*, 118: 64-87 (2003[a]).
Massoquete, A., Ramarao, B. V., Lavrykov, S., Goel, A., and Ramaswamy, S., "Anisotropic Moisture Diffusion Study on Refined Paper", *2003 International Paper Physics Conference, Victoria, BC, Canada* 253-257 (2003[b]).
LESCANNE, Y., MOYNE, C., and PERRE, P., "Diffusion Mechanism in a Sheet of Paper", *Drying'92*:1017-1026 (1992).
LASO, M., "Stochastic Dynamic Approach to Transport Phenomena", *AIChE Journal* 40(8): 1297-1311 (1994).

NAKASHIMA, Y., and WATANABE, Y., "Estimate of transport properties of porous media by microfocus X-ray computed tomography and random walk simulation", *Water Resources Research*, 38(0), XXXX, doi: 10.1029/2001WR000937, 2002
REYES, S.C., and IGLESIA, E., "Effective Diffusivities in Catalyst Pellets: New Model Porous Structures and Transport Simulation Techniques, *Journal of Catalysis* 129: 457-472(1991).
ROSIUM, R.D., "Moisture effects on webs and rolls", *Tappi Journal* 76 (6): 129-136(1993).
NILSSON, L., WILHELMSSON, B., and STENSTRÖM, S., "The Diffusion of Water Vapor through Pulp and Paper", *Drying Technology* 11(6): 1205-1225 (1993).
LESCANNE, Y., MOYNE, C., and PERRE, P., "Diffusion Mechanism in a Sheet of Paper", *Drying'92*:1017-1026 (1992).
LIANG, B., FIELDS, R.J., and KING, C.J., "The Mechanisms of Transport of Water and N-Propanol through Pulp and Paper", *Drying Technology* 8(4): 641-665 (1990).
AHLEN, A.T., "Diffusion of Sorbed Water Vapor through Paper and Cellulose Film", *Tappi Journal* 53 (7): 1320-1326(1970).
FOSS, W.R., BRONKHORST, C.A., and BENNETT, K.A., "Simultaneous Heat and Mass Transport in Paper Sheets during Moisture Sorption from Humid Air", *AIChE Symposium Series No. 322*, 95: 80-88 (1999).
RISKEN, H., "The Fokker-Planck Equation", Springer Verlag (1989).
BIRD, R.B., CURTISS, C.F., ARMSTRONG, R.C., and HASSAGER, O., "Dynamics of Polymeric Liquids: II Kinetic Theory", Wiley, New York (1987).
KALLIANPUR, G., "Stochastic Filtering Theory", Springer Verlag (1980).
GARDINER, C.W., "Handbook of Stochastic Methods for Physics, Chemistry and the Natural Sciences", Springer Verlag (1983).
MARUYAMA, G., "Continuous Markov Processes and Stochastic Equations", *Rend. Circolo Math. Palermo* 4: 48(1986)
KLOEDEN, P.E., and PLATEN, E., "Numerical Solution of Stochastic Differential Equations", Springer Verlag (1992).
Holmstad, R.T. Ph.D. Thesis, Department of Chemical Engineering, NTNU, Trondeheim, Norway (2004)